

Phonons and excitons in colloidal CdSe/CdS quantum dots with wurtzite and zinblende crystal structure

vorgelegt von
Diplom-Physikerin
Amelie Laura Biermann
geb. in Berlin

von der Fakultät II - Mathematik und Naturwissenschaften
der Technischen Universität Berlin
zur Erlangung des akademischen Grades

Doktor der Naturwissenschaften
– Dr. rer. nat. –

genehmigte Version

Promotionsausschuss:

Vorsitzender: Prof. Dr. Lehmann
Gutachterin: Prof. Dr. Axel Hoffmann
Gutachter: Dr. Anna Rodina

Tag der wissenschaftlichen Aussprache: 01.12.2017

Berlin, 2018

1 Abstract

This thesis presents a thorough analysis of the optical and vibrational properties of colloidal II-VI-semiconductor quantum dots, focussing on the effects of crystal structure differences and the interplay within core-shell QDs on the lattice vibrations, temperature dependent lattice parameters the exciton-phonon coupling and the exciton fine structure. Here, spherical CdSe/CdS QDs of different sizes are studied. The nano-scale confinement not only allows the growth in the wurtzite structure – the default for bulk CdSe – but also in the zinblende structure. Since these two structures are fundamentally different, it is one of the main objectives of this work to analyze the influence of the crystal structure on the properties of the QD.

The lattice parameters of core-shell QDs are investigated and strain and temperature dependent effects are separated by comparison with reference samples at the same temperature. This leads to the extraction of purely temperature dependent lattice expansion coefficients thus becomes possible for each material, revealing different expansion behaviors for the wurtzite and zinblende structured cores, as well as a dependence on the core size. The exciton-phonon coupling within the QD is studied with Raman spectroscopy, in dependence of the QD diameter and the effect of zinblende and wurtzite crystal structure, revealing a size dependent minimum in coupling strength. Additionally, the influence of the addition of a CdS shell on the coupling is investigated with Raman spectroscopy and resonance PL, finding decreasing coupling for increasing shell thickness.

The difference in crystal structure, i.e. the anisotropy of the wurtzite structure with it's piezo- and pyroelectric fields, should strongly influence the charge carriers and their band structure. Using photoluminescence excitation spectroscopy, the band edge fine structure is revealed to be different for zinblende and wurtzite CdSe QDs, as well as diameter dependent. This is mainly achieved by evaluating the energetic distance between the lowest bright and dark exciton states, which becomes larger both for smaller QDs and in wurtzite structures. For comparison, the excitonic states are calculated according to a established formalism. The results reveal that the existence of this dark state in zinblende structures can only be explained by a oblate deformation of about 10%, which induces an anisotropy large enough to cause the observed splitting.

In the final section of this thesis, a more complex hybrid structure is studied, namely a CdSe/CdS core-shell system which is enclosed in a thick shell of protective silica against a reactive environment, that is present in biological applications. Through a combined approach of TEM and Raman analysis, this study reveals that a successful silica encapsulation employing loosely bound ligands leads to the formation of an interface between QD and silica. This interface between the CdS shell and the silica shell, is proposed to be formed via the formation of Cd-O-Si bonds at the QD surface.

2 Zusammenfassung

Diese Arbeit befasst sich mit optischen und vibronischen Eigenschaften kolloidaler Quantenpunkten aus II-VI-Halbleitern. Dabei werden die Auswirkungen unterschiedlicher Kristallstrukturen und der Wechselwirkung innerhalb von Kern-Hülle-Systemen auf die Gitterschwingungen, die Exziton-Phonon-Kopplung und die Exzitonische Feinstruktur der Quantenpunkte (QD). Hierfür werden sphärische CdSe/CdS Quantenpunkte verschiedener Größen und Kristallstrukturen mit Hilfe von Ramanspektroskopie und Photolumineszenz-Anregungsspektroskopie (PLE) untersucht. Durch ihre geringe Größe ist es möglich diese Strukturen nicht nur in der für Bulkmaterialien üblichen Wurtzitstruktur, sondern auch in Zinkblendestruktur herzustellen. Da sich die beiden Strukturen fundamental in ihrer Polarität unterscheiden, ist es von besonderem Interesse heraus zu finden, welche Auswirkungen dies auf die Eigenschaften der QD hat.

Aus der Temperaturabhängigkeit der Phononenmoden in Kern-Hülle-Systemen werden die rein temperaturabhängigen linearen thermischen Ausdehnungskoeffizienten bestimmt. Dafür werden Verspannungseffekte, die durch das Zusammenspiel von Kern und Hülle entstehen, von der eigentlichen Temperaturabhängigkeit separiert. Dies führt zu Ausdehnungskoeffizienten, die sich für CdSe und CdS unterscheiden, aber auch von der Kristallstruktur und vom QD-Durchmesser abhängen.

Desweiteren wird die Exziton-Phonon-Kopplungsstärke in Abhängigkeit des QD-Durchmessers für QDs mit Wurtzitstruktur und Zinkblendestruktur mit Hilfe von Ramanspektroskopie untersucht. Dabei wird für beide Kristallstrukturen festgestellt, dass es ein Minimum in Kopplungsstärke bei einem bestimmten Durchmesser gibt. Der Einfluss einer CdS Hülle um den CdSe Kern reduziert die Kopplung, wie mit Ramanspektroskopie und resonanter Photolumineszenz beobachtet wird. Außerdem wird eine höhere Kopplung bei QDs mit Wurtzitstruktur beobachtet, was mit höheren internen Feldern zu erklären ist.

Der Einfluss der unterschiedlichen Kristallstruktur wird ein weiteres Mal klar, wenn die elektronischen Bandkanten Zustände betrachtet mit Hilfe von PLE werden. Bei der Analyse von Zinkblende und Wurtzit QD mit verschiedenem Durchmesser wird beobachtet, dass die Aufspaltung zwischen den Bandkanten Zuständen größer wird je kleiner der Durchmesser des QDs. Außerdem wird beobachtet, dass die Separation zwischen den beiden untersten elektronischen Übergängen generell für Wurtzitstruktur höher ist.

Die elektronischen Bandkanten Zustände werden mit Hilfe eines etablierten Formalismus ermittelt, dafür muss um eine entsprechende Aufspaltung zu erlangen für Zinkblende eine Deformation in Richtung abgeflacht angenommen werden, da ansonsten auf Grund der Isotropie des Kristalls keine Aufspaltung entsteht.

Zum Schluss wird das Hybridsystem bestehend aus einem von einer Sili-

kathülle umgebenen CdSe/CdS QD analysiert, dass wegen seiner hohen chemischen Stabilität nachgefragt ist. Die Silikatumhüllungssynthese wird *in situ* mit Ramanspektroskopie beobachtet. Hier wird gezeigt, dass das amorphe Silikat direkt mit dem QD wechselwirkt, ohne eine Ligandenzwischenschicht wechselwirkt. Als mögliche Bindung zwischen den Materialien wird eine Cd-O-Si Brücke vorgeschlagen.

3 List of publications

Some of the results included in this thesis have been published:

Ghazarian, N., Biermann, A., Aubert, T., Hens, Z., and Maultzsch, J. “*Thermal Expansion of Colloidal CdSe/CdS Core/Shell Quantum Dots*”, in preparation (2017)

Biermann, A., Aubert, T., Baumeister, P., Drijvers, E., Hens, Z., and Maultzsch, J. “*Interface formation during silica encapsulation of colloidal CdSe/CdS quantum dots observed by in situ- Raman spectroscopy.*” J. Chem. Phys., 146(13):134708-7, April 2017.

Cirillo, M., Aubert, T., Gomes, R., Van Deun, R., Emplit, P., Biermann, A., et al. (2014). “*Flash*” *Synthesis of CdSe/CdS Core-Shell Quantum Dots. Chemistry of Materials*, 26(2), 1154-1160.

<http://doi.org/10.1021/cm403518a>

Norman Tschirner, Holger Lange, Andrei Schliwa, Amelie Biermann, Christian Thomsen, Karel Lambert, Raquel Gomes, and Zeger Hens. “*Interfacial Alloying in CdSe/CdS Heteronanocrystals: A Raman Spectroscopy Analysis.*” Chem. Mater., 24(2):311-318, January 2012.

C. Friedrich, A. Biermann, V. Hoffmann, M. Kneissl, N. Esser and P. Vogt, “*Preparation and atomic structure of reconstructed (0001) InGaN surfaces*”, J. Appl. Phys. 112, 033509 (2012); <http://dx.doi.org/10.1063/1.4743000>

Contents

1	Abstract	i
2	Zusammenfassung	ii
3	List of publications	v
4	Colloidal Nanocrystals, an introduction	1
4.1	Applications and resulting demands on the QD's properties	4
4.2	Properties of core-shell QDs	6
5	Theoretical background: Raman spectroscopy	11
5.1	Raman effect in bulk crystals, Raman spectroscopy setup and interpretation	11
5.2	Strain determination from Raman spectroscopy	13
5.3	Exciton-phonon coupling strength determined from Raman spectroscopy	14
6	Experimental methods	16
6.1	Raman spectroscopy setup	16
6.2	Photoluminescence excitation spectroscopy (PLE) setup	18
7	Synthesis of CdS/CdSe colloidal QDs and subsequent Silica encapsulation	21
7.1	Synthesis of colloidal QDs	21
7.1.1	Exemplary CdSe QD syntheses	24
7.2	Semiconductor shell addition methods for bare colloidal QDs and properties of the core-shell QDs	25
7.2.1	Exemplary SILAR and <i>flash</i> synthesis and comparison of resulting properties	25
7.3	Silica encapsulation for biological applications	28
8	Structural and electronic properties of CdSe/CdS quantum dots	31
8.1	Crystal lattice and optical properties of CdSe/CdS QDs	31
8.2	Raman spectra of pure CdSe QDs and CdSe/CdS core-shell structures	34
9	Temperature dependent lattice contraction in wurtzite and zinblende core-shell QDs	42
9.1	Temperature dependence of Raman modes in wurtzite and zinblende core-shell NC	42
9.2	Separation method of thermal and epitaxial strain effects	47
9.3	Linear temperature coefficients for heterostructures	49

10 Exciton-phonon coupling	55
10.1 QD diameter dependent Huang-Rhys factor from Raman spectroscopy	57
10.2 Huang-Rhys factor in CdSe/CdS core-shell QDs	61
11 Excitonic fine structure of CdSe QD	64
11.1 CdSe QDs in PLE measurements	66
11.2 Determination of the energy to size conversion at low temperatures	69
11.3 Temperature dependence of the near band-edge states	71
11.4 Fine structure dependence on QD size, emission energy and crystal phases	74
11.5 Excitonic fine structure in CdSe/CdS core-shell QDs	80
12 Effect of a silica shell on the encapsulated QD	85
12.1 Previous studies by TEM, PL and absorption	85
12.2 Synthesis of silica particles and the synthesis reaction mechanism in the reverse micelle microemulsion	88
12.3 The <i>in situ</i> Raman setup and synthesis of silica shell on CdSe/CdS QDs	91
12.4 Raman analysis of the silica encapsulation of CdSe/CdS QDs	94
12.5 Dynamics of the silica encapsulation reaction analyzed by <i>in situ</i> Raman and TEM	97
12.6 Origin of the change in Raman frequency during silica synthesis	101
12.7 The evolution of the Raman intensity observed during silica encapsulation	105
12.8 QD A and QD B's diverging evolution of the Raman spectrum during silica encapsulation	109
13 Conclusions	113
14 Bibliography	116
15 Acknowledgments	130

4 Colloidal Nanocrystals, an introduction

Colloidal nanocrystals (NC), or colloidal quantum dots (QDs), are crystals in the nanometer size range that are in a stable solution with an organic or inorganic solvent. The solution is stabilized by ligands (surfactants) which are molecules with a polar and a non-polar part. Often the non-polar part consists of one or several long carbon chain, which is attached to a polar functional group at one end. They organize around the polar surface of the colloidal NC, orienting their polar part towards the NC surface and to non-polar part towards the solvent (Fig. 1). This construct is called a micelle and enables to keep the NCs in stable solution with a non-polar solvent (e.g. toluene, hexane).

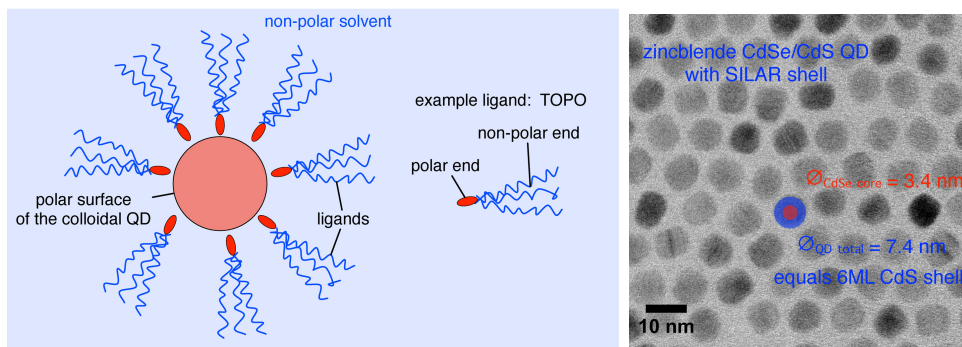


Figure 1: Right: Colloidal QD inside a micelle of ligands in solution of a non-polar solvent, such as toluene. Non-polar objects and areas are shown in blue, whereas polar ones are red. The example ligand shown, is TOPO (trioctylphosphinoxid, three carbon chains (non-polar) depicted as blue lines, with the red phosphinoxid end (polar)). The ligand molecules arrange around the QD with the polar end oriented in direction of the polar crystal surface, while the non-polar carbon chains ensure the suspension of the QD in the non-polar solvent. Left: TEM image of spherical zincblende CdSe/CdS QDs (CdSe diameter 3.4 nm, total diameter 7.4 nm) as an example for the QDs examined in this work.

In this way, using the correct ligand for each combination of specific NC and solvent, the NCs are prevented from settling at the bottom of the containment and/or agglomerating at the same time. The ligand needs to be chosen specifically to fulfill the demands of the intended application. Electronic conductive ligands for instance, are mandatory and performance limiting for applications like electrically driven LEDs or solar cells. In those applications, the colloidal NCs are used as the active element. Charge carriers need to be injected in the NC in the case of LEDs and the separated and

subsequently extracted in the case of the solar cells. For those applications, colloidal NCs would be an interesting and promising candidate, since due to their small size, they exhibit quantum confinement effects (hence the name quantum dot), which enables to tune the emission wavelength with the NC size. Many colloidal QDs are shown to offer a very high quantum yield and high absorbance. Additionally, the possibility to apply an active layer for a device from solution would open up completely new fabrication methods. Hence, finding the optimal ligand for such applications is a subject of great interest in research. [1–4]

The NC itself contains a few hundred until a few thousands of atoms, arranged in approximately regular patterns that are often similar to structures known from bulk semiconductors. Other than those well-known bulk materials or epitaxial quantum dot-structures, grown in metal-organic vapor phase epitaxy (MOVPE) or molecular beam epitaxy (MBE), colloidal NCs are synthesized in a wet-chemical reaction in solution. Different syntheses of CdSe/CdS QDs used in this work, will be addressed in detail in Section 7.1.

While the NCs have a regular crystal structure on the inside, the crystal symmetry is broken at the surface due to the lack of bonding partners. Open bonds are energetically unfavorable and hence surface reconstructions are formed or bonds to molecules in the NC's proximity to reduce the surface energy. This means the surface has inherently different properties than the corresponding bulk material; how big the influence of this surface is on the QD and how exactly the surface is influenced by the surrounding medium is widely unknown, despite being researched for many years.

The outer form of the NC can be varied by the choice of precursor, ligand and reaction condition, which can selectively favor the growth at different reactive crystal surfaces. This gives rise to a wide variety of forms ranging from spheres to triangular/rectangular pyramids and cubes to elongated sticks, rods or wires. Nevertheless, many authors found indications that the influence of the surface on the QDs properties are considerable



Figure 2: Colloidal zincblende CdSe QDs of different sizes (between 2.5 and 5.5 nm), emitting light at their corresponding lowest electronic transition because of UV illumination. This highlights the broad spectrum of wavelengths that can be reached depending on the QD size. From Sofie Abé, private communication

Due to their finely tunable size, colloidal QDs can be synthesized to a wide range of wavelengths because of electronic confinement in two or three dimension, depending on the shape of the QD. Because of their different bulk emission wavelength, different materials are used to produce colloidal QDs in different wavelengths. Among the widely used II-VI semiconductors alone, the range in wavelength varies from PbSe, which is used for the infrared and red region to CdSe for visible wavelengths, and to CdS for blue and UV. In Fig. 2 solutions of differently sized zincblende CdSe QDs are shown. Under UV illumination, the QDs shown in the figure emit at the energy of their lowest electronic transition. Thus, the figure shows the diversity of emission wavelength available by size variation alone.

CdSe QDs (like CdS, ZnS etc.) can be synthesized in two basic crystal symmetries; zincblende and wurtzite structure. The two symmetries have very similar bond lengths, hence the formation of both symmetries is possible in the same inter-atomic potential. In colloidal QDs, zincblende structure forms comparatively easy in syntheses using lower temperatures and different precursors and surfactants than wurtzite, however, it is not found as a bulk material. The diverging properties caused by the different symmetry are often neglected as similar emission wavelength with similar characteristics can be produced for the two configurations. However, the wurtzite structure is a polar structure, and such has pyro- and piezo-electric fields. This leads to a polar moment along the c-axis, which on the one hand enhances light absorption (or generally interaction with light) in this direction, and on the other hand also influences surface states, causes surface charge accumulation at interfaces and band bowing. Additionally, effects like for example the Quantum Confined Stark Effect should be present in wurtzite material.

In summary, while colloidal QDs are a promising and interesting material for different applications (see also following Sections), it is especially out of interest to analyze the surface of the QDs in general, influences of changing surface chemistry and the influence of the crystal anisotropy.

In this Section, general properties of colloidal QDs in application prospects (Sec. 4.1), as well as core-shell QDs, which are heterostructures combining different materials will be addressed. Heterostructures combining different crystalline semiconductor materials, will be covered in Sec. 4.2, focussing on CdSe/CdS QDs as they are the subject of this work. Beyond those crystalline structures, it is also possible to enclose the QDs in different, non-crystalline materials to modify the QDs surface (Sec. 7.3). This becomes especially necessary for application of the QDs as biological labels, to provide a chemical barrier towards the reactive environment in the application.

4.1 Applications and resulting demands on the QD's properties

Colloidal QDs are a promising candidate for many applications, especially in opto-electronics, due to their great luminescent brightness, high absorption and finely tunable emission wavelength, with bandgaps in the visible and infrared spectral region. The first working diode based on colloidal CdSe QDs has been demonstrated already in 1994 by Colvin et al.[5], followed by further well-known proof of principle publications on the electro luminescence of CdSe QDs in 1996 and 1998[6, 7] And the first working diode based on colloidal CdSe QDs has been demonstrated already in 1994 by Colvin et al.[5]

In general, there are different basic sorts of optoelectronic applications, one is based on the as efficient as possible emission of light, like LEDs or lasers, and one that relies on absorption and subsequent charge separation, solar cells for instance. For the first, a high emission, high QY and finely controlled emission wavelength is of high importance. Here, an additional challenge is posed by the complexity of electronically contacting the QDs, which is necessary to drive the devices electrically. This originates from the surface stabilization with ligands, as the conventionally used ones are electrically isolating, like TOPO (trioctylphosphinoxid), TOP (trioctylphosphine) or oleic acid (see Fig.8) for instance. Hence, the search for conductive ligands provides a great field of research in order to reduce losses at the surface and optimize the device efficiency. Nevertheless, working colloidal QD LEDs have been demonstrated by several groups already. [8–10] Even white LEDs have been demonstrated, combining different colloidal QDs.[11] Here, the “green gap” can be covered more easily than with conventional semiconductor materials like InGaN.

Whereas Dang et al show optically pumped red, green and blue lasing colloidal quantum dot films[12], using QDs showing single-exciton gain and an efficiency exceeding 80%, which show constant efficiency over 2000h and are hence interesting as backlight of displays.

But also efficient solar cells are demonstrated frequently. A good overview is given by Talapin et al..[1] Here, a great advantage compared to conventional materials is the simpler realization of multi-junction architectures that can potentially boost the power conversion efficiency greatly, by providing efficient absorption over the whole solar spectrum and low energetic loss. Lunt et al. analyze different architectures and combination possibilities in detail and find that single junction solar cells should be able to reach power conversion efficiencies up to 17% and tandem cells (combination of two different QD films) even could achieve 24%. Those structures can potentially have lifetimes of about 10-15 years, and thus should be of great interest for generation of solar energy.[13] Already during the past years efficiencies have increased rapidly and are now exceeding 10%. Lan et al. for instance reached 10.6

% with PbS QDs by engineering the polarity of the halide QD passivation with the solvent.[14] In the infrared region, efficient and stable photovoltaics with an external QY of 46% have been demonstrated by Koleilat et al. by employing linker molecules within the QD film to enhance the electric conductivity.[15]

However many of the realized concepts are based on the so-called Grätzel-cell [16], originally conceptualized to use dye-molecules in a solar cell and published in 2000. Although different architectures and even devices produced in an all-solution process are thinkable. For the Grätzel-cell, the dye-molecules (now colloidal QDs) are adsorbed on a mesoporous TiO₂ (titanium dioxide). The TiO₂ functions as an electrode, offering a large surface area for coverage with QDs, which can absorb the generated electrons at high speed and efficiency. The transport of holes is realized by an electrolyte surrounding the QD-covered TiO₂.

During the past years, colloidal QDs have raised interest in a different area of application entirely: biology. In biology, there is great demand for making biological processes visible by monitoring the position of specific cells or molecules in cells or in the body. This applies to a broad spectrum of application from monitoring cancer cells and stretches to understand different aspects of the metabolism. Conventionally organic fluorophores are used as emitters. The emitters are attached to a marker molecule with a large affinity to dock to the specific cell-type to be monitored, so the position is visualized by emission of the fluorophore close to the marked cell under illumination. However these fluorophores, as they are molecules, fluorophores defined and discrete electronic states. This means in order to excite them efficiently, the light source has to match one of the higher excited electronic states. This makes it hard to use different markers to see different types of cells at the same time and excite at once. Here, colloidal QD offer the advantage of a overall higher absorption, and broader absorption spectrum. At the same time, they exhibit intense and long-term stable luminescence, providing the opportunity of long-term observation and fast/easier detection because of the higher intensity.[17, 18] Further information can be found in several reviews like for instance Pietryga *et al.* or Jing *et al.*[2, 3]

However, in order to use the QDs in biological applications, they must be adapted to be stable in aqueous environments. Therefore, the encapsulation of the QDs in different materials has been researched for years, creating a chemical barrier between the QD and the environment while offering solubility. The shell material in question need to be optically transparent for the markers to be visible. Additionally, these materials should optimally be biocompatible and offer possibilities for functionalization, as it must be possible to couple the encapsulated QD to molecules that target specific cell. For this, different polymers and silica have been suggested for use. The use of a silica shell has been investigated during the past years [18, 20–22] and research has shown that it offers higher stability in water and other polar

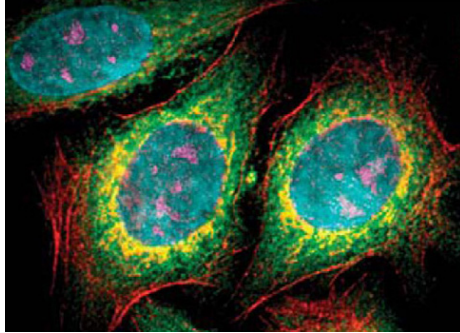


Figure 3: Example of a QD decorated human (epithelial) cell, using five different colors: Cyan corresponds to 655-QDs labeling the nucleus, magenta 605-QDs labeling Ki-67 protein, orange 525-QDs labels mitochondria, green 565-QDs labels microtubules, and red 705-QDs labels actin filaments. Taken from [19].

solvents and different harsh conditions, like pH.[23]

In this work we investigate silica capped QDs and analyze the encapsulation synthesis in detail. In Section 12, we address the effects of silica encapsulation on the QD. While the state of the art of silica encapsulation is presented in Sec. 7.3, the procedure of in situ Raman measurements during the synthesis is described in Sec. 12.3 and the results are presented in Sec.12.

4.2 Properties of core-shell QDs

Due to differently strong confinement, colloidal QDs can be synthesized with almost any desired emission wavelength, however when a single material is applied, e.g. CdSe or HgTe, the surface of the QD is in direct contact with the surrounding environment, which has been shown to reduce chemical and luminescent stability. On the one hand, this direct contact to the environment can result in surface defects. This is because the open, unsaturated bonds on the QD surface are likely to bind to molecule in their vicinity or form reconstructions, which can trap charge carriers and thus reduce the quantum yield by non radiative recombination. Or on the other hand the uncovered surface provide defect centers that emit at another wavelength entirely. Overall these surface trap states lead to a strongly reduced photoluminescence quantum yield (PLQY) and enhance photo bleaching, as well as reducing the chemical stability against the environment and thus complicate post synthesis processing steps such as atomic layer deposition, which are mandatory for some device concepts.

Additionally, the surface is prone to interaction with the environment and chemical reactions are probable, which could hinder the application of those QDs in certain environments. For instance, it has been shown that an acidic environment or an oxidative environment (like water for instance) reduces the QD lifetime drastically. [24–26]

One way to saturate the open surface bonds of the optically active part of the QD is to cover the QD in a material with the same crystal structure and similar lattice constant. In case the chosen shell material has a larger band

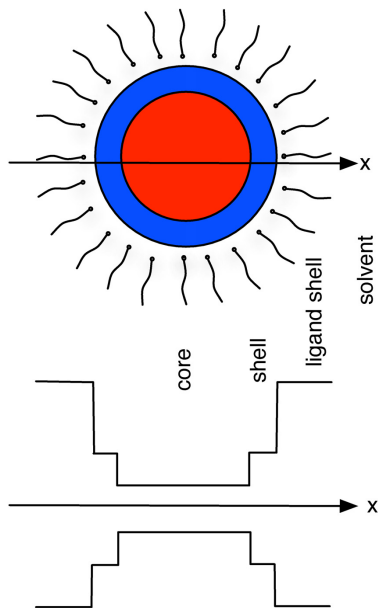


Figure 4: Schematical image of a colloidal core shell QD surrounded by its ligand shell and solvent, below schematic cross section along the QD symmetry axis of the ground and lowest excited state of core and shell for QD with type-I band alignment, including the surrounding ligand shell (“high energy gap”/isolator) and solvent/air ($\approx \infty$) for visualization of confining potentials at play in a core shell structure. Band offset and absolute energy differences not to scale.

gap than the enclosed QD (now called core), depending on the band-off set, the structures can have type I or type II band alignment. For type I band alignment (Fig.4) the potential minimum for electrons and holes is in the core of the QD, hence both charge carriers locate in close spacial proximity. This leads an efficient recombination of free charge carriers, as opposed by type II alignment, where the electrons accumulate in the core and holes in the shell of the QD or vice versa. Thus the free charge carriers are spatially separated in type II QDs. Hence for the recombination an additional momentum is needed, which makes the recombination less probable and in consequence reduces the QY. This renders type II alignment unfavorable for applications that demand high emission intensity and efficiency. The CdSe/CdS core-shell structures, that are discussed in the work, show a type I alignment. This also means, that the core, the part of the QD where the free charges accumulate plays the dominating role in the emission.

The coverage of the crucial part of the QD propels the reactive QD surface further away from the optically active material and thus reduces trapping of charge carriers at the surface and improves the PLQY widely.[27–29] Since this encapsulation of the QD core changes the environment from a mixture of ligands and solvent (mostly non-polar solvents, such as toluene) or ligands and air, an essentially isolating environment, to a semiconducting environment, this effectively relieves the electronic confinement in the core by reducing the step height in the surrounding potential form near infinity to a finite height (see schematics Fig.4). As a consequence, the electronic transition energies are shifted towards lower energies after capping. This has to be taken into account when configuring a QD for a specific applica-

tion with a determined emission wavelength; however since there has been extensive research connecting emission wavelength, and core and shell size and the correlation with growth conditions and times, this is not an obstacle.[27–29]

Apart from the electronic properties, the shell also influences the atomic lattice of the core. For an epitaxial growth, the two lattice constants need to be similar, with as small a mismatch as possible. At the interface of the two materials, each material needs to deviate from their respective “ideal”, bulk-like lattice constants to accommodate direct bonds. This distortion of the lattice is called strain (Fig. 5). The lattice that has a reduced bond length as compared to the bulk bond length shows compressive strain, whereas the lattice that stretches the bonds in comparison to bulk shows tensile strain. Strained materials not only exhibit changed phononic properties, but can also have altered optical properties compared to their unstrained state, in particular in polar structures.

Looking at the bulk lattice constants of zincblende CdSe $a=6.13$ nm [30]

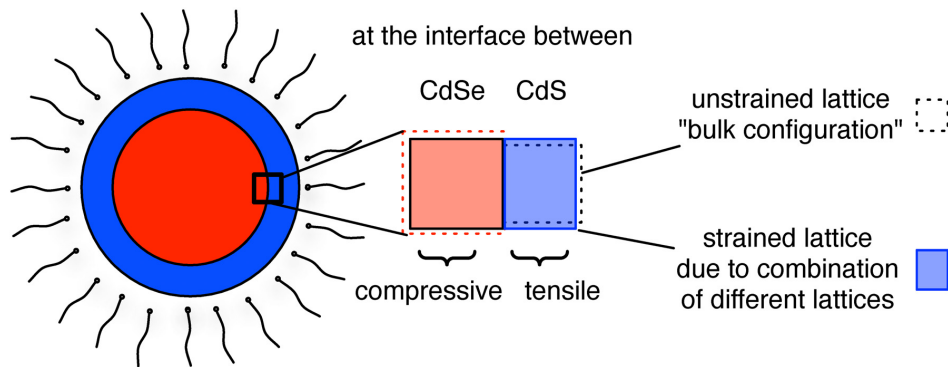


Figure 5: Core shell QD with exemplary lattice constants for CdSe as core and CdS as shell material. The zoom to the interface of core and shell material shows the deviation of bond length from the “ideal” that each material has to undergo to form direct bonds. While the CdSe core needs to reduce the mean bond length, the CdS shell stretches the mean bond length, therewith the core shows compressive and the shell tensile strain.

and CdS $a=5.83$ nm[31], and wurtzite CdSe $a=4.37$ nm and $c=6.97$ nm [30] CdS $a=4.16$ nm and $c=6.61$ nm [32, 33], it becomes clear that CdSe consistently has the larger bulk lattice constant. Hence in a CdSe/CdS core-shell QD this means that the CdSe core is under compressive strain and the CdS shell under tensile strain.

The amount of strain depends strongly on the geometry of the QD, for spherical QDs this breaks down to the relation between core radius and shell thickness. As a rule of thumb, the material that occupies the highest volume, is the least strained and concomitantly puts the other material under

heavy strain. So for one specific CdSe core, the compressive strain increases for increasing CdS shell thickness, at the same time the shell's strain is reduced. However, the growth temperature also plays a role, because during growth the atoms arrange themselves to reach the minimal potential energy at this temperature, which can differ for different temperatures due to different thermal expansions (see also Sec. 9). Since the strain in materials influences the materials' electronic properties and also influences the overall crystal quality (for instance structural defects can be caused by relaxation of heavy strain), it is important to understand this quantity. These dependencies will be discussed in more detail in Sec. 8.2, including the differences between the two crystal structures as well as the temperature dependency of the strain.

The improvement of the QY for core-shell QD has been found to be especially large for high shell thicknesses, and so-called “giant” shell QDs, which show a strong reduction of blinking behavior during emission.[34–37] This “blinking” can be identified in the observation of the emission of single QDs; the observed QD doesn't emit continually, but shown times without luminescent recombination in between, so-called “off” times. In ensemble measurements this behavior manifests itself by an effective reduction of QY. The origin of the blinking is often explained by recombination of electrons and holes through an Auger process.[38, 39]

For instance Cragg and Efros have provided a description of the process, and find that the Auger recombination rate depends on the size and the shape of the confinement potential. A soft potential barrier should reduce the amount of Auger recombinations drastically by three orders of magnitude. This soft barrier can be achieved by a graded interface layer between the core and the shell material, and would lead to a slow transition in electronic properties between the two materials. This points out the importance of a precise knowledge of the interface. Additionally, they find strong oscillations in Auger recombination rate, when the potential size is reduced. So in principle, it is possible to suppress Auger recombination by choosing the right “magic size”. [40]

Already in 2011 García-Santamaría et al. found a strong reduction in blinking behavior and a decreased Auger recombination for their CdSe/CdS core-shell QDs (also called dot-in-dots) and attributed their findings to a graded interface between core and shell. Which they see evidenced by the observation of CdSe and CdS LO phonon replica as well as a mixed overtone in fluorescence line narrowing measurements (FLN) and interpret those as an alloyed phonon modes at the interface.[41] Even though, his assignment of the phonon modes might be debatable, since second-order mixed CdSe-CdS modes yield similar energies, the resulting conclusion is in line with previous ideas. Wang et al. for instance have come to a similar interpretation of their results on CdZnSe/ZnSe QDs where they attribute the reduction in Auger recombination rate to the presence of a graded transition between core and

shell.[42]

Furthermore, Tschirner et al. demonstrated evidence of an alloyed interface layer by Raman spectroscopy combined with ab initio calculations.[43] In a series of different shell thicknesses added to the same QD, they find a mode in the Raman spectrum that increases in intensity for higher shell thicknesses and correlate this with calculation on alloyed bulk material frequencies, while also addressing the occurring strain in the hetero structure in the paper.

Finally, Mourad et al. find effects of an randomly alloyed interface layer for CdSe/CdS QDs which is visible in absorption measurements. In the measurements additional transitions appear for alloyed $\text{CdSe}_x\text{S}_{1-x}$ QDs[44] and they interpret those states to deeper valence band states to the lowest conduction band. The absorption measurements reflect their findings from tight-binding calculations. The corresponding absorption lines shift between the lowest main transitions of the alloyed QD. The breaking of symmetry of the charge carrier wave function compare to the pure binary QDs leads to a relaxation selection rules, so that formerly prohibited transition become relevant and observed.

In 2016 this view is completed by a study from Vaxenburg et al (with Efros and Rodina), who find the Auger recombination rate originates from the non radiative recombination of the biexciton (BX) ground state in the CdSe/CdS QDs. Taking into account the biexciton fine structure, that is caused by the asymmetry of the QD (caused by crystal field or non-spherical shape) and the hole-hole interaction, they find these BX are energetically identical to negative trion states. The negative trion recombination channel however is suppressed when the hole is stronger localized than the electron. The height of the Auger recombination rate depends on the core size as well as the shell thickness and shows an oscillatory behavior depending on both quantities, which originates from the overlap between of the three single-particle states and the wave function (oscillation) of the excited charge carriers. An additional influence is posed by the temperature, which generally enhances Auger recombination rate.[45]

All those works imply a very strong dependence on the interface and the surface of the QD. If it is not intentionally grown, the question is where this alloyed interface layer stems from and how to enhance it. A possible origin of an alloyed interface can be interdiffusion of atoms due to elevated temperature during the synthesis. The issue demonstrates that a deeper understanding and knowledge on the interplay between core and shell is mandatory to improve the QDs on all fronts.

5 Theoretical background: Raman spectroscopy

In this Section the theoretical ground work will be introduced, that will be used for the evaluation of Raman spectra presented in the work. First the theoretical description of Raman effect in bulk crystals will be addressed, as the effect lays ground to many of the measurements presented here. This will be followed by two Sections focussing on properties, which can be determined from the observed Raman spectra. The strain on the crystal lattice, which can be determined via an energetic shift of the phonon mode on the one hand and the coupling strength between excitons and phonons, which manifests in the higher order Raman intensities observed on the other hand.

5.1 Raman effect in bulk crystals, Raman spectroscopy setup and interpretation

The Raman effect is based on the scattering of photon with the collective vibrations, the phonons, of a crystal lattice of a solid. In the process of this interaction of the photon with the solid, a lattice vibration is either generated or exterminated fulfilling momentum- and energy-conservation. Thus, when analyzing the change energy experienced by the light, the effect provides direct information on the lattice vibrations of the examined solid. This process occurs additionally to the elastic scattering of photons at the matter without energy transmission, which is called Rayleigh-scattering, and leads to photons with the same energy but different momentum after scattering as compared to the initial photon. Due to higher probability, the elastic scattering process dominates the spectrum of scattered light, with an intensity higher by the order of magnitude of 10^6 than the Raman scattered light. In the macroscopic theory the interaction of light with a material is described as an interaction between the electronic wave with the polarization of a solid medium via the susceptibility.

$$P(r, t) = \chi(k_i, \omega_i) E_i(k_i, \omega_i) \quad (1)$$

Where $\chi(k_i, \omega_i)$ is the susceptibility of the medium, $P(r, t)$ polarization of the medium (at position r and time t), and $E_i(k_i, \omega_i)$ electromagnetic field as a harmonic wave with the field vector k_i and frequency ω_i .

This susceptibility however depends on the position of the atoms within the solid, which in return is altered by the vibration of the lattice. The interaction can then be considered as a perturbation of susceptibility, caused by phonons.

$$Q(r, t)_m = Q(q, \omega_0) \cdot \cos(qr - \omega_0 t) \quad (2)$$

The influence of the phonons on the crystal lattice is well described using the normal coordinates of the vibrations $Q(r, t)_m$ (q wave vector and ω_0 the eigen frequency of the harmonic phonon mode m) and the effect of a phonon

on the susceptibility can be approximated with Taylor series on dependence of $Q(r, t)$:

$$\chi(k_i, \omega_i) = \chi_0(k_i, \omega_i) + \left(\frac{\delta\chi}{\delta Q} \right) \Big|_0 Q(r, t) + \dots \quad (3)$$

This splits the polarization in to parts, one unperturbed, which corresponds to the part of the Rayleigh scattered light and one part induced by interaction with phonons, which is the Raman scattered part of the light:

$$P_0(r, t) = \chi_0(k_i, \omega_i) E_i(k_i, \omega_i) \cdot \cos(k_i r - \omega_i t) \quad (4)$$

$$P_{induced}(r, t) = \left(\frac{\delta\chi}{\delta Q} \right) \Big|_0 Q(r, t) E_i(k_i, \omega_i) \cdot \cos(k_i r - \omega_i t) \quad (5)$$

Together with Eq. , this can be reformulated as:

$$P_{induced}(r, t) = \frac{1}{2} \left(\frac{\delta\chi}{\delta Q} \right) \Big|_0 Q(q, \omega_0) E_i(k_i, \omega_i) \quad (6)$$

$$[\cos\{(k+q)r - (\omega_i + \omega_0)t\} + \cos\{(k-q)r - (\omega_i - \omega_0)t\}] \quad (7)$$

For the electromagnetic wave, this means the incoming wave is split into one wave with the wavevector $k_s(AS) = k_i + q$ and the frequency $\omega_s(AS) = \omega_i - \omega_0$, and another wave with $k_s(S) = k_i - q$ and $\omega_s(S) = \omega_i + \omega_0$. In case of $k_s(AS)$ the wave gains the momentum q and the energy of one phonon (in the form of ω_0), for $k_s(S)$ the wave gives a momentum q and the energy of one phonon to the lattice, and hence creates one phonon. These formula show that momentum and energy conservation are intact in the Raman process. In case a vibration is created, the process is called Stokes, when a vibration is exterminated the process is called Anti-Stokes, while ω_0 corresponds to the Raman shift.

Since the wavevector of the incoming electromagnetic wave (after $k_{photon} = 2\pi/\lambda_{photon}$) is about two orders of magnitude larger than the size of first Brillouin zone, as a result of the momentum conservation, the interaction with one phonon at the center of the Brillouin zone, the Γ -point is possible. For Raman processes of higher order, so including more than one phonon, in principle the interaction can take place with phonon from the whole Brillouin zone. In the macroscopic description those processes are captured by the development of the Taylor series in Eq. 3 to higher orders.

Additionally Equation 3 leads to the definition of the Raman tensor R ,

$$R = \left(\frac{\delta\chi}{\delta Q} \right) \Big|_0 R_{ij} = \left(\frac{\delta\chi_{ij}}{\delta Q_m} \right) \Big|_0 \quad (8)$$

which is the derivative of the susceptibility in all dimensions from normal coordinates of all phonon modes m . It represents the symmetry of a given crystal structure and can be determined under consideration of group theory. It is used to calculate the measurable intensity of the Raman scattered

light $I \propto |e_i \cdot R \cdot e_s|$, for an experimental geometry, given by e_i and e_s as the polarization of the incoming and the scattered light. This results the selection rules, that show under which an interaction between incoming light and the matter can be observed.

When the energy of the incoming light corresponds to an electronic state of the analyzed material, the Raman process becomes resonant and the intensity of Raman scattered light becomes dramatically increased due to a much higher interaction cross section. This is also true for a process where the energy of the Raman scattered light equals an electronic transition. This effect become even more important, when the analyzed subject is not a crystalline bulk material, but a molecule since their electronic states are much further separated. Also the vibrations of molecules can be investigated with Raman spectroscopy, in fact the Raman effect was originally discovered for molecules (Nobel price in 1930).

In this way, Raman spectroscopy can be applied to many different fields. Here it is used for the investigation of nanocrystals, where it reveals size dependences for the lattice phonons, the different strain conditions that occur for core-shell crystals and even surface modifications on the nanocrystal can be observed.

5.2 Strain determination from Raman spectroscopy

Generally, the change in phonon frequency $\Delta\omega$ in relative to the phonon frequency of the corresponding unstrained material ω caused by a change of lattice constant (Δa) relative to the optimal, unstrained lattice constant a , can be described according to Scamargio et al., using the Grüneisen parameters for the LO phonon of CdSe and CdS $\gamma_{\text{CdSe}} = 1.1$ [46] and $\gamma_{\text{CdS}} = 1.37$ [47].

$$\frac{\Delta\omega}{\omega} = \left(1 + 3\frac{\Delta a}{a}\right)^{-\gamma} - 1 \quad (9)$$

[48] This uses $\Delta\omega = \omega - \omega_0$, the relative Raman frequency shift of a sample (ω) compared to an unstrained reference(ω_0), such as the corresponding bare core for CdSe or bulk material for CdS, and gives $\Delta a = a - a_0$, the epitaxial strain due to the lattice mismatch (a_0 is the free-strain and a is the strained lattice parameter). The choice of unstrained reference here, in contrast to bulk-like structures, is complicated by the fact that the phonon should be affected by confinement. An overview over results of different studies is given by Dzhagan et al. [49] and illustrates that independently of the method used for determination of the phonon frequency, the variation for diameters smaller than 10 nm is non negligible. The majority of studies find a variation of 203 to 211 cm^{-1} just between the diameters between 2 and 7 nm. This overview can be found and be discussed in more detail in Sec.8.2 and 9.

5.3 Exciton-phonon coupling strength determined from Raman spectroscopy

The coupling between excited carriers and the crystal lattice can be understood as Fröhlich interaction[50]. It describes the interaction of the polarization caused by an electron-hole pair in a dielectric environment with the exciton itself. A local point charge causes a force on the ions in its surrounding and the resulting displacement creates a polarization which acts on the charge itself. A longitudinal optical (LO) vibration of a chain of atoms in a polar crystal results in a polarity which can *e.g.* couple to photons. This vibration is changed, when the equilibrium positions of the atoms are displaced due the presence of a point charge. But also the point charge feels a force, induced by the polarization caused by the LO vibration and hence its properties are influenced, resulting in a complex entanglement.

Huang and Rhys addressed the problem of the change of an electronic transition, when it is coupled to a lattice with perturbation theory[51]. They introduced a dimensionless parameter S to adjust their equations to experimental observations. This parameter is now called Huang-Rhys factor and is used to quantify the coupling strength. The Huang-Rhys factor can be estimated from Raman spectra, but a quantum mechanical description is needed to translate observations of the measurement.

The interaction of point charge and lattice is different for vibrations of different symmetry, higher-order vibrations. This results in different-order phonon processes being disturbed differently, which is reflected in changed intensities of the related Raman bands[52]. This then allows the calculation of the coupling strength from the intensities in a Raman spectrum. For a system with electronic transitions, in a certain lattice configuration, the energy of the ground state reads as:

$$E_i = \frac{1}{2}m\omega_{LO}^2q^2, \quad (10)$$

while the energy in the excited state is

$$E_j = E_{ij} - \sqrt{2}\Delta\omega_{LO} \left(\frac{m\omega_{LO}}{\hbar}\right)^{\frac{1}{2}}q + \frac{1}{2}m\omega_{LO}^2q^2 \quad (11)$$

with the excited state energy E_{ij} , the phonon frequency ω_{LO} and q as the normal mode coordinate of the lattice vibration. The overlap between the wavefunctions of the lattice vibration and the electronic excitation can then be calculated following Frank-Condon theory. The corresponding eigenfunctions to the energies of excited and ground state are given by

$$\varphi_n(p) = \left(\frac{\sqrt{m\omega/\hbar}}{\sqrt{\pi}2^n}\right)^{\frac{1}{2}} e^{\frac{1}{2}\frac{\hbar}{m\omega}q^2} H_n \left(\sqrt{\frac{\hbar}{m\omega}}q\right) \quad (12)$$

$H_\alpha(q)$ being Hermite polynomials. In general, the overlap between the wavefunctions of two linearly displaced harmonic oscillators can be expressed by

$$\langle n|m \rangle = \int_{-\infty}^{\infty} \varphi_m(q)\varphi_n(q) dq \quad (13)$$

Following the works of Keil *et al.* and Martin *et al.*[52, 53], this integral can be solved using the following relation between Hermite- and Laguerre-polynomials: $\int_{-\infty}^{\infty} e^{-x^2} H_m(x+y)H_n(x+z)dx = 2^n \sqrt{\pi} m! z^{n-m} L_m^{n-m}(-2yz)$ [54], which leads to:

$$\langle n|m \rangle = \left(\frac{m!}{n!} \right)^{\frac{1}{2}} e^{-\frac{1}{2}\Delta^2} \Delta^{n-m} L_m^{n-m} \Delta^2. \quad (14)$$

with Δ being a dimensionless parameter describing the displacement of the excited harmonic oscillator potential caused by the lattice vibration.

This Frank-Condon overlap is part of the Raman scattering cross section in scattering theory. Following Klein *et al.* and Albrecht *et al.*, the Raman scattering cross section for an n-order process at temperatures near 0 K is[55, 56]:

$$|\sigma^n(\omega)|^2 = \mu^4 \left| \sum_{m=0}^{\infty} \frac{\langle n|m \rangle \langle m|0 \rangle}{E_{ij} + m\hbar\omega_{LO} - \hbar\omega + i\Gamma} \right|^2 \quad (15)$$

with the incident photon energy $\hbar\omega$, the homogeneous linewidth Γ of the optical transition, the electronic transition dipole moment μ and m as intermediate vibrational level in the excited state. It can be shown that $S = \frac{\Delta^2}{2}$ applies. The ratio of the intensities of different-order LO Raman bands then yields an expression that only depends on the value of Δ and known quantities and thus allows an evaluation of the coupling strength.

Many publications follow this proceeding, first introduced by Merlin *et al.* and Alivisatos *et al.*[57, 58]. However, a factor in the reported equations is inverted. The Frank-Condon overlap (14) differs in numerator and denominator of the factor $\frac{m!}{n!}$ and in the upper index of the Laguerre polynomial. Furthermore, a recent calculation based on a Brownian oscillator model by Kelley *et al.*[59] suggests that this expression might be underestimating the influence of the spectral broadening of the electronic bands. It is represented as Γ in the Raman-cross section in (15) and mainly varies due to size- and shape variations. This could give rise to changes in the absolute value of the Huang-Rhys factor. However, relative comparisons should be appropriate and general quantitative comparisons should not be inhibited[59].

6 Experimental methods

As mentioned before, a big part of this work is the characterization of the CdSe/CdS QDs by means of Raman spectroscopy. This method provides a wide range of information on the crystal properties through probing the phonons of the examined QD sample. Like this, it is possible to gain information like lattice strain for core and shell, that are not easily available by other techniques. Determining the influence of a shell on the core lattice parameter could otherwise only be performed by HRTEM, which would entail high evaluation effort and statistics. Especially the lack of possibility to align the spherical QDs according to their crystal axis, makes it difficult to measure atomic distances accurately.

Although optical techniques such as PL and absorption also provide an indirect indication of strain in the structure in form of a strain-induced shift of transitions, they predominately show the cores properties because of the higher carrier concentration and lower transition energies in the core. Additionally, to the investigation of everything that influences the lattice phonons in the sample, the intensity in Raman spectroscopy can be used to determine the exciton-phonon coupling or electronic density of states through analysis of resonant conditions.

An additional method used in this work for the characterization of the QDs is photoluminescence spectroscopy, which provides insights on the electronic fine structure, which will be presented in chapter 11. As well as the observation of phonons under resonance conditions.

6.1 Raman spectroscopy setup

In order to analyze the Raman signal of a sample, a coherent light source with high intensity is needed, which is provided by a laser. This is necessary to on the one hand gain the a high signal intensity and on the other hand to be able to separated the elastically scattered from the inelastically scattered light to be analyzed. In some setups this separation is realized with the help of a notch filter, that is reflective for a corresponding laser wavelength but transmissive for all other light, which is positioned to suppress the excitation laser wavelength in the scattered signal coming from the sample. Since the quality of the filters is limited to a certain width, the edge of the filter can't be infinitely close to the laser wavelength, so only Raman signals can be observed that aren't too close to the excitation and thus suppressed can be observed.

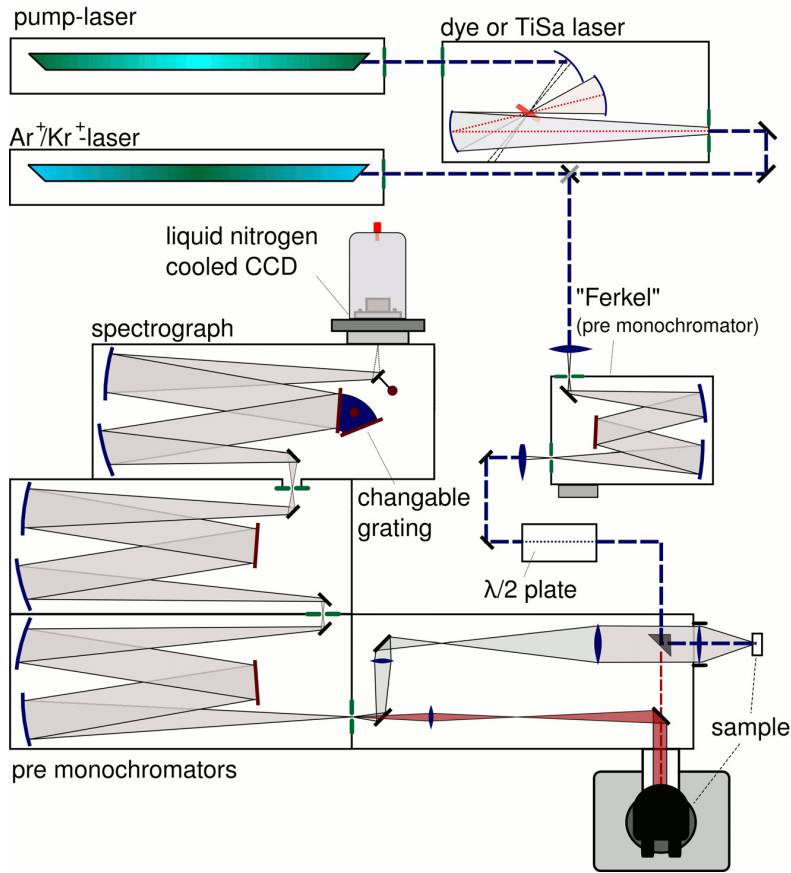


Figure 6: Experimental Raman setup using a triple monochromator, used for several measurement within this work. The optical path way marked with blue dashed belongs to the macro setup, the red dashed line show the pathway of the micro setup. The makro setup is used for the *in situ* Raman measurements in particular because of the higher spatial demands for the synthesis. Taken from [60]

Here however, a triple monochromator (Dilor XY) is used instead. The first two monochromators are used in substrative mode and act as a bandfilter for the excitation wavelength and suppress stray light. This filter can be finely tuned and even signals close to the excitation can be separated, depending on the quality of alignment and the hole widths. This is in contrast to the notch filter which is specific for the excitation wavelength. The third monochromator is used to disperse the signal for energetic resolution. The dispersiveness is determined by the grating used and the spectral region to be analyzed. Fig. 6 shows the setup used for the majority of the Raman measurements presented in this work. It uses a grating with 1800 grooves/mm and neon and argon lines are used for calibration to absolute energies.

The scattered and dispersed light is detected with a nitrogen cooled silicon based charge coupled device, positioned behind the third monochromator. The setup provides a resolution of 0.4 cm^{-1} and in principle can be used in two different modes.

Either the sample is placed under a microscope (Fig. 6, optical pathway in blue), which provides the opportunity to excite and detect locally with a focus laser spot with down to μm width and thus gives lateral resolution on the sample for observation of small samples or microstructures. The other mode, here called macro-mode (Fig. 6, optical pathway in red), instead of the microscope uses a lens with a focus distance of 5 cm. This leads to a wider spot on the sample that is illuminated and hence a larger area that the signal is collected from. In this way the local power density is lower and the risk of damage is reduced. At the same time the Raman signal is averaged over larger areas of the sample. This mode can be used for samples without local structures or samples that are dissolved. Since in this work focusses on colloidal QD with sizes far below optical resolution, most measurements presented here are recorded using this mode.

For excitation an Ar-Ion laser (Coherent Innova, Spectra Physics Stabilit) was used, offering different laser lines between 457 and 647 nm. For suppression of plasma lines, originating from the laser tube, a prism pre-monochromator is used as a filter.

For low-temperature measurements, the samples are cooled in an Oxford microcryostat with liquid helium in an isolating vacuum, or with a Linkam stage with liquid nitrogen for higher temperatures. We estimate the temperature accuracy to account to $\pm 5 \text{ K}$ for both cryostats.

6.2 Photoluminescence excitation spectroscopy (PLE) setup

The extensive investigation with Raman spectroscopy in this work will be completed with photoluminescence excitation spectroscopy (PLE), to add the analysis of electronic properties of the QDs to the more structural information gained from observation of the phonons.

Regular photoluminescence (PL) measurements use a fixed excitation wavelength and analyze the light that is emitted by the investigated sample under this given excitation. Especially when the excitation is close to resonance with states with high occupation probability such as the ground state, the PL spectra are strongly dependent on the excitation wavelength. The analysis of this dependency can be performed with a method called photoluminescence excitation spectroscopy (PLE). By variation of excitation wavelength, this method can reveal insights in the electronics states of the sample beyond the ground state, including information on electronic states bi- and triexcitation states, different trap or defect states, or states induced by doping.

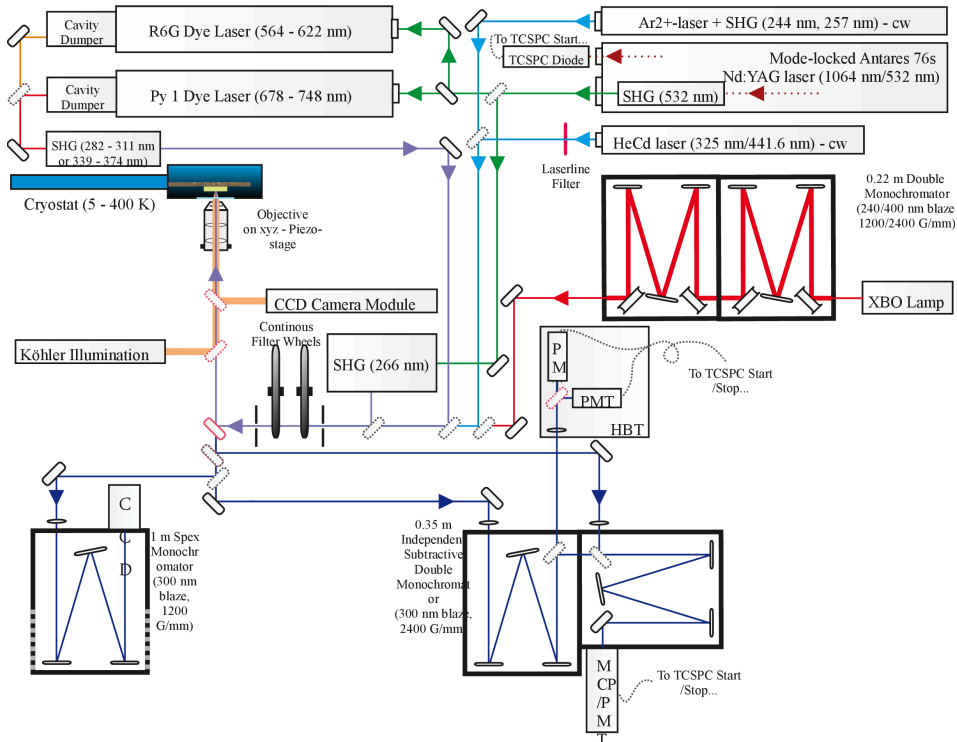


Figure 7: Setup used for the PLE measurements in this work. As light source the XBO lamp was used in combination with a double monochromator (red lines) for monochromatization. The samples were cooled in a self-stabilized cryostat with liquid helium. The collected signal was analyzed with a spex monochromator and CCD(left). Image from Gordon Callson, private communication.

Additionally, energy dependent modulations in intensity give information on the exciton phonon coupling strength to state in resonance. This quantity can simply be determined comparing the intensities of the transition and the phonon replica. Thereby the probabilities of the process of excitation and subsequent emission of a photon with and without generation of a phonon are compared, which directly gives a measure of the interaction probability of the generated exciton with the phononic system. This means the method provides complementary information to results gained from Raman measurements, where the monitored process is different, as described in Sec.5.3. Additionally coupling factors derived from Raman spectroscopy are seldom determined under resonant excitation in the ground state as for many systems under these conditions the Raman signal is overpowered by a highly efficient PL and hence hard to decipher.

The PLE setup (see Fig. 7) is similar to a regular PL setup, but with an exci-

tation source, which has to offer continuously tunable excitation energy and a high power output. The light must be either monochromatic or go through a monochromator, for a high resolution of the excitation energy dependence. Here, a Hg high-pressure lamp with parallelization optic and monochromator combination is used. With a slit width of 1 mm and a grating $150 \frac{1}{mm}$ of the monochromator, the excitation axis can reach resolutions up to 5 meV in the spectral range used in this work. The monochromatized light is focussed on the sample, which is positioned in a self-stabilized liquid He flow cryostat. The resulting signal from the sample is collected under a small angle (about 10°) in relation to the excitation (approximately back-scattering geometry) and subsequently spectrally decomposed in a monochromator ($1800 \frac{1}{mm}$, slit $180 \mu m$) and detected with a CCD. For the measurement, the excitation energy is tuned stepwise and spectra are recorded with a fixed detection monochromator position. This results in 2d data, with the detected signal in one axis, stacked according to their excitation energy.

7 Synthesis of CdS/CdSe colloidal QDs and subsequent Silica encapsulation

Colloidal QD are QD synthesized and kept stable in a solution. This synthesis however has an impact on the properties of the final sample. For instance the synthesis conditions can be used to tune the size of the QD, as well as the crystal structure and the shape of the QD. An Additional challenge is to achieve a size distribution within the ensemble, that is as small as possible. These subjects have undergone a lot of research during in past years, in many parts by the group of Z. Hens, who also provided our samples.

Here, the syntheses and influences of synthesis conditions on CdSe QDs will be presented in the first subsection, focussing on comparable QDs to the ones used in this work. This will be followed by the different synthesis options for a subsequent CdS shell addition for the synthesis of core-shell QDs, which are favored for application because of improved properties. Those synthesis options and influence on the final QDs are then compared (new syntheses from Z.Hens group), including measurements that were performed in the context of this work.

Finally the synthesis of a silica shell around the QD, as needed for application in bio-labelling, will be presented as it is performed for the silica shelled QDs in Sec. 12. The observations on the silica encapsulated QDs presented in this part are based on samples comparable to those used in this work as a prerequisite.

7.1 Synthesis of colloidal QDs

Colloidal QDs of various forms can be synthesized in a setup that is, compared to MOVPE or MBE, less laborious. It consists basically a temperature controlled vessel for temperatures typically between 200 and 400°C, that is sealed to reduce desorption of the solvent into the environment, and syringes for controlled precursor injection (example see Fig. 8 left). The vessel is filled with a mixture of solvent and ligands, both with boiling points above synthesis temperature. Often chloroform, hexane or toluene are used as solvent and oleic acid, **trioctylphosphine** (TOP), **trioctylphosphine oxide** (TOPO) or **oleic acid** (OA) as ligand (molecules see Fig.8 left). The precursor consists of the inorganic constituents of the intended QD, bond to an organic surfactant, that mediates the growth. As precursor for CdSe QDs, cadmium oleate and selenium is dissolved in **octadecene** (ODE-Se) are widely used.

The choice of solvent, ligand and precursor, as well as the temperature and time of the synthesis determines the crystal structure, shape and size of the final QD. By adjusting these parameters, the properties of the final QD can be finely tuned.[61–64]

For QDs, consisting of a single material, the procedure of choice is the seeded growth method, which consists of two main steps. First, there is the nu-

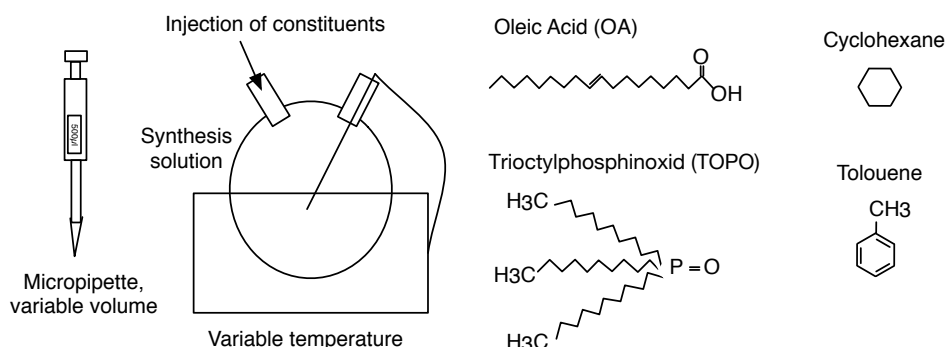


Figure 8: Left: Schematics of a vessel used for synthesis of colloidal QDs. The vessel is sealed with stopper, but provides the possibility to inject the constituents of the synthesis. The volumes of each ingredient are precisely measured with a micropipette with appropriate volume and interchangeable tip to prevent contaminations. The vessel is heatable and the temperature is constantly observed. Right: Chemical structure of ligand and solvent molecules typically used for colloidal QD stabilization.

cleation of the crystal seeds, followed by a subsequent growth phase in the second step. The nucleation takes place, when the temperature of the reacting solution exceeds a critical temperature. At this temperature, the both precursors convert to active monomers efficiently. After surpassing a certain level of supersaturation, the monomers spontaneously start to form crystal nuclei, which consumes energy and causes the temperature to drop and stops the nucleation. A high degree of supersaturation is reached by applying the “hot injection” method [65–68], where the precursors are injected to a hot reaction solution of solvents and ligands. This concentrates the nucleation to a short time frame, thus this effect is called “burst nucleation”.

The remaining active monomers in the solution can now deposit on the nuclei, growing the crystal. The effect that smaller QDs grow faster leads to a smaller and smaller size distribution and is called “focussing”. When the desired size is reached, the reaction can be stopped by rapidly cooling down the solution. If the solution remains at growth temperature, once the monomers have been incorporated, a ripening process begins. This causes some crystals to grow, while others shrink and provide active monomers for the growing crystals. This process is called “Oswald ripening” (also present for MOVPE or MBE growth of QDs) and is essentially a “defocussing”-influence on the size distribution, as it increases the halfwidth of the distribution. For a small size distribution at optimum, this ripening growth regime should be avoided. The reaction chemistry and how it can be engineered to tune final size and broadness of the size distribution has been the subject of many studies.[61–64]

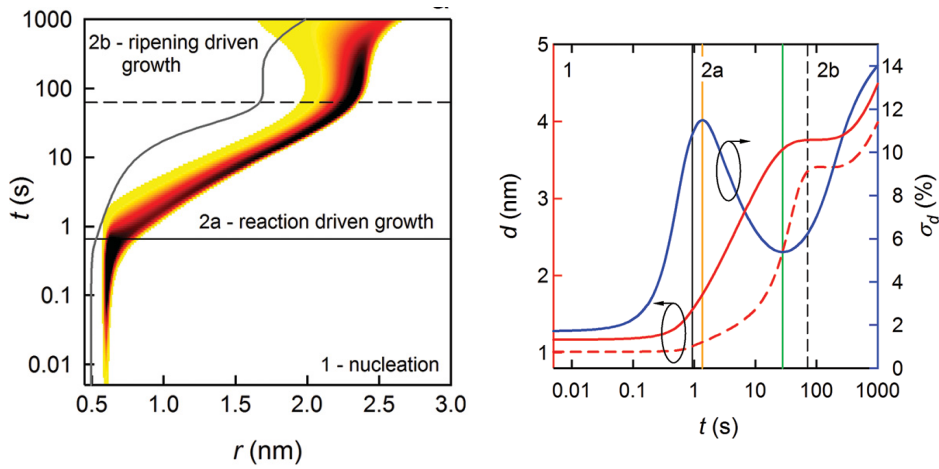


Figure 9: Left: Concentration distribution $c(r,t)$ obtained with the initial parameters as given in the Supporting Information. The color scale indicates an increase of c in the direction yellow orange red black. The gray line marks the critical radius (r_c). Right: diameter in dependence of the synthesis time with clear focussing of the diameter [62]

Abé et al.[62] for instance have investigated the size development with a combined approach of experiments and numeric modeling with a rate equation model. This lead to a description of the size distribution during synthesis time, as shown in Fig. 9 left, with the before mentioned phases of nucleation (1), reaction driven growth (2a) and ripening driven growth (2b). The findings accentuate the necessity to choose the right time to stop the reaction in order to achieve a sharp size distribution. Figure 9 right shows the mean diameter and the dispersion as a function of reaction time, with the growth phases marked as in Fig. 9. This shows well, that for minimal dispersion, the growth should be stopped before the ripening phase starts, as a clear minimum in size dispersion is visible due to the “focussing”-process. They also find that the nucleation can be tuned by the rate of active monomers or the solute formation, whereas the exact temperature of injection and growth doesnt influence the diameter after focussing much, as the change in temperature automatically modifies the growth rate. The diameter however is increased by decreasing the monomer formation rate, as Abé et al. [62] found that the CdSe formation rate depends in first order on the Cd and Se precursor concentrations. In the following year they find yet a different way in crease the QD size and show that increasing the amount of free acids in the synthesis effectively has the same influence on the reaction as the increase of solute solubility.[63] As the free acids are responsible for the coordination of the cation precursors, Abé *et al.* conclude that the increased size is due to an increased solute consumption that leads to the

formation of fewer QDs and thus larger final sizes. This, however, reduces the “focussing”-effect and thus increases the size distribution of the final QD, and hence should not be the preferred method of increasing the QD’s final size.

These results lay the fundament for a well-controlled growth of QDs with predetermined final sizes, which is essential for any application. They also provide simulation models that can be applied to study the synthesis and predict the outcome of a set synthesis. Since for applications of colloidal QDs on a larger scale, upscaling and automation is essential, the optimization of the synthesis for an optimal postfocussed diameter and optimal chemical yield, as well as a precise control over the crystal structure, is an absolute prerequisite.

7.1.1 Exemplary CdSe QD syntheses

Looking at a procedure that is often followed or used slightly adapted, a more detailed insight into the chemical procedure can be gained. This procedure was described first by Jasienak et al. and produces zincblende CdSe QDs. First the Se precursor needs to be prepared by dissolving selenium in octadecene (forming ODE-Se). In preparation of the synthesis, the cadmium oleate $\text{Cd}(\text{OA})_2$ precursor is liquified at 100°C , and added to further octadecene (ODE). The mixture is degassed for 1 h at 100°C under (dry) nitrogen atmosphere. Afterwards the temperature is increased to 265°C , and the ODE-Se is injected to start the synthesis. This procedure is also called “hot injection”, as the precursors are injected to the hot reaction solution. The temperature of the mixture drops after injection automatically (ODE-Se is at room temperature). The CdSe QD growth continues at 235°C until it is stopped by rapid cooling. The zincblende CdSe NCs produced by this method are stabilized by oleate ligands on the surface.

For wurtzite CdSe QDs a similar procedure is used, as described in References [69, 70]. Here, the Cd precursor is prepared by mixing CdO with TOPO and ODPA and heating the mixture for one hour under vacuum. The solution is subsequently heated to 345°C under nitrogen atmosphere and TOP is injected in preparation for the synthesis. Then, the Se precursor (Se dissolved in TOP) is added to the solution to start the synthesis, which just as for zincblende QDs can be stopped again by rapid cooling. The wurtzite QDs resulting from this synthesis are stabilized by a mixture of TOP and TOPO.

After the synthesis, the both types of QDs need to be purified to remove the excess precursor and ligand molecules. This is realized by precipitation through the addition of solvent, which is followed by centrifugation to achieve a separation of the QDs from the solution (including residue precursors and ligands) due to their higher density. The separated QDs are

resuspended by addition of further solvent. This leads to a QD solution with reduced, but not fully removed content of remaining synthesis products. Hence these purification steps are repeated several times (often 3), to successively purify the QD solution.

However, the synthesis of single material QDs usually only represents the first step in fabrication. The subsequent addition of a semiconductor material will be discussed in the following Section 7.2.

7.2 Semiconductor shell addition methods for bare colloidal QDs and properties of the core-shell QDs

To create colloidal core-shell QDs which show widely improved luminescent properties (as discussed in Sec.4.2), first the bare core QDs are grown, as described in 7.1, then a shell is build around the QD. For this subsequent addition of a shell materials of similar crystal structure, two different options can be found in literature. On the one hand, the Successive Ionic Layer Adsorption and Reaction (SILAR) method is widely used and works on zincblende, as well as wurtzite QDs. The method provides a very precise control over the shell thickness as the atomic layers are deposited one after another. This is realized by the addition just one of the shell-constituents precursor at growth temperature to saturate the surface, subsequently followed by the other constituent, forming monolayer after monolayer. For a CdSe QD to be covered by CdS, this would be the Cd precursor followed by S precursor. The added amounts need to be calculated exactly to reach complete coverage of the QD, otherwise a uniform shell cannot be formed. After each precursor injection, there must be enough time left to ensure complete coverage (often about 10 minutes is used). An alternative to this waiting time would be to use higher concentrations of precursor than needed followed by a rinsing step to remove excessive precursor between each addition of each monolayer. This option however is even more time-consuming and therefore rarely applied. Instead often an annealing step is carried out between to the steps, which is believed to ensures good crystal quality, especially for QDs with high shell thickness (“giant shells”). In order to reduce the synthesis time, different ways have been investigated. The “flash” synthesis, as shown by Cirillo et al., provides a faster shell addition with high crystal quality.

7.2.1 Exemplary SILAR and *flash* synthesis and comparison of resulting properties

For a typical SILAR synthesis for the S precursor, the S is dissolved in octadecene (forming S-ODE). For the Cd precursor, CdO is dissolved in a mixture of OA and/or ODE. Before the reaction, n-octadecylamine (ODA)

and ODE were mixed and degassed for 1 h at 100°C under nitrogen flow. Afterwards the prepared CdSe cores in hexane are added and solution of ODA and ODE and the mixture is degassed for another hour at 100°C. Then the temperature is raised to 225°C and the successive addition of Cd and S precursor is started, with breaks to account for reaction time and possible additional annealing steps for higher crystalline quality.

As before mentioned the advantage of this method is the precise control of the shell thickness (monolayer-accuracy), the downside is labour intensity and time. The synthesis of “giant shell”-QDs is reported to take between 30 min per monolayer[36] and up to 4 hours for low defect materials with intensive annealing steps. Often for optimal morphological and optical properties each step needs to be followed by annealing for 3.5-4h [36], which results in a total synthesis time of over two days for a 15 ML shell thickness.

Avoiding this, Cirillo et al. [69] have demonstrated a method, which enables the direct growth of a wurtzite CdS shell in one single step. The synthesis of the shell takes 3 minutes only and results in good crystal quality and a regularly formed shell, as shown in the TEM images and size dispersion in Fig. 10. The method uses a different Cd precursor, carboxylic acid (OA) and phosphonic acids as surfactant, which lays ground to the isotropic growth of the shells. They also found that an excess amount of OA compared to cadmium is necessary to prevent the formation of individual CdS QDs. The shell thickness can be directly determined by adjusting the Cd amount offered in the synthesis, as it is fully converted in the reaction.

For a typical synthesis, as used in [69, 70], the Cd precursor is prepared

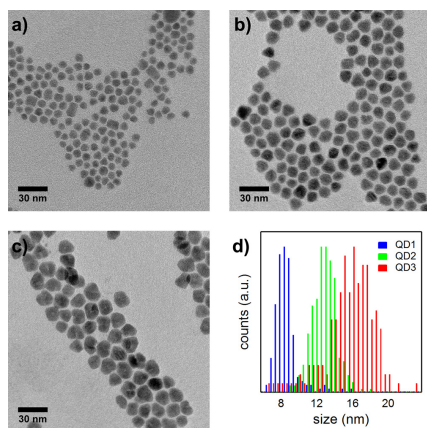


Figure 10: a), b) and c) TEM images of 8.9 ± 1.3 , 13.0 ± 1.4 , and 15.8 ± 2.7 nm total diameter QDs, bases of 2.5 nm CdSe cores and synthesized with the “flash” method, showing uniform shells and no byproducts of the synthesis like smaller CdS QDs, although the distribution for the highest shell thickness becomes broad, d) visualizes the diameter distribution of the samples in a, b, and c, taken from [69]

by heating in oleic acid and in TOPO dissolved CdO to 120°C for one hour while flushing with nitrogen. Subsequently the temperature is raised to 330°C, and TOP is injected as soon as the solution turns clear. This is followed by the addition of the previously prepared QDs (wurtzite) and the S precursor, which consists of S dissolved in TOP. The reaction is stopped after a few minutes by rapid cooling and addition of toluene to accelerate

the cooling. Finally the finished core-shell QDs are purified repeatedly by the addition of isopropanol and methanol, centrifugation and redispersion in toluene.

This entails that the shell synthesis with the “flash” instead of the SILAR method on the one hand is faster, and on the other hand is conducted at higher temperatures. Regarding the finished resulting QD, this could either lead to a sharper interface between core and shell, since the time span is much shorter during which diffusion of core and shell molecules can take place in comparison to SILAR. Or since the temperature of the “flash” procedure is much higher and diffusion of atoms is essentially a temperature activated process, this could lead to a more intense diffusion for a shorter period of time. If this method also results in a smooth graded interface between core and shell, that is comparable to SILAR produced samples, is a question of which of the influences, temperature or time, has a stronger influence on the interface. Since this interface has mainly been investigated for core-shell QDs, that were produced with the SILAR method (see also Sec.4.2) and a smooth transition between two materials seems favorable for the QD QY, this property should be addressed in particular, additional to the more general luminescent attributes of the “flash” produced QDs.

Figure 11 shows absorption and PL spectra of the QDs already depicted

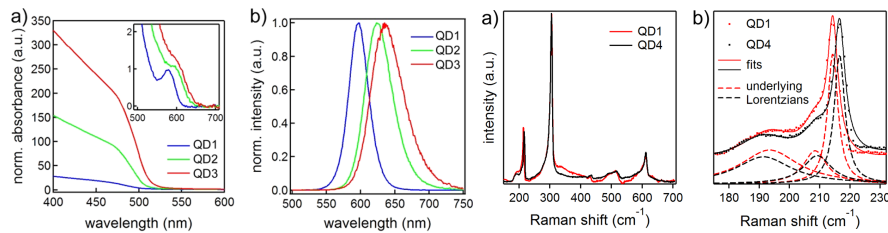


Figure 11: Right: a) Absorption and b) PL spectra of the same QDs shown in Fig. 10, Left: a)+b) Raman spectra of the QD with thinnest shells in the publication together with a close up on the CdSe phonon region including underlying fits for comparison with Tschirner et al. [43], measurement within this context of this work, images taken from [69]

in Fig. 10, revealing a red shift with increasing shell thickness, as expected (Sec. 4.2), and an increasing halfwidth of the energetically lowest transition, as can be expected from the size distributions shown in Fig. 10. The absorption spectra are dominated by the CdS shells absorption, as it represents the highest volume fraction in the QDs. This shows, that regarding the luminescence “flash” grown QDs can have similar properties to those produced with the SILAR method. In order to find out about the interplay between the two lattices, we analyzed the samples with Raman spectroscopy, as previously evidence for an interface formation in SILAR CdSe/CdS QDs has been found in the low energetic shoulder of the CdSe phonon mode (Tschirner et

al. [43], see also Sec. 4.2). Of course apart from a possible interface formation, the interplay of the two lattices causes strain in the core-shell system (Sec.4.2), which can also be analyzed by Raman spectroscopy, but will be discussed Sec. 8 and 9. Figure 11 left shows Raman spectra of the thinner shelled “flash” QDs presented in the publication of Cirillo et al. [69], which are investigated as part of this work. The spectra reveal very similar overall spectra compared to Tschirner et al. [43]. Additionally, a similar interface mode to the one proposed by Tschirner et al. is observed, which again shows the great similarities between the products of this two very different synthesis. Even though the width of the interface cannot be quantified by Raman spectroscopy, due to difficult quantitative interpretation of intensities, the similar Raman spectra show that the QDs do have similar structures and that the much faster “flash” synthesis is most probably a good approach for a simplification of the QD growth.

While in this Section, we addressed the coverage of QDs in crystalline material with similar lattice parameters, predominantly semiconductor materials, in the following Section a different encapsulation entirely will be discussed. The encapsulation of a QD with polymers or silica and other more or less inert materials is primarily used in biological labeling applications and poses a largely different interaction on the QD as the interaction between QD and outer shell is less direct and not completely elucidated yet.

7.3 Silica encapsulation for biological applications

For biological applications, the colloidal QDs need to be covered in a material that provides a chemical barrier to the aqueous and often non PH-neutral environment, while being optically transparent. One of the most promising candidates for encapsulation is silica, a well known and relatively biocompatible material. Silica has been shown to improve stability in polar solvents under various harsh conditions, concerning pH and ionicity for instance. For further discussions on this topical complex, see Sec. 4.1 and chapter 12)

One additional, important advantage of silica as capping material is that the surface of silica can be functionalized with a wide range of chemical groups, including amines and thiols, providing the possibility to couple the biomolecules of interest and for specific targeting of cells or intracellular structures.[71–75] These silica shell-QD complexes will be studied in the final part of this work, together with a detailed analysis of the encapsulation process.

Eventhough there has been much progress in this field of research during the past year, it is unclear in which cases the silica encapsulation preserves or even improves the PL of the QD and how exactly this is influenced. Many groups find indications that differences in PL QY must stem from different surface chemistries, but this surface chemistry and extent of interaction on the surface of the QD is subject to speculations mainly.[73, 74, 76]

In this Section the aim is to address the previous results of the encapsulation

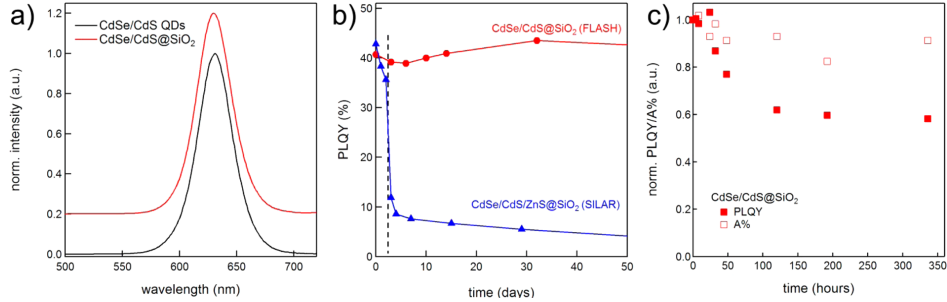


Figure 12: a) normalized PL spectra under UV illumination (454 nm) of a flash-synthesized CdSe/CdS QD with and without silica shell. b) PL QY of different QDs over time. c) normalized PLQY and absorption of the same encapsulated QD as in a over time. Taken from [70] (cooperation partner), The QDs are directly comparable to those used in this work.

synthesis that is also used in the in situ Raman experiment conducted in this work. Aubert et al. have optimized the silica encapsulation for application to “flash” synthesized core-shell QDs and show the resulting composites have a high physicochemical stability. Those “flash” QDs can, opposite to the conventionally used SILAR QDs[77], maintain their high luminescence quantum yield after encapsulation and even after long periods of time in aqueous solution and long term UV irradiation. This is shown in Fig. 12, where Fig. 12a shows the emission wavelength remains approximately the same and Fig. 12b shows the comparative intensities of SILAR and “flash” QDs in water under UV illumination. While the SILAR QDs PLQY is strongly reduced after less than 5 hours, the “flash” QD only reduces to 60% of the original PLQY after 100 h \approx 4days and seems to saturate there (stays constant for over 14 days), as shown in Fig. 12c. This renders the “flash” QD after encapsulation with the described procedure the perfect candidate for long term cell observations. The origin of the different results for SILAR and “flash” synthesized QDs might lie in their very different surface chemistries[78].

The encapsulation synthesis will be described in the Section on the procedure of the in situ Raman experiment (Sec.12.3). It is usually finished by a purification step of precipitation, centrifugation and resuspension, just like for the QD syntheses described in the previous chapters (not covered in *in situ* Raman). Also technical details about the Raman observation of the synthesis are presented in Sec. 12.3. Finally the results of the experiments are presented in Sec.12, showing the formation of an interface between silica and the QD and giving rise to the possibility of a more detailed analysis of influences on the reaction, which could lead to further improvements of the synthesis or at least a better understanding.

8 Structural and electronic properties of CdSe/CdS quantum dots

In the following section, we take a closer look into the properties of the material investigated in this work. Therefore, first the crystal structures and optical properties of CdSe and CdS will be discussed, followed by an overview of the properties unique for colloidal QDs based on those materials. Then, we present typical Raman spectra, we regularly observe for those QDs, and discuss the present phonon modes together their respective origins and show in which way Raman spectroscopy can be used for the analysis of the present material.

8.1 Crystal lattice and optical properties of CdSe/CdS QDs

Cadmium Selenide (CdSe) and Cadmium Sulfide (CdS) can be found in wurtzite as well as zincblende (face-centered cubic, fcc) crystal structure, hence it can crystallize in the hexagonal or the cubic close-packed form. However bulk material can only be found in wurtzite structures; The zincblende structure is found exclusively in nanostructures, usually with a synthesis at lower temperatures and using different surfactants from the wurtzite growth.

Figure 13 shows the two crystal structures schematically for CdS. For the

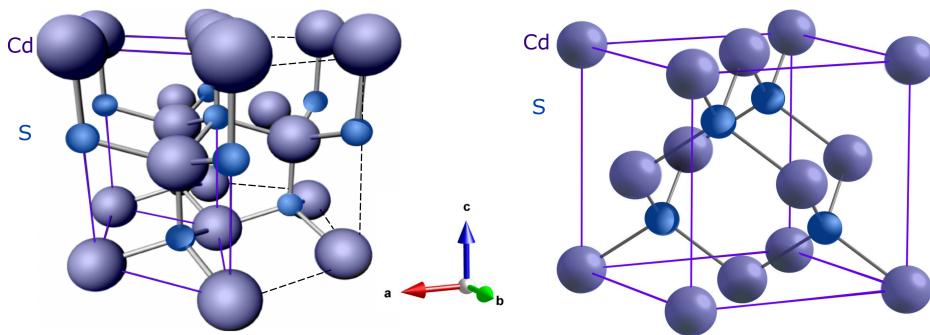


Figure 13: Crystal lattice of wurtzite (left) and zincblende (right) CdS in a ball and stick model. Taken from Narine Ghazarian private communication.

zincblende structure, the atomic distances are the same in all directions, such the structure is isotropic. In contrast to this, the wurtzite structure has one symmetry axis (the c- axis) with a larger lattice constant compared to the other. Along this axis, the layers of the different atom species are arranged in alternating sequence. The covalent bonds between the atoms cause a higher charge density around the S atoms. This means that if the structure ends (surface) with such an atomic layer, there is an unsaturated

particular charge that can influence the interaction with the environment locally. This surface can e.g. provide a reactive surface in the synthesis which is used for the synthesis of elongated crystals. Additionally, this anisotropy leads to pyro- and piezo electricity in the structures, which influence the electronic properties and strongly effects strained core-shell structures.

The lattice constant of zincblende CdSe is $a=0.613$ nm [30] while the zincblende CdS material has a slightly smaller constant of $a=0.583$ nm[31]. For wurtzite bulk CdSe, the lattice constants are $a=0.437$ nm and $c=0.697$ nm [30], and for wurtzite CdS $a=0.416$ nm and $c=0.661$ nm [32, 33]. Hence CdSe consistently has a larger lattice constant compared to CdS. In a CdSe/CdS core-shell QD this results in compressive strain for CdSe cores and tensile strain for CdS shells (see also Sec 4.2, especially Fig. 5) and will cause pronounced influences on the Raman spectrum, as will be shown later on.

Looking at the bonding potentials of the atoms often helps to understand

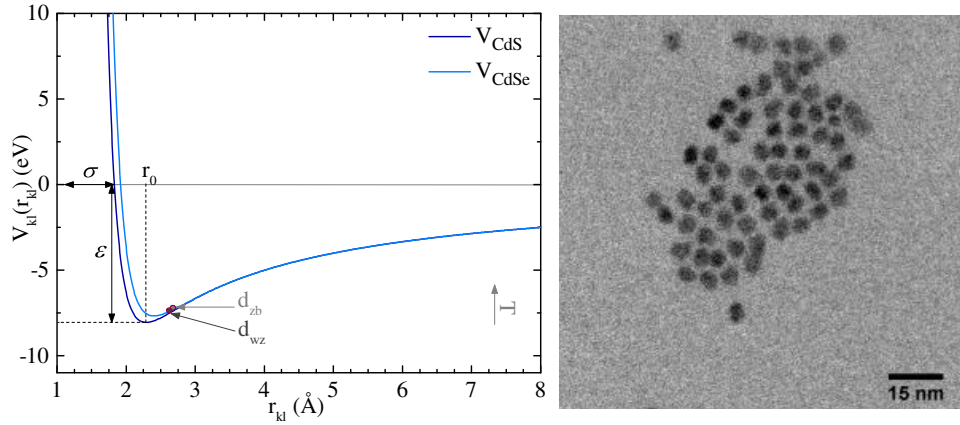


Figure 14: Left: A plot of two-body inter-atomic potential energy for CdSe and CdS as a function of inter-atomic distance. The function of the Lennard-Jones-like inter-atomic potential $V_{ij}(r)$ and the potential parameters were taken from Ref. [79]. T indicates the influence of increasing temperature. Right: TEM image of a wurtzite 5.12 nm diameter CdSe QD without shell. (Part of the WZ core series used in this work).

basic properties such as temperature dependence of a materials. Fig. 14 shows the two-body interatomic potentials for Cd and Se, as well as Cd and S. The potentials are Lennard-Jones-like inter-atomic potentials which consist of a long-range Coulomb interaction term (attractive) and a short-range potential (repulsive) and are modified by parameters to reflect the characteristics of the interaction between the atomic species. The parameter shown here are taken form Grünwald et al.[79]. Those potentials describe the interaction between the two sorts of atoms and show the energetic minimum at the optimal interatomic distance, as well as how much energy is

needed to break the bond and how strong the interaction is in general. A deep minimum means a strong interaction, a shallow potential curve means the material has a high temperature dependence. This will be used and discussed in more detail in Sec. 9.

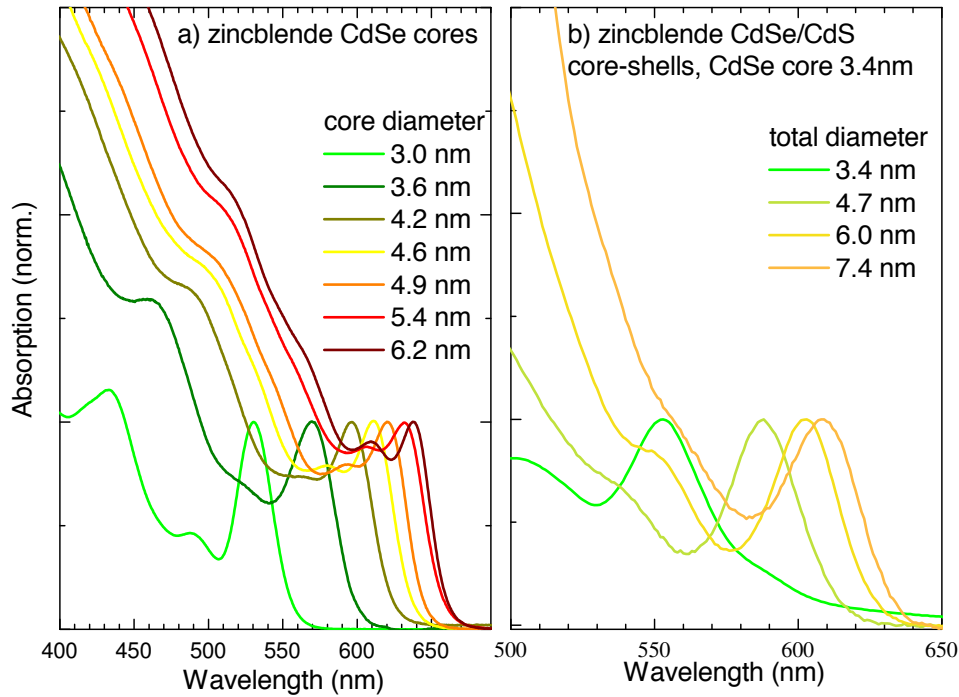


Figure 15: Absorption spectra (room temperature) with UV excitation ($\lambda = 454$ nm) of a) a series of colloidal zincblende CdSe QD with varying diameter without shell measured on QDs in solution at room temperature with UV excitation ($\lambda = 454$ nm). The intensities are normalized to the first transition. As the diameter increases, the first transition shifts towards lower energies because of reduced confinement. b) a series of colloidal zincblende CdSe QD with varying CdS shell thickness on the same core (diameter 3.4 nm) in solution. The intensities are normalized to the first transition. As the shell thickness increases, the first transition shifts towards lower energies because of reduced confinement.

As mentioned in Sec. 4.2, these colloidal QDs are especially interesting because of their well-controllable size dependent properties, most prominently visible in the energy of the lowest electronic transition. This size dependence is caused by the quantum confinement effect and enables to tune the wavelength of emission and absorption. The smaller the “box” (the QD) the charge carriers are confined in, the higher the energetic ground state and the more separated the excited states. This leads to a size dependence of the

absorption spectrum, which is exemplarily shown in Fig. 15a) for a series of differently sized zincblende QDs (same QDs as used in Sec 11) at room temperature. As the QD diameter decreases and the confinement grows, the absorption edge shifts (lowest energetic electronic transition) towards higher energies. Since this dependency is well researched and reproducible regarding the synthesis conditions, the size of synthesized QD is mostly determined from absorption spectra, using a before constructed sizing curve. The effect of an additional CdS shell on a CdSe QD on the absorption spectrum is shown in Fig. 15b). When a shell is added to the QD, the confinement is partially relieved and the states are shifted towards lower energies. The higher the shell thickness, the more pronounced is this effect, which leads to the shift in absorption edge towards lower energies as depicted in Fig. 15b). This means the shell not only stabilizes the QD's surface by way of saturating the surface bonds (Sec.4.2, but it also effects the optical properties through the confinement effect and the phononic properties by causing strain. In the next section (8.2) the phononic properties of CdSe/CdS QDs will be presented and analyzed.

8.2 Raman spectra of pure CdSe QDs and CdSe/CdS core-shell structures

Since the phonon properties play an important role in this work, the Raman spectrum of pure CdSe QDs and CdSe/CdS core-shell structures, wurtzite and zincblende, should be addressed in particular.

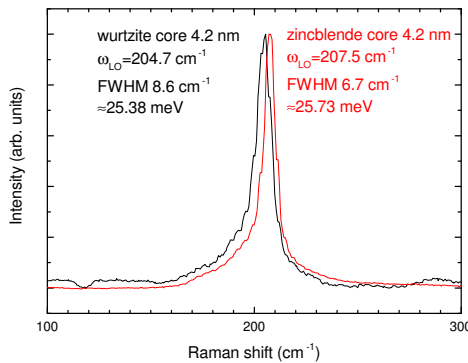


Figure 16: First order Raman spectra of two 4.2 nm diameter CdSe QDs ($T=10K$), one with wurtzite, one with zincblende structure. The phonon frequency of the wurtzite QD is lower than for zincblende and at the same time it exhibits a slightly larger halfwidth, which most probably originates from the crystals structure's anisotropy.

Showing the influence of the different crystal structures on the Raman spectrum of a CdSe QD, Fig. 16 gives the first order Raman spectra of one zincblende and one wurtzite QD of the same diameter $d = 4.2$ nm. Despite the difference in symmetry, the spectra appear very similar between the two samples and are dominated by one single phonon mode. In principle, the Raman spectrum of a wurtzite structures should consist of the A_1 , the

E_1 and the E_2 mode, which can be observed in the experiment under conditions given by the Raman tensor (Sec. 5.1). However, for a sample with randomly distributed QD, as used in Fig. 16 and measurement in backscattering geometry without polarization, all should be allowed. Nevertheless, those modes are neither visible here, nor have they been reported in other previous studies. Instead an “LO-like” mode is observed, very close to the LO mode of the zincblende structure, but with a slightly lower frequency. Considering the different atomic distances of the two symmetries in the same bonding potential (Fig. 14), it becomes apparent that the phonons must be very similar. The “LO-like” phonon mode must, because of the energetic proximity to the LO mode of zincblende, be a phonon mode that mainly vibrates along the c -axis, as the lattice constant along this axis is close to that of the zincblende structure. This has also been found in measurements regarding the size dependence of phonon modes combined with calculation by Trallero-Giner *et al.*[80]. Additionally, to the energetic position of the phonon modes in the Raman spectrum, the halfwidth provides further information. For the wurtzite compared to zincblende QDs, we consistently find similar, but slightly larger halfwidth for wurtzite “LO-like” mode (similar to the $A_1(\text{LO})$ in wurtzite nomenclature). This should originate from the higher anisotropy of the wurtzite structure, which results in a broader distribution of phonon energies.

According to selection rules in zincblende crystals additionally to the LO mode, a TO mode can be observed. For wurtzite CdSe a similar “TO like” phonon can be found, similar to the $A_1(\text{TO})$ in wurtzite nomenclature, comparable to the appearance of the LO mode. For zincblende CdSe the TO modes is reported to appear at about $\approx 170 \text{ cm}^{-1}$ [81], but most often vanishes in the other Raman signal.

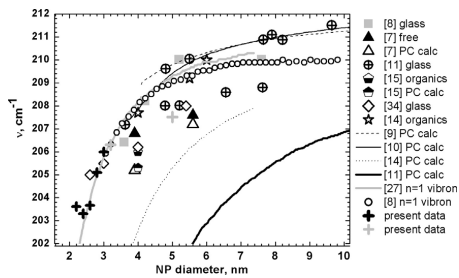


Figure 17: Size dependent phonon frequency of CdSe QDs, collected from several publications. The frequency decreases with decreasing QD size starting from a diameter of 6 nm. Data origins: 8→[80], 7→[82], 11→[83], 15→[84], 34→[85], 14→[86], 9→[87], 10→[88], 27→[89], Taken from Ref.[49]

Furthermore, the observed phonon frequency of the investigated QD varies according to the QD size. This dependence has been observed in many publications and, like the size dependence of the optical properties, is a confinement effect. The dependence is shown in Fig. 17 and reveals a

decreasing phonon frequency for decreasing QD diameter, consistently for all shown data and calculations. The frequency saturates in the bulk frequency depending on the model from a QD diameter of 5-10 nm (see Fig. 17 and Ref.[80]). This results in different unstrained phonon frequencies for differently QD sizes, which has to be taken into account in strain analysis by comparison to a suitable reference sample.

When a shell is added to the QD, the Raman spectrum becomes more complex and reflects the two materials as well as the interaction between them. Hence, Raman spectroscopy is widely used as a sensitive characterization technique to study semiconductor materials like these structures. Since a precise knowledge on the structural properties and the interplay between core and shell is mandatory, because of the direct influence on the optical properties which are responsible for the effectiveness of the QDs in applications, Raman spectroscopy is therefore an interesting tool for the analysis.

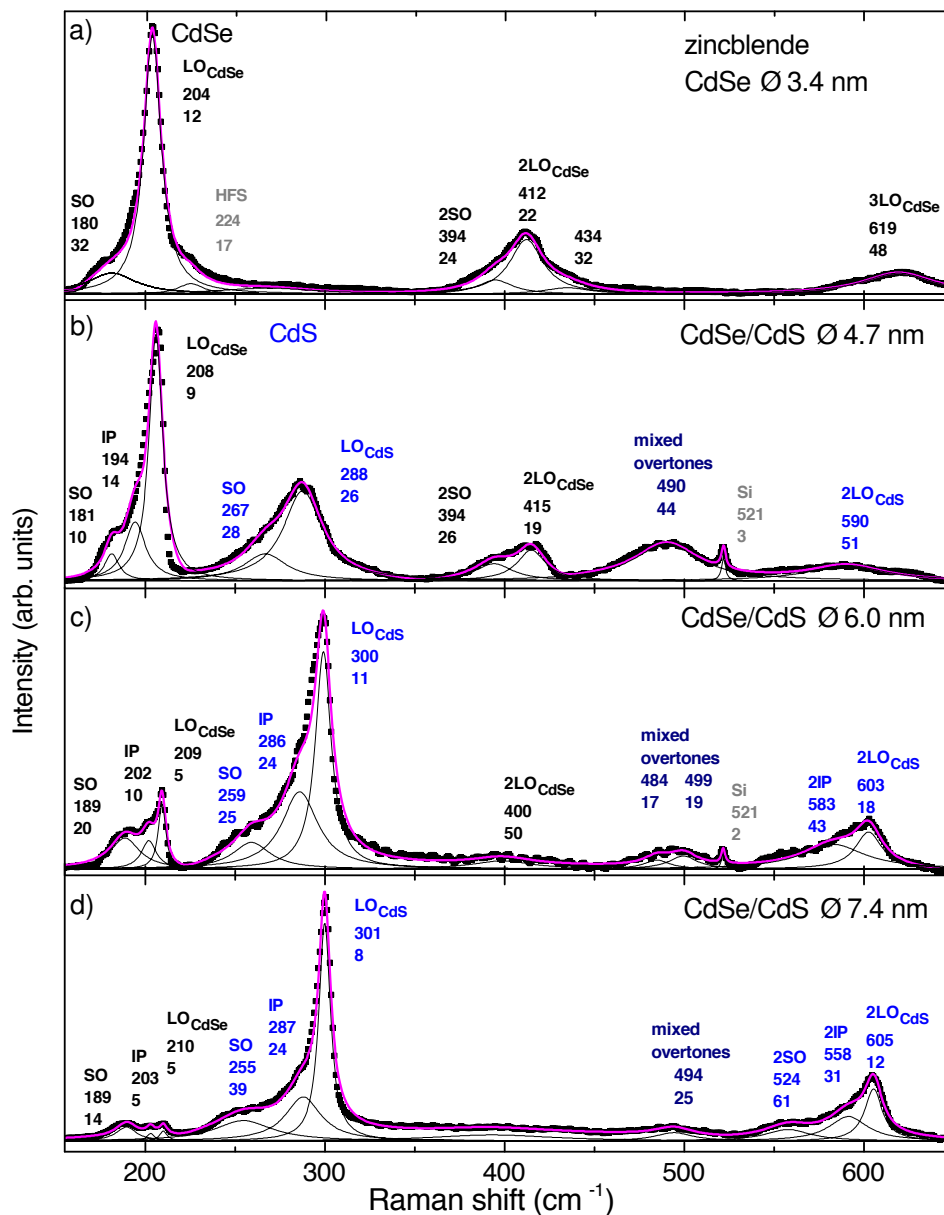


Figure 18: Raman spectra for one wurtzite and one zincblende CdSe QD with a diameter of 3.4 nm, that is covered by a differently thick CdS shell. As the shell thickness increases, the intensity of the CdS increases, the CdSe decreases, the position of CdS shifts to higher energies

The typical spectra of zincblende CdSe/CdS core shell QDs (shown Fig.18) are dominated by the Raman signals of both separate materials, CdSe at around 210 cm^{-1} and CdS around 302 cm^{-1} . The room temperature bulk phonon frequencies are usually given as $\omega_{\text{CdSe, bulk}}=210\text{ cm}^{-1}$ and

$\omega_{\text{CdS, bulk}}=302 \text{ cm}^{-1}$ [90].

Within the shell thickness series in Fig.18, the intensity of those two modes varies strongly. The higher the CdS shell thickness the more intense the CdS phonon mode becomes in comparison to the CdSe phonon mode, because the CdS volume increases and there is simply more CdS material contributes to the Raman scattering. Additionally, depending on the wavelength of the measurement, the light can be absorbed by the CdS shell and hence not reach the CdSe core und such reduces Raman scattering in the CdSe core. Of course this effects incoming and outgoing light and leads to a further reduction in intensity of the CdSe core for increasing CdS shell thickness. The effect, however, is strongly dependent on the wavelength used for the Raman measurement and the absorption characteristics of the CdS shell, which vary according to the shell thickness particularly for thin shells due to confinement. This makes an interpretation of absolute and relative intensities within such a series complex and emphasizes the necessity for a careful analysis when such questions are addressed.

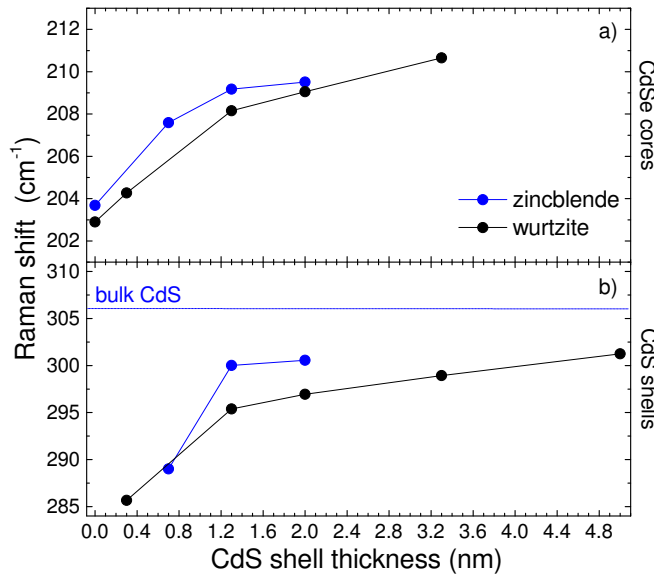


Figure 19: Raman frequencies for the shell thickness series from Fig.18 for the CdSe and CdS modes in dependence of the CdS shell thickness. (wurtzite and zincblende CdSe QD with 3.4 nm diameter)

More straight forward observations can be made by analyzing the positions and occurrence of the various modes in the spectrum. Investigating the positions of the high intensity phonons within the shell thickness series (Fig. 19), we find that the thicker the CdS shell on the QD, the closer the CdS Raman mode shifts towards the unstrained bulk frequency of CdS at around 303 cm^{-1} (at room temperature, 306 cm^{-1} at 7K), which is visualized shown the phonon frequency dependence on the shell thickness in Fig. 19. This shows that the CdS shell that previously showed tensile strain, relaxes the thicker it becomes.

For the CdSe core however, the behavior is the opposite (Fig. 19, with frequencies determined from Fig. 18). The thicker the CdS shell becomes, the further away the CdSe phonon mode shifts in comparison with the uncovered QD. This means the core in contrast to the shell becomes more and more compressively strained and is reflected in the Raman spectrum as a shift of the phonon mode toward higher frequencies. This trend is very similar for wurtzite and zincblende QDs, as shown in Fig. 19. Using Eq. 9 in the previous Section, the strain can be calculated for each material in dependence of the shell thickness, as shown in Fig. 20. The figure clearly shows the increasing and decreasing strain for growing shell thickness, for the CdSe core and CdS shell respectively.

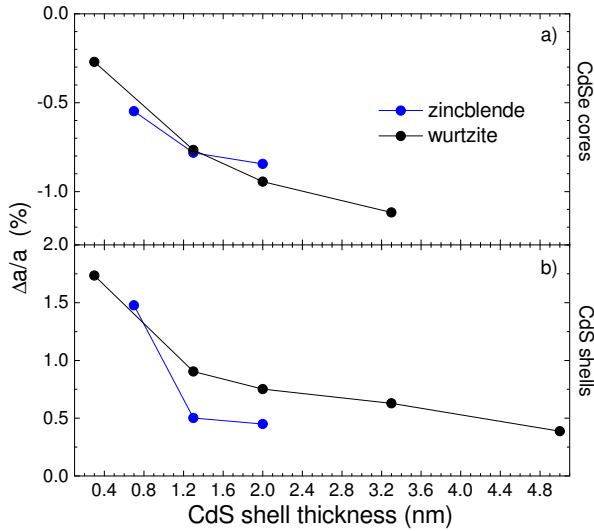


Figure 20: Strain $\frac{\Delta a}{a}$ for the shell thickness series from Fig.18 for the CdSe and CdS modes in dependence of the CdS shell thickness determined with frequencies in Fig. 19. (wurtzite and zincblende CdSe QD with 3.4 nm diameter)

For some core-shell QDs, the core is not visible in the Raman spectra for some excitation energies, due to the before mentioned absorption of the light in the shell. In those cases, the information depth of the measurement becomes smaller than the shell thickness and no information on the core can be gained.

Additionally to the CdSe and CdS phonon mode in first order Raman scattering, each mode has overtones visible in the spectrum, which can be found at approximately the doubled frequency of the first order phonon. They originate from higher order Raman processes and their intensities are often used to determine the exciton-phonon coupling strength, as described in Sec. 5.3. Also mixed overtones, combinations of two or more different phonon modes, are present in the spectrum. These modes are allowed un-

der energy and momentum conservation and can stem from anywhere in the Brillouin zone. This means depending on the materials phononic dispersion, the assignment can be difficult as the frequencies can vary strongly over the Brillouin zone. For the CdSe and CdS overtones however, the second order Raman frequencies correspond to approximately Γ -point frequencies.

In addition to the phonon modes of each material and overtones, more complex phonons can be found taking a closer look at the lower intensity regions and the line shapes of the high intensity modes. Around 180-190 cm^{-1} for instance, a peak to the lower frequency side of the CdSe LO is visible. The mode has been first shown to exist in Raman experiments in 1974 for CdS micro crystallites[91]. It was predicted occur as it is part of the solution of Maxwell's equation, when a damping at the surface of the structure is taken into account, and is named "surface optical" (SO) phonon after it's supposed origin.

Since then, many groups have observed this mode and investigations have been published regarding dependence of this mode on the form of the QD and the dielectric environment. These factors both influence the damping at the QD's surface on the phonons and hence change the solution of the Maxwell's equation. For spherical QDs the size dependence has been investigated by modeling [87] [92] and experimentally by Raman spectroscopy [93]. While calculations regularly find different phonon branches for this phonon, in experiments usually only one mode is observed. But they coherently find a larger separation of SO and LO mode, the higher the surface area becomes. For elongated structures, such as rods or nanowires this geometry dependence has been shown by many groups and for a number of materials, such as GaP[94], ZnS nanowires[95] and CdS nanorods [96] for instance.

Often the influence of the dielectric environment is automatically discussed in the publications, as it is substantial for the calculation of the SO. In this context, the construction of core-shell structures merely presents itself as a special environment with a dielectric constant different from the usually assumed solvent or vacuum. This can be found in Ref. [97] and experimentally for ZnS capped CdSe QDs.[98] For an increasing ZnS shell, the SO phonon near the CdSe LO shifts towards lower frequencies (higher separation from the LO), which shows the growing influence of the ZnS with a lower dielectric constant than the previous environment. Guigni *et al.* even show a dependence of the arrangement for CdSe/CdS nano rods samples.[99]

Recently Lin *et al.*[100] have claimed that the intensity of the feature is strongly dependent on the resonance conditions of the measurement. They say that the peak becomes intense when higher energetic transitions, like $1P_e-1P_{3/2}$, come into resonance. However, their calculation does not explain the geometry dependent energetic shifts, which were observed in earlier publications. Additionally they calculate the localization of the phonons and find that the modes in this energetic region are not localized at the surface, but include atoms in the whole QD. This however is in strong contrast

to atomistic calculations that were performed in this group by Steffem Westerkamp (as yet unpublished), where we find that in this region the vibrations exhibit the highest amplitude in the volume near the surface of the QD.

For sufficiently narrow LO modes (here at the CdSe mode) an additional mode becomes distinguishable, between the LO and the SO signal. This mode has been shown to increase in intensity, when the shell thickness is increased and is correlated with the formation of an interface between the core and the shell of the QD [101] (see also Sec. 4.2, 7.2) Hence this mode is called interface mode (IF in the spectra).

Furthermore additional broader features are observed frequently. In several others publications for instance, Dzhagan calls a broader feature the high frequency shoulder (HFS) of the LO mode of CdSe. However this feature is present in most studies, but has not been assigned to an origin yet. Besides this, there have been reports of a broad feature at about 250 cm^{-1} , which is correlated with the signal of amorphous Se structures[102], resonant with the excitation wavelength of 633 nm.[103] This is however not visible in our samples and should generally be avoidable by purification of the QD solution after the synthesis, as described in Sec. 7.1.

Possibly Raman modes originating from the substrate can become visible in Raman measurements of QD films. In this work, Si substrates are used, which is visible in some spectra with a sharp Raman peak at 521 cm^{-1} . With an intensity that is lower by more than an order of magnitude than the peak at 521 cm^{-1} , the much broader feature around 300 cm^{-1} (characteristic three peak structure), is not visible in any spectra presented here.

Based on this knowledge, in the following Section, the temperature dependence of the Raman signal will be analyzed and discussed for core-shell QDs with different geometries and crystal structures. The observation of the temperature dependent phonon modes will be used to extract temperature expansion coefficients for each material in the QD, proposing a method to separate the pure temperature dependence from the interplay of core and shell.

9 Temperature dependent lattice contraction in wurtzite and zincblende core-shell QDs

This chapter will focus on the influence of temperature on the crystal lattice of the QD, leading to the determination of lattice expansion coefficients. For core-shell structures, extracting the expansion coefficient is complicated by the interplay between core and shell, especially when expansion coefficients differ between the two materials. This difference in thermal expansion causes one material to expand/contract at a different temperature than the other, and thus change the strain it applies to the other material.

This temperature dependent interplay will be analyzed by Raman spectroscopy using a set of core-shell QDs consisting of two shell thickness series with zincblende crystal structure with two different core sizes and one wurtzite series with the same core size as one of the zincblende series to enable a direct comparison of the two crystal structures. Table 1 shows the crystal structure, core sizes and shell thicknesses for the samples used. For zincblende QDs, the CdS shell is grown with the SILAR method, which automatically provides information the shell thickness with monolayer precision (see. Sec. 7.2). For wurtzite QDs, the FLASH method is used for the shell growth and shell thicknesses are determined with TEM. Here the mentioned number of monolayers are estimated from the shell thicknesses.

9.1 Temperature dependence of Raman modes in wurtzite and zincblende core-shell NC

Generally, when a solid body is exposed to changes of temperature, it expands or contracts because the bond lengths defining the lateral dimension of the crystal lattice change. For most solids, above a certain temperature, increasing temperature leads to higher bond length and thus expansion of the material. For temperatures near 0K however, the transport of heat is governed by transversal acoustic phonons, which due to their vibrational geometry effectively reduce the projection of the bond length. Hence for low temperatures, the thermal expansion coefficient can become negative. For CdSe this should be observable around 50K [104], and since our measurements start from 70K should not be observed here.

The thermal expansion above this certain temperature can be easily understood considering the pair-potentials for a bond between two atoms, which is given in Fig.14 for bond between Cd and Se and a bond between Cd and S, as those two bond define the QDs studied in this work. A temperature increase also means an increase in potential energy, via an increase in thermal energy, for the involved species which allows larger distances between the atoms. How much this distance and therewith the lattice parameter changes, in dependence of the temperature, is directly dependent on the

structure (wz/zb)	core diameter (nm)	total diameter (nm)	shell thickness (nm)	shell (ML)
wz	3.4	-	-	
wz	3.4	4.4	0.5	2
wz	3.4	5.9	1.25	4
wz	3.4	7.8	2.2	7
wz	3.4	9.9	3.35	10
wz	3.4	13.3	4.95	15
zb	3.4	-	-	
zb	3.4	5.3	1	2
zb	3.4	6.0	1.3	4
zb	3.4	7.3	1.95	6
zb	4	-	-	
zb	4	5.1	0.55	2
zb	4	5.6	0.8	3
zb	4	6.8	1.4	5

Table 1: List of CdSe/CdS core-shell QDs with wurtzite and zincblende crystal structure used for analysis of the influences if the CdS shell thickness on the phonon modes (Sec. 8.2), thermal expansion properties (Sec. 9) and on the band edge states (Sec. 11, thin shells only). For all wurtzite QDs, the shell thickness in monolayer is approximated, as opposed to zincblende, where it is determined by the number of synthesis steps. (Sec. 7.2)

bonding potential between its components. Hence the thermal expansion is material specific property. This property is mostly described with the linear thermal expansion coefficient, which corresponds to the derivative of the relative change in bond lengths in dependence of temperature.

Taking closer look at the pair potentials in Fig.14, the difference in depth and slope between CdSe and CdS suggest different dependencies on temperature for the materials. Since we are discussing not bulk material, but nanometer-sized heterostructures, where there is an interaction between the different materials of the core and the shell of the QD, the expansion will differ from ideal bulk crystals. The interaction between core and shell induces strain, and since the lattices show different temperature dependencies, this strain is dependent on the temperature. This underlines the necessity to compare temperatures, when comparing strain results from different measurements or even theory. Furthermore it shows that a detailed knowledge on the thermal expansion as well as the temperature dependent interaction between the materials is required.

For bulk materials, this thermal expansion can be determined simply by measuring the change in spatial dimension of a defined sample for different temperatures. However, for nanostructures, this is much harder because

with a size being below optical resolution, the size can only be determined by electron scattering. Furthermore, the separation between change of core and shell size would be difficult as the contrast between the materials is small and hard to determine. Using the total size of the structure determined by TEM, doesn't reveal the effect of the temperature on each material, which defeats the purpose of this investigation of heterostructures. Additionally this method would only work for low temperatures. Another method to determine the coefficient is the determination of the bond length with XRD at different temperatures. [105, 106]

Here we propose the use of Raman spectroscopy, which enables to observe both materials at the same time, as each material has a distinct phonon frequency. The phonon frequency reflects the temperature dependence of bond length, bond strength and strain / geometry of the atoms in a crystal. Generally, in a solid the atoms vibrate round their equilibrium positions in the asymmetric lattice potential (for comparison see pair-potential Fig.14). When the temperature increases, the potential energy of the lattice is increased, which leads to increased interatomic distances and hence expansion, depending on the form of the potential. This increase on bond length directly influences the frequency of a lattice phonon and results in a decrease in frequency (red shift), which can be observed by Raman spectroscopy. Additionally, due to the increase in bond length the collective vibrations can oscillate with a higher amplitude. [107]

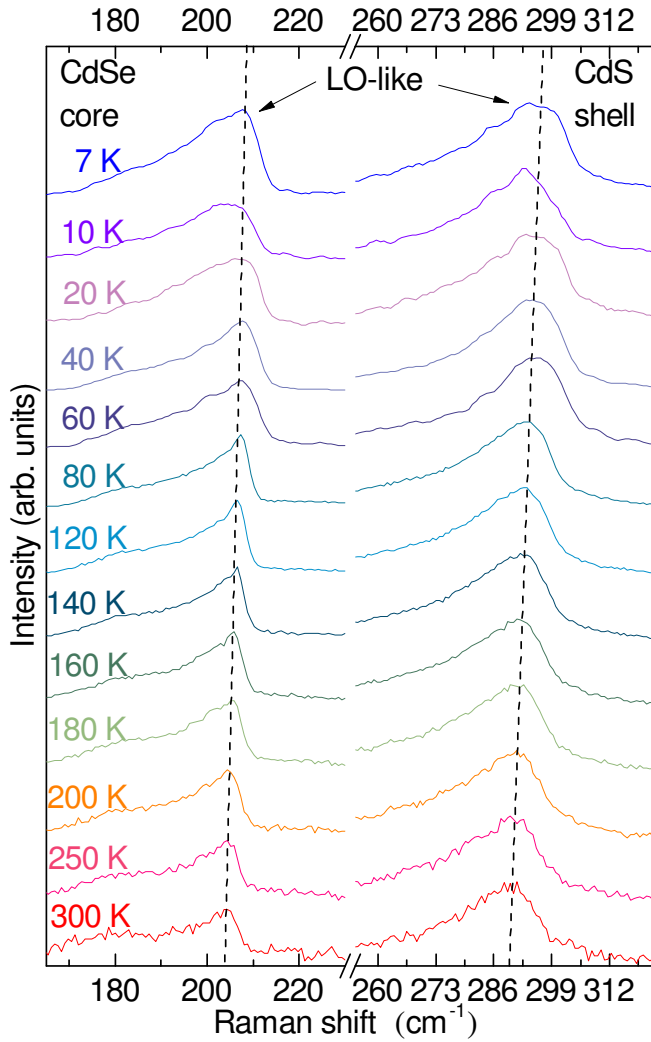


Figure 21: Temperature dependent Raman spectrum of wurtzite CdSe/CdS QD with 3.4 nm CdSe and diameter of 4 nm from 83 K to 298 K. Left: frequency range of the CdSe core. Right: frequency range of the CdS shell. CdSe and CdS LOs showing a characteristic redshift with increasing temperature, visualized by the dashed lines. (CdSe frequency decreases from 210.7 cm^{-1} to 207.0 cm^{-1})

However, independent of the method used for the determination of the bond lengths in the QD, the measured bond lengths are the result of the combined effects of temperature and of the interaction between core and shell. Therefore a suitable description of the expansion and the interplay of the lattices is required. In order to achieve this, we analyze the temperature dependent shifts in Raman frequency (which include temperature and strain effects) for different core-shell QDs including the pure, uncovered core and find a suitable fit function. Then we propose a linear model for the separation of the strain related frequency shift and the temperature dependent properties of the pure materials, assuming negligible interaction between the effects.

Fig. 21 shows typical Raman spectra for a wurtzite CdSe/CdS QD (with a core size 3.4 nm CdSe core and total diameter of 4 nm) in the temperature

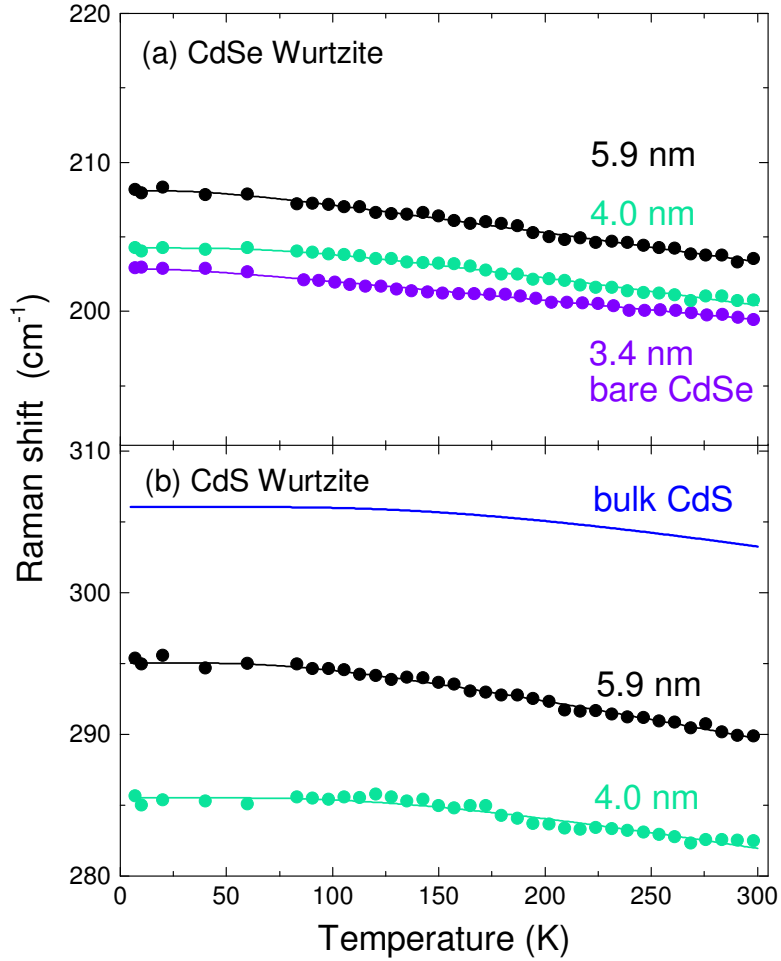


Figure 22: Raman shift as a function of QD diameter and temperature for Wurtzite CdSe/CdS. The samples have the same sizes of CdSe cores 3.4 nm and several different thicknesses of CdS shells. With increasing shell thickness (QD diameter is increasing from 4 to 5.9 nm) the Raman values are significantly shifted in frequency, relative to bare CdSe core ((a), blueshift), bulk CdS shell ((b), redshift) and between the samples. Additionally, the CdSe core and CdS shell LOs showing a characteristic redshift with increase of temperature. Their temperature-dependency were describe well by the calculated curves (solide lines) using equation 16. (bulk CdS blue solid line taken from Neto et al. [104]).

range between 7 K and 298 K. In agreement with a general lattice expansion as described above, we find a redshift in phonon frequency for both materials. The temperature dependent frequencies of the CdSe and CdS phonon are displayed in Fig. 22 for a series of different shell thicknesses on the same wurtzite QD core (3.4 nm, the same as in Fig. 21). For reference, the temperature dependence of the pure, uncovered CdSe core and bulk CdS are included in the Fig. The frequency shift for all phonon modes is fitted with an empirical formula proposed by Cui et al. [108], which describes the data well and will be used for the following calculations to have continuous data. For the fitting procedure A, B and ω_0 at 7 Kelvin where used as free fit-parameters, resulting in the displayed functions.

$$\omega(T) = \omega_0 - \frac{A}{e^{B\hbar\omega_0/k_B T} - 1} . \quad (16)$$

Equation after Cui et al.[108]

Additionally to the generally decrease in frequency with increasing temperature, Fig. 22 visualizes the differences within the shell thickness series, which are induced by strain in the core-shell structure. With increasing shell thickness, the CdSe LO modes shift to higher frequencies (blueshift) compared to bare CdSe core. For the CdS LO mode, the trend is opposite: For increasing shell thicknesses, the phonon frequency of the CdS LO shifts towards lower energies (redshift) compared to bulk CdS.

The strain of those materials, which is defined as the relative contortion of the lattice constant ($\frac{\Delta a}{a_0}$), can now be calculated from the relative shift of the phonon frequencies compared to an unstrained value using the formula (Equation 9) introduced in Section 5.2, with $\gamma_{\text{CdSe}} = 1.1$ [46] and $\gamma_{\text{CdS}} = 1.37$ [47] the Grüneisen parameters for wurtzite CdSe and CdS. Considering the strain resulting from our Raman measurements, we see that for increasing CdS shell thickness, the tensile strain of the CdS shell relaxes, while the compressive strain of the CdSe core is increases, as shown in Fig.22. These results are in good agreement with other studies by Tschirner et al. [43] and Dzhagan et al. [109] for instance. Additionally it become apparent, that the strain is different at different temperatures.

Based on these findings, in the following Sections the separation between pure temperature-related effects and strain effects due to the interplay between core and shell will be addressed.

9.2 Separation method of thermal and epitaxial strain effects

For the separation of epitaxial and temperature induced strain effects, we first address the calculation of strain and insert equation 16 into equation 9, to gain a formula which allows for a direct calculation of the strain from the

relative change in phonon frequency. This results in equation 17:

$$\frac{\Delta a(T)}{a} = \frac{1}{3} \left[\left(1 + \frac{\Delta \omega(T)}{\omega} \right)^{-\frac{1}{\gamma}} - 1 \right] \quad (17)$$

Within this formula, the change in Raman frequency can be defined in several different ways. On the one hand, the shift in frequency can be determined relative to the frequency at the lowest possible temperature (here 7K). This gives the effectively measured phonon frequency shift, that hence will be called $\left. \frac{\Delta \omega(T)}{\omega} \right|_{\text{eff}}$, and is defined as shown in equation 18. The strain calculated from this frequency shift includes influences from temperature and epitaxial strain related effects and will be called $\left. \frac{\Delta a(T)}{a} \right|_{\text{eff}}$ analogue to the frequency.

$$\left. \frac{\Delta \omega(T)}{\omega} \right|_{\text{eff}} = \frac{\omega(T)_s - \omega(T = 7K)_s}{\omega(T = 7K)_s} . \quad (18)$$

Where $\omega(T)_s$ is the temperature-dependent phonon frequency of the corresponding sample (index s).

On the other hand, the strain component of the effectively measured temperature dependent strain, is caused by the interaction between core and shell (epitaxial strain, index strain), is of high interest. This component can be determined by calculating the strain of the sample in comparison with an unstrained reference sample for each temperature (Eq. 19).

$$\left. \frac{\Delta \omega}{\omega}(T) \right|_{\text{strain}} = \frac{\omega(T)_i - \omega(T)_{\text{ref}}}{\omega(T)_{\text{ref}}} \quad (19)$$

Where $\omega(T)_{\text{ref}}$ is the temperature-dependent function of the phonon frequency of an unstrained reference sample (index ref). For the CdSe cores, we use the bare core as unstrained reference, for the CdS shell the reference is provided by bulk CdS, because a shell without a core cannot be synthesized. The bulk CdS reference is taken from data published by Neto et al. [104] and fitted with equation 9. Those references are then compared to $\omega(T)_s$, the temperature-dependent function of the phonon frequency of the analyzed sample.

These distinct strain functions for both materials, CdSe core and CdS shell are shown in Fig. 23 for one exemplary QD of the series in Fig. 22 (details in the caption). Generally, due to smaller lattice parameters of the CdS crystal structure in respect to CdSe, we find the CdSe core to be compressively strained (CdSe_{compressive}, negative $\frac{\Delta a}{a}$), while the CdS shell exhibits tensile strain (CdS_{tensile}, positive $\frac{\Delta a}{a}$). The amount of strain is higher for the core indicating a higher influence of the shell inside the heterostructure.

The temperature dependence of the epitaxial strain (index strain) of the CdSe core reveals decreasing strain for increasing temperature, which is opposed by the effect the increasing temperature has on the CdS shell, where

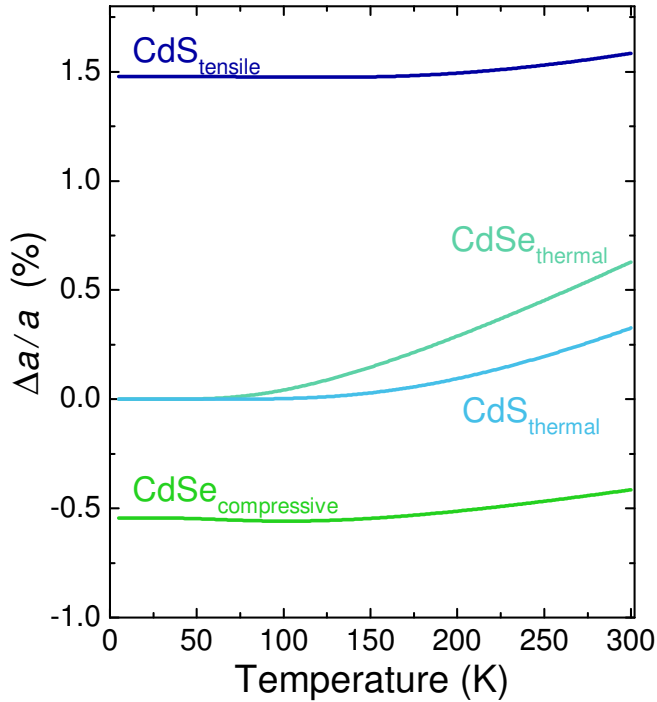


Figure 23: Strain $\frac{\Delta a}{a}$ as a function of temperature and shell thickness for one QD for the shell thickness series shown above. The compressive strain of the core (CdSe_{compressive}) increases as the temperature decreases, while the tensile strain of the shell (CdS_{tensile}) decreases. Due to different thermal expansion between CdSe and CdS, they show temperature-dependent strain.

the tensile strain increases. This shows that higher temperatures favor the relaxation of the CdSe core due to its temperature expansion properties, and underlines the necessity to think about temperature dependence when comparing results on strain gained by different groups and methods. For instance, results gained from room temperature Raman measurements cannot directly be used to explain shifts in low temperature PL.

The effectively observed thermal strain $\left. \frac{\Delta a(T)}{a} \right|_{\text{eff}}$ for CdSe and CdS is negligible (≈ 0) between 7K and 75K, where the temperature apparently has little effect on the lattice parameters only. But above 75K (onset depends a little on the sample), we find an increase in lattice parameter for both materials, which is in fact stronger for CdSe. Both increases in effectively measured $\left. \frac{\Delta a(T)}{a} \right|_{\text{eff}}$ are steeper and higher than the change observed for the pure epitaxial strain. So it becomes apparent, that the effectively observed temperature dependence of the lattice is largely influenced by temperature expansion and epitaxial strain. The different behavior in temperature dependent change of the lattice will lead to different expansion coefficients of the two materials, as will be discussed in the next Section.

9.3 Linear temperature coefficients for heterostructures

For the analysis of the pure thermal expansion and hence the separation of thermal and strain effects in heterostructures in general, and CdSe/CdS

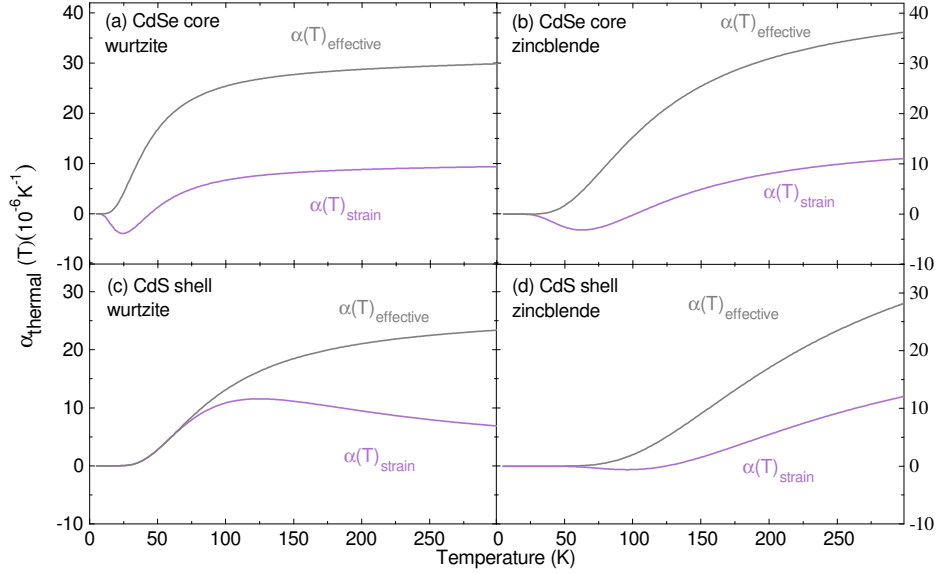


Figure 24: Shows a comparison of the coupled effects of the thermal expansion coefficient $\alpha(T)$ as a function of the temperature exemplary for two Wurtzite and zincblende QDs. $\alpha(T)_{\text{effective}}$ originates effective from different thermal expansion and $\alpha(T)_{\text{strain}}$ from lattice mismatch.

QDs in particular, we first introduce a definition of the linear temperature coefficient in order to then propose a method to separate thermal and strain effects in heterostructures.

The linear thermal expansion coefficient (LTEC, $\alpha(T)$) of a material is defined as the change in length per unit (usually nm) with the change in temperature per K. The magnitude of the LTEC depends on the structure, symmetry and bonding potential of the material. To determine this coefficient from our experimentally measured data, we use a temperature-dependent function (Eq. 20), based on the formula published by James et al. [106] and Okada and Tokumaru [110], which essentially is the differentiation of the strain with respect to the temperature. Hence, as a more visual description, the LTEC can be obtained from the slopes of the strain function (see Section 5.2) at any temperature:

$$\alpha(T) = \frac{d}{dT} \left(\frac{\Delta a(T)}{a} \right) \quad (20)$$

Applying this formula for the LTEC to our results from previous sections, we find two different coefficients: One originates from the lattice mismatch between CdSe and CdS (shell thickness) - the epitaxial strain, $\alpha(T)_{\text{strain}}$, and another one that is the effectively observed thermal dependency of the lattice $\alpha(T)_{\text{effective}}$, which includes strain effects.

Fig. 24 shows the calculated results of this two effects as a function of the temperature, $\alpha(T)_{\text{strain}}$ and $\alpha(T)_{\text{effective}}$, exemplarily for one wurtzite and one zincblende QD for CdSe and CdS. While there are strong differences for the wurtzite and zincblende cores, the CdS shells only differ marginally. The function $\alpha(T)_{\text{effective}}$ for the zincblende core (Fig. 24 b) shows a steeper increase with temperature increase and overall higher values for the LTEC compared to the wurtzite core (Fig. 24 a). In the low-temperature region, we find an additional difference, $\alpha(T)_{\text{effective}}$ for zincblende core remains constant for higher temperatures, up to 35 K, than for the Wurtzite core. Overall, the $\alpha(T)_{\text{strain}}$ of the cores with different crystal structures are distinct and differ strongly especially for low temperatures, whereas it is almost the identical for the different shells over the whole temperature range (trend, values), see Fig. 24 c,d.

$$\alpha(T)|_{\text{thermal}} = \alpha(T)_{\text{effective}} - \alpha(T)_{\text{strain}} \quad (21)$$

However, in order to obtain the pure thermal expansion coefficient $\alpha(T)|_{\text{thermal}}$, these effects need to be separated. As an approximation, we calculate the difference between the two functions, separating the thermal strain from epitaxial strain (equation 21). This assumes that the two effects can be separated linearly and do not have any higher order interaction.

Applying this method, we find thermal expansion coefficients for CdSe and CdS, shown in Fig. 25 for all samples (see Table 1). Within one series, the LTECs of the CdSe core and CdS shell converge independent of the shell thickness of the corresponding sample. This underlines that the linear interpolation approximation, we made for the separation of the different influences on the lattice constant, is reasonable and sufficiently removes the effect of the epitaxial strain from the pure thermal properties of the material. All calculated LTECs (Fig. 25) increase with increasing temperature, which merely reflects that the material expands for increasing temperature, as expected.[107]

For all CdS shells, the resulting LTECs coincide, which reflects the fact we only found small differences in their temperature dependent behavior, already in the Raman spectra. The coinciding temperature expansion coefficients manifest in the parallel shift of the temperature dependent Raman frequency of all CdS shell Raman modes. As the LTEC can be viewed as the derivative of the lattice constant in dependence of the temperature, and since the lattice constant is described with $\frac{\Delta a(T)}{a} \propto \frac{\Delta \omega}{\omega}(T)^{-\frac{1}{\gamma}}$, with $\gamma \approx 1$ (CdS, CdSe), it is a good approximation to use parallel shifts of the phonon frequency in dependence of temperature as an indication for similar LTEC.

A direct comparison between the thermal expansion coefficients of the CdSe cores and the CdS shells (Fig. 25), provides smaller overall expansion for the shells, which can be explained using the inter-atomic pair potentials (Fig. 26) for the two materials. The potential curve of CdS has a deeper

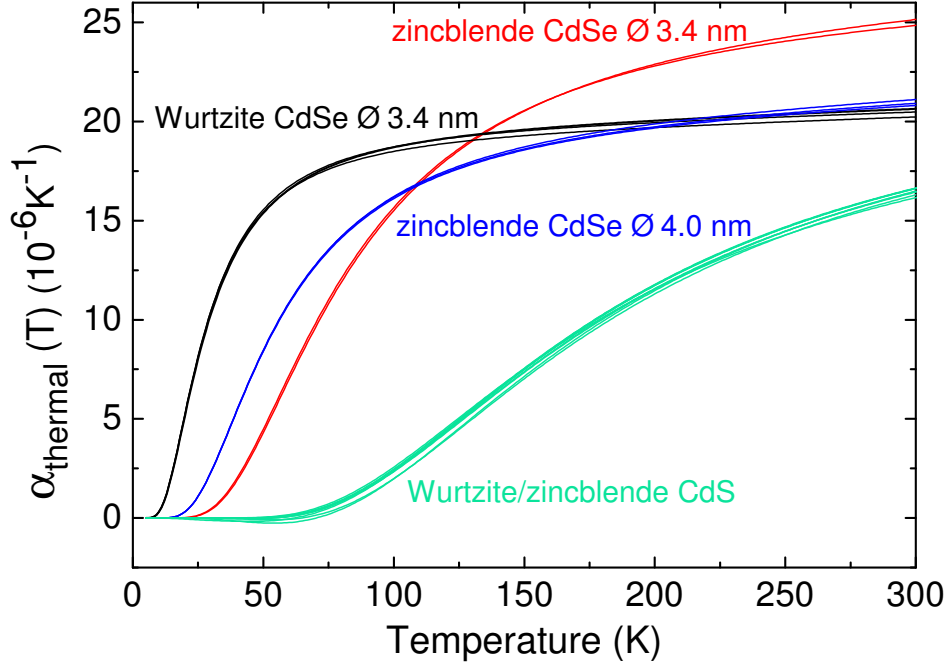


Figure 25: Thermal expansion coefficient $\alpha_{\text{thermal}}(T)$ as a function of temperature for wurtzite and zincblende CdSe/CdS QDs as determined with Eq. 21 from the measured temperature dependent Raman spectra.

and steeper (smaller width) minimum at lower distances compared to CdSe, which indicates a stronger bond between Cd and S, than between Cd and Se. Generally, materials with strong bonds typically have a lower thermal expansion coefficient [107] than materials with weaker bond and flatter potential, expectation in congruent with our findings. This can be understood by comparing how much thermal energy needed to increase the equilibrium distances between the atoms within the potential. This leads to the conclusion that for steeper potential minima, the same additional amount of thermal energy, increases the equilibrium position of the atoms and therefore with the lattice constant less than for a flatter minimum. This matches our results of smaller temperature expansion for CdS compared to CdSe well. Additionally to the different materials, we have analyzed different crystal phases, and find a steeper and higher increase for the zincblende phases compared to the wurtzite phase, looking at the CdSe cores with 3.4 nm diameter with different crystal structures (Fig. 25). This demonstrates the different temperature dependent behavior of the two phases, which can be understood, when considering the corresponding interatomic distances in the pair-potential (see Fig. 26, marked d_{wz} , d_{zb}). Since the wurtzite phase consists of smaller interatomic distances as the zincblende phase, it's atoms equilibrium positions are closer to the minimum of the interatomic potential,

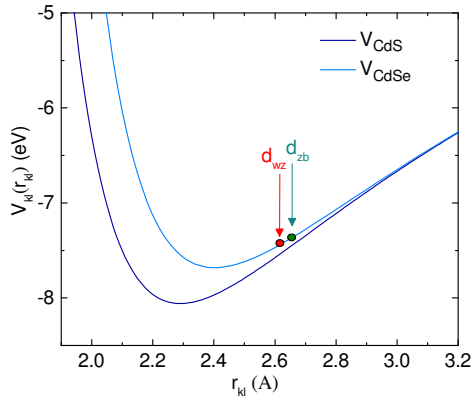


Figure 26: A plot of two-body inter-atomic potential energy for CdSe and CdS as a function of inter-atomic distance. The function of the Lennard-Jones-like inter-atomic potential $V_{ij}(r)$ and the potential parameters were taken from Refs. [79]. The distance between nearest neighbor atoms for the Wurtzite ($d_{wz} = 0.263 \text{ nm}[111]$) and zincblende ($d_{zb} = 0.265 \text{ nm}$, $d_{zb} = 1/4\sqrt{3}a$) CdSe are marked on the potential curve.

which only allows for smaller changes upon increase of thermal energy than for the zincblende phase. The onset of the expansion however, is different for the two phases. For wurtzite, the crystal starts expanding at lower temperatures than for the zincblende structure, which might originate in the crystal structure's anisotropy. Trallero-Giner *et al.* have confirmed that the lattice vibration observed in Raman spectroscopy is a vibration along the c-axis by comparison of temperature dependent Raman measurement and *ab initio* lattice dynamical calculation.[80] This vibration in c-direction has a stronger temperature dependence than a vibration in a-direction would have. The atomic distances along the c-axis in the crystal are larger than for the a-direction, which could explain an onset of expansion at lower temperatures for this direction, as in the interatomic potential (Fig. 26) becomes less steep for higher distances, allowing larger changes in atomic distance per added thermal energy. But the onset of thermal expansion also depends on the size of the core, comparing 3.4 nm and 4 nm zincblende core in Fig. 25.

Moreover, different CdSe core sizes with the same crystal structure, show differently high total thermal expansion (Fig. 25). This, together with the different onset of expansion, indicates a size dependence of this property, as found for so many other attributes for particles in this size range, as the frequency of the phonon mode or the lowest optical transition for instance (see Sec.4, 7)

In conclusion, through the analysis of temperature dependent Raman measurements of colloidal CdSe/CdS core-shell QD of different crystal structures, we show that the epitaxial strain-related temperature effects can be separated from the temperature dependence of the pure materials by comparison with the temperature dependence of an unstrained reference material. Thus we demonstrate that with this approach it is possible to retrieve the temperature expansion coefficients of the pure materials from interca-

lated heterostructures.

Analyzing the resulting thermal expansion coefficients, we find different coefficients for differently sized QDs, which points towards a yet another size dependent effect in the low nm-regime. Furthermore we find a generally higher temperature dependence for the zincblende crystal phase compared to the wurtzite phases, which can be explained by their different interatomic distances in the pair-potential. This confirms that the crystal structure plays an important role for the temperature expansion coefficient, and thus must always be considered. Additionally, material specific different coefficients are found for CdSe and CdS. Here, CdS shows lower LTECs and thus temperature dependent expansion than CdSe, which is in agreement with the differences in the respective inter-atomic pair-potentials.

10 Exciton-phonon coupling

The magnitude of the coupling of excited charge carriers to phonons contributes to the time scales of different photophysical processes[112] of high significance for various light emitting applications. Although there are several studies on the coupling strength in colloidal II-VI semiconductor QDs, experimentally as well as theoretically, no consensus is found on the order of magnitude of the Huang-Rhys factor S . Furthermore, the dependence of the coupling strength on the QD size is much debated with diverging results.[113]

While some groups report a size-independent exciton-phonon coupling[55], other groups find a decreasing[114, 115] or increasing[83, 116, 117] coupling strength for decreasing QD size. Nomura *et al.*[118] report a minimum of coupling strength at a radius of 7 nm for spherical CdSe QDs and an increase for both decreasing and increasing size based on their calculations. According to them the increase in coupling strength for increasing QD size after the minimum is caused by an increase in coulomb interaction, whereas the enhanced coupling toward decreasing QDs size originates from valence band mixing in the strong confinement regime. For PbS quantum dots, on the other hand, Krauss find a maximum in similar calculation, but in measurements they observe S to be 4 orders of magnitude larger than their calculations indicate. Salvador *et al.*[119] find for CdSe a size independent coupling constant in the order of 0.10-0.12 to the optical phonon, but a strong diameter dependence for the coupling to acoustic phonons with a maximum at about 2 nm diameter. They explain this by, on the one hand the increase in phonon energy for decreasing particle size, and on the other hand by the increasing reorganization energy at small sizes, which reduces the coupling. However in this work, we focus on the coupling to optical phonons. Opposing the size independent exciton-phonon coupling, Oshiro *et al.* [120] confirm the existence of a minimum, claiming that the increase at small diameters is due to the difference in polaron effect on electron and hole, while the decrease at larger diameters stems from the large polaron effect on the electron, which decreases with decreasing size. Their calculated minimum is estimated to lie between 1.5 to 2.5 nm radius, depending on the assumed band offset. The Huang-Rhys factor “ S ”, they conclude to be around around 0.6. This minimum is also found by Zheng *et al* [121] for zinc-compound materials, where the minimum position is found to vary dependent on the crystal composition.

Another, more recent, theoretical approach has been taken by A.M. Kelley [122], who combined atomistic calculations (GULP) of the phonons in CdSe NCs with electronic potentials calculated p(article in a sphere) with a deformation potential approach to estimate the coupling strength. Resulting values of the Huang-Rhys factors are between 0.6 and 1.2. They also find an increasing coupling strength for decreasing particle size, for particles smaller

than 2.6 nm diameter, which is the size limit of their atomistic calculation. But they also point out, that the coupling strength in bulk CdSe is higher, which points towards a minimum in somewhere between 2.6 nm diameter and the bulk crystal.

In conclusion, the diameter dependence of the exciton-phonon coupling in spherical CdSe QD remains a subject of research and discussion. Hence, using a series of spherical zincblende CdSe QD with sizes between 3.0 and 6.4 nm, the size dependence of this quantity is analyzed. Furthermore, using a diameter series of spherical wurtzite QD between 3.6 and 5.2 nm are analyzed for comparison of the exciton phonon coupling strength for the two different crystal structure. The effects of the addition of the CdS shell on the exciton phonon coupling will be discussed, based on Raman and FLN measurements.

Amongst the experimental method, Raman spectroscopy is the most commonly applied to evaluate the coupling strength between excitons and the crystal lattice. While many used calculation like presented in Sec. 5.3, some authors use the intensity ratio between first and second order Raman peak directly, or alternatively insert the intensity ratio directly as the displacement parameter (Δ) of the harmonic oscillator in equation (Eq. 15), which leads to $\frac{|I_{1LO}/I_{2LO}|^2}{2}$.

However, Kelley *et al.* present calculations based on a Brownian oscillator model, that suggest a dependence on the experimental conditions, namely the wavelength used in the experiment and the resonance condition therein.[59] Comparing zincblende and wurtzite CdSe QDs in Raman spectroscopy, suggests that the energy difference between the electronic transition and the exciting photon energy generally changes the estimated Huang-Rhys factor S because of resonant enhancement near lowest energy excitonic states[59]. Which is why excitation wavelength dependent Raman measurements are include in the following Section to address this aspect.

However, the conclusion of Kelley *et al.* is not supported by full resonant Raman measurements, as the Raman signal even just coming close to resonance with the ground transition is drowned out by the intense luminescence of the QD. Hence, no measurement in full resonance is presented. Additionally, to achieve Raman spectra with low luminescence back ground, they used hole-accepting ligands to quench the QD's luminescence. However, this surely deforms the hole wavefunction and makes comparability questionable.

Another, more direct method of determination of this coupling strength is posed by close analysis of resonant PL measurements, by comparison of the intensities of phonon replica of the ground transition. However, one must carefully consider the coupling to which state is determined in the measurements, as for low temperatures, the spectrum is actually dominated by phonon replica of the "dark" state, which becomes optically active for temperatures close to 0K (see also Sec. 11).

10.1 QD diameter dependent Huang-Rhys factor from Raman spectroscopy

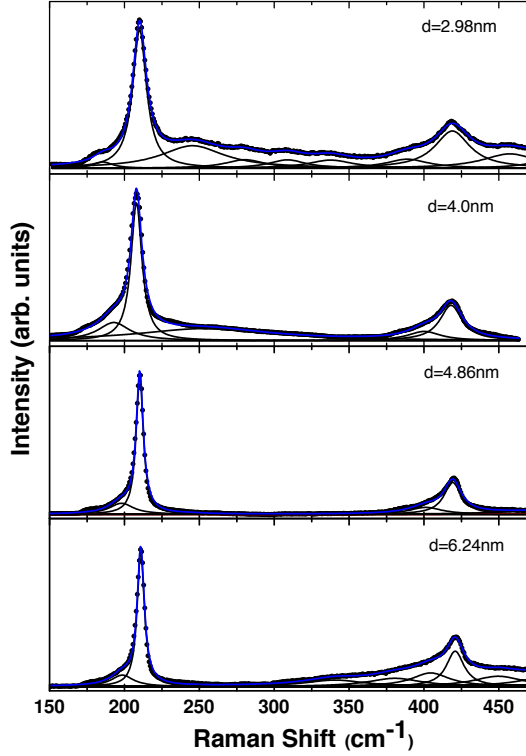


Figure 27: Exemplary Raman spectra for several QD of the zincblende diameter series with the fit used to extract the 1LO and 2LO intensities. The background varies widely over the whole series, becoming more intense for both very small and large sizes. At the same time the second order Raman intensities increases, indicating a higher coupling. However this coupling seems to enhance all observed features, not only the LO mode. The intensities are normalized to the CdSe first order Raman signal. Intensities used for the determination of S are areas under the fitted peaks.

As demonstrated in Sec. 5.3, it is possible to determine the Huang-Rhys factor by comparison of the intensities of different order Raman processes. Here, the intensities of first and second order LO are compared, but a comparison with third or fourth order should lead to equally valid observation. However the observation of third or higher order Raman signal is limited due to low intensity, especially for low coupling strengths. Entering these intensity ratios in Eq. (15), using Eq. (14), the energy of the electronic transition for each QD and $\Gamma = 20 \mu\text{eV}$ for the linewidth, as mean values[123] allows the calculation of the parameter S . Additionally the LO-phonon frequency and the excitation energy, are measured or set by the experimental conditions and inserted into the equation. Additionally, a different measure of the exciton-phonon coupling will be shown used, which also repeatedly appears in literature. Here it is assumed that the intensity ratio approximately equals the displacement parameter Δ , which leads to $S' = \frac{|I_{1LO}/I_{2LO}|^2}{2}$. To investigate the dependency of the electron-phonon coupling strength on the QD size, a series CdSe NCs of different diameters between 3 nm and

6.4 nm were analyzed (same series, as used for analysis of the band edge fine structure in Sec. 11). Fig. 27 shows a selection of Raman spectra differently sized zincblende QDs together with the fits used for the determination of the HR factor. Over the size range, the background changes as well as the half width of the LO mode, which decreases for larger QDs, as should be expected from confinement. Other modes beside the LO become more intense for both very small and large sizes, at the same time as the second order Raman intensities increases. This indicates that a higher coupling seems to enhance all features, not only the LO mode. Atomistic calculation on the phonon frequencies within this kind of structures have shown that the spectra actually consist of a very broad, continuous spectrum, providing all kinds of frequencies apart from the well know bulk-like LO frequencies. However it is suspected that strong selective coupling leads to the well-known spectrum, dominates by one phonon mode only.[100, 122, 124, 125]

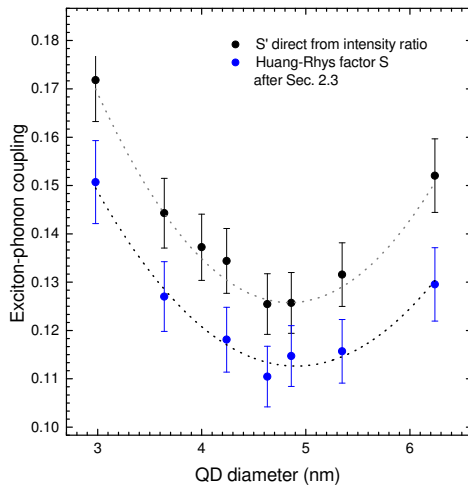
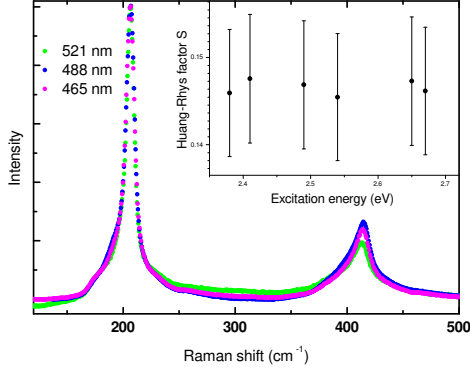


Figure 28: Huang Rhys factor S (after Sec. 5.3) and $S' = \frac{|I_{1LO}/I_{2LO}|^2}{2}$ for the zincblende CdSe QD diameter series in comparison. Both determined from Raman spectra at 10K with a 488 nm excitation. S and S' vary between 0.1 and 0.2, showing a distinct minimum in coupling strength at about 4.7 nm QD diameter. The lines are added as a guide to the eye, the indicated errors merely represent the error of the measurement, fitting errors are not included.

The Huang-Rhys factors S and S' , determined for the zincblende CdSe diameter series are shown in Fig. 28, showing only a small offset between the two values. With coupling factors between 0.1 and 0.2, the observed values are with previously reported S (see above). However, the diameter dependence reveals a distinct shape including a minimum around 4.7 nm and an increasing coupling strength towards increasing as well as decreasing QD size.

As described in the introduction of this section, the resulting HR factors are discussed to be dependent of the wavelength of measurement. To address this issue, the excitation wavelength is varied. Fig. 29 displays the Raman spectra of the 4.6 nm zincblende QD, excited with 465 nm, 488 nm and 514 nm. The measurement at 514 nm is closer to the bandgap and shows a more prominent background. The determined parameter S for several

Figure 29: Raman spectra of 4.6 nm diameter CdSe NCs excited at 465 nm (violet), 488 nm (blue) and 521 nm (green). The spectra were normalized to the fundamental Raman peak. Inset: Determined S for the 4.6 nm diameter zincblende QD, for varied excitation wavelength with errors based on measurement inaccuracy. Within measurement error, S is constant over the observed excitation energy range.



further wavelength for this sample is displayed in the inset and reveals only small changes in the resulting coupling strength, which is extracted from fits to the spectrum. However, with a diameter of 4.6 nm, this sample is near the minimum of the size dependence of S (Fig. 28) and for small coupling strengths, the variation with excitation energy might be small. Still, the measurements indicate, that the minimum remains fix for the investigated excitation energy range.

Hence, Fig. 30 displays S for QDs with different diameters, determined with

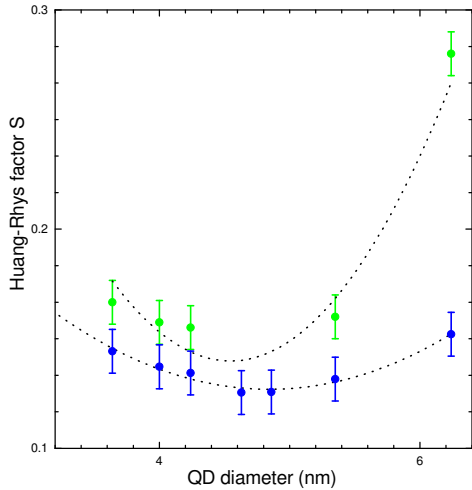


Figure 30: Huang-Rhys factors S , estimated from Raman spectra of zincblende CdSe QDs with different diameters, measured with 488 nm and 514 nm as excitation wavelength. The curves roughly follow the same trends, however the scale differs between the two excitations. S is consistently larger for excitation with 514 nm. The dotted lines are a guide to the eye.

488 nm and 514 nm as excitation wavelength. Starting from the largest diameter, S decreases for decreasing QD size until a minimum value is reached around $d=4.7$ nm, then increases consistently for both wavelength, the values however being larger for 514 nm excitation wavelength. This confirms the existence of a minimum in electron-phonon coupling, independent from measurement energy. But the figure also shows, that the influence of the

excitation wavelength on the observed coupling factor is not sufficiently accounted for in the calculations presented in Sec. 5.3. This indicates that the calculation doesn't provide advantages compared to S' , which shows the same dependency and only marginally larger values, but can be directly determined from measurement. Hence S' can be easier determined and compared.

Figure 31 displayed S' for the wurtzite and the zincblende series in de-

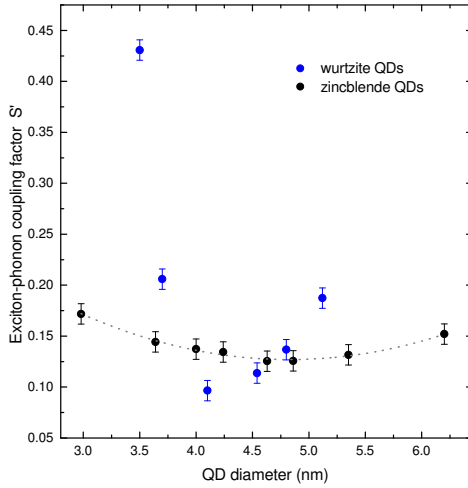


Figure 31: Exciton-phonon coupling factors S' , estimated from Raman spectra of zincblende and wurtzite CdSe QDs with different diameters, at 10K with an excitation wavelength of 488 nm. For the wurtzite QDs, the minimum lies between 3.8 and 4.4 nm diameter, for zincblende QDs at 4.7 nm. Outside of the minimum, the wurtzite QDs show a stronger coupling by a factor of 2-4, size dependently.

pendence of the QD diameter. There are less data points for the wurtzite series, due to generally broader and less defined features of the wurtzite Raman spectrum and hence more difficult evaluation of intensities. However, the coupling strength for wurtzite QD also indicates a minimum just like for zincblende structure, but a smaller sizes between 3.8 and 4.4 nm. The coupling strength outside of the minimum is larger than for the zincblende series, by a factor of 2-4 (size dependently) under the experimental conditions used. This, shows once again the fundamental differences between the crystal structures. The higher polarity of the wurtzite lattice should induce a higher interaction of the lattice with excitons and hence a higher exciton-phonon coupling is expected of the wurtzite structure. Although it should be noted, that this higher coupling could also be an effect similar to the observation on the excitation energy dependence of the coupling strength for zincblende QDs. There the coupling is higher for excitation closer to the ground state. Since the ground state of the wurtzite QDs is at higher energies compared to zincblende (see Sec. 11.2), the excitation energy used is automatically closer to the ground state, which could increase the coupling and lead to an overestimation.

The shape of the curves (Fig. 28 and 30) strongly supports the existence of a minimum as postulated by Normura *et al.* [118], albeit the minimum is predicted for a diameter of 14 nm. However the diameter at which the minimum is observed here for both crystal structures, is closer to the findings of

Oshiro *et al.* [120], who find a minimum in coupling strength around 4-5 nm diameter, depending on the assumed band offset to the environment. Applied to the present case, where the observed minimum in coupling is lower for wurtzite QDs compared to zincblende QDs, this could indicate that the band offset is smaller for the wurtzite QDs[120]. This is possible considering that the QDs are measured in equal environments and but have different ground state energies (Sec. 11.2). Oshiro *et al.* explain the strong increase of the coupling with further decreasing particle size after the minimum, with the difference in polaron effects on the hole and the electron in the strong confinement regime.

Normura *et al.* see the general decrease in coupling with decreasing QD size as a decrease in influence of the Coulomb interaction, whereas the increase following the minimum originates from increasing confinement.[118]

Because of the observed variation of absolute value of S , it is reasonable to leave comparison beyond the order of magnitude aside. The magnitude of coupling strength however is the same for Oshiro *et al.* (0.6 for the lowest value), but compared to Nomura *et al.*[118] is larger by an order of magnitude. However the same order of magnitude has been observed in measurement several times, as can be found in a good overview over previously found orders of magnitude of the Huang-Rhys factor.[126]

10.2 Huang-Rhys factor in CdSe/CdS core-shell QDs

The Huang-Rhys factor has previously been found to decrease once a shell is added to the QD.[43] Figure 32 gives an overview over the Huang-Rhys factors determined for a zincblende series with different shell thicknesses on the same core size of 4 nm. The coupling strength drops dramatically upon shell addition of 2 ML only and further decreases for increasing shell thickness. This seems reasonable, as the addition of a CdS shell effectively reduces the overlap of the hole and electron wave function, as the electron's wave function leaks into the shell.

Since, as described in the previous Section, we found that the strength

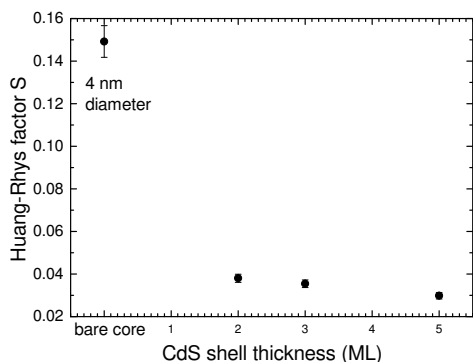


Figure 32: Huang-Rhys factor S determined by Raman spectroscopy at 10K for a series of zincblende CdSe/CdS core-shell QDs with varied shell thickness. The core diameter remains constant at 4 nm and the shell is successively added by SILAR method (Sec. 7.2). S decreases dramatically upon CdS shell addition.

of the coupling observed by Raman spectroscopy depend on the resonance of the QD's transition and the excitation wavelength used for the measurement. Here the excitation wavelength is fixed, while the shell addition shifts the transition toward the red (see Sec.7). Hence, the condition changes continually and it is possible that the reduction of S originates from the shift of the QD's transition further away from resonance. This leads to the idea to measure the coupling in resonance with the main transition of each sample to ensure consistent conditions.

Therefore, with the setup described in Sec. 6.2, PLE measurements were performed on two sets of CdSe/CdS core-shell QD with varied shell thickness (extracts from the series' used in Sec. 8,9 and 11), based on a wurtzite and a zincblende CdSe core with a diameter of 3.4 nm. Figure 33a shows the resonant PL spectrum of the wurtzite core together with two different shell thicknesses added to the core (displayed relative to the excitation energy). The corresponding spectra of the zincblende series are shown in Sec. 11, Fig. 46, where both spectra are discussed in the context of band edge states. Here, again the Huang-Rhys factor can be estimated from the intensity ratio between second and first order of the phonon-replica. Since the process that is observed in this kind of measurement is different from Raman spectroscopy, it allows the direct determination of the intensity ratio is sufficient.

The shell thickness dependent Huang-Rhys factor for the examined wurtzite and zincblende series is shown in Fig. 33b. Here too, the coupling goes down upon shell addition, for both wurtzite and zincblende structure. However the effect isn't nearly as pronounced as it appeared observed by Raman spectroscopy. This indicates that the effect observed in Raman, definitely is enhanced by the shift in electronic transitions caused by the addition of shells, but the overall reduction in exciton-phonon coupling remains true. Additionally it can be observed that the coupling in the wurtzite QDs is generally larger than for zincblende QDs, by about a factor of 1.5, as was also observed in Raman (Fig. 31). As the wurtzite structure exhibits internal pyro- and piezo-electric fields, a larger coupling of the electronic system to lattice vibrations is to be expected. However the difference is smaller than anticipated, assuming a completely field-free and symmetric zincblende QD.

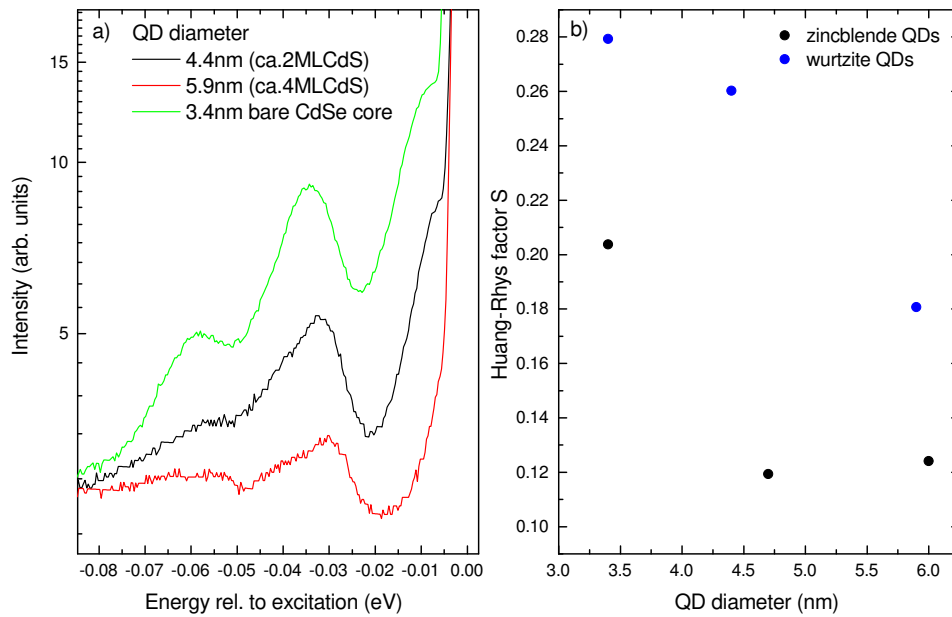


Figure 33: a) Resonant PL spectra (5K) of the wurtzite CdSe/CdS core-shell series, displayed relative to the excitation energy for comparison. The 2-3 phonon replica are visible, the zero phonon line lies several meV below the excitation indicating a transfer mechanism. b) Huang-Rhys factors determined from fits to the FLN measurements for zincblende and wurtzite core-shell. Wurtzite QDs have consistently higher coupling factors and for both structures the coupling reduces for addition of a CdS shell.

Despite revealing these very interesting coupling factors for different core-shell QDs, one problem with this method of measurement at low temperatures becomes obvious upon close inspection of the spectra in Fig. 33a. The phonon replica are replica of the bright state, but of the “dark” state that is located several meV below the bright state and becomes activated at low temperatures. This can be seen by the zero-phonon-line that doesn’t coincide with the excitation, but is a separate feature. Hence the observation made here, reveal the coupling factors to a different state. This could be avoided using higher temperature during measurement.

It is notable, that the order of magnitude is indeed the same as observed by Raman spectroscopy (0.1-0.2), despite the wide range discussed in the literature. While the coupling factors determined by Raman spectroscopy indicated a higher coupling when the measurement would be closer to resonance, the Huang-Rhys factor S observed by PLE, with values around 0.2 for zincblende, is slightly higher but close.

11 Excitonic fine structure of CdSe QD

The band edge fine structure of wurtzite colloidal CdSe QDs was studied by Nirmal et al.[127], using a combination of photoluminescence excitation spectroscopy (PLE) and fluorescence line narrowing (FLN), already in 1995. A theoretical description followed soon after by Norris et al.[128] and Efros et al.[83], in cooperation with each other. They showed a size dependent fine structure splitting for wurtzite colloidal CdSe QDs, together with a theoretical description based on the crystal field splitting in the wurtzite structure. This crystal splitting field is induced by anisotropy and results in at least five states lying close together at the band edge, of which only three should be optically active due to selection rules.[129–131] The optically active transitions are called $\pm 1^L$, $\pm 1^U$ and 0^U in order of ascending energy for prolate structures. For oblate structures however, the order of $\pm 1^U$ and 0^U is interchanged. Additionally, energy levels related to forbidden transitions, which should be optically inactive, the ± 2 and the 0^L are present. The lowest excitonic state in oblate structures is the 0^L state, as opposed to prolate structures, where it is the ± 2 state. Hence both forms have in common that the lowest excitonic state belongs to a optically forbidden transition. Despite being forbidden or “dark” – as this characteristic is often called – the ± 2 transition is clearly visible in measurements as a zero-phonon line (ZPL) in FLN spectroscopy.

Why this “dark” state becomes optically active, however, has been widely speculated over time. Recently, Rodina et al. have presented a comprehensive study discussing the possible activation processes and what consequently should be observable in measurements.[132, 133] The optical activation of the “dark” exciton is discussed in connection with dangling bond spins at the QD surface, phonons and the magnetic field. The resulting temperature dependencies of the recombination probability are presented, which provides an option to experimentally determine the activation process. In our experimental conditions, only recombination *via* interactions with dangling bond spins or phonons are possible, as no magnetic field is present.

On the other hand, Sercel *et al.* have just recently presented calculations showing that the dark state can be activated by the breaking of symmetry introduced by doping.[134] As impurities, introducing a charge to the QD are possible principally, this could also provide an explanation for the optical active “dark” state observed in our measurements.

Biadala et al. recently presented – together with Rodina – the formation of a magnetic polaron in colloidal CdSe QDs under the influence of high power excitation at cryogenic temperatures[135]. This, on one hand, increases the splitting between dark and bright states, which can be observed in measurements. This was explained by the formation of a dangling bond magnetic polaron, consisting of about 60 oriented dangling bond spins and one dark exciton. On the other hand, the dangling bond spins assist in the radiative

recombination of the forbidden “dark” exciton.

Beyond the wurtzite crystal structure, the zincblende structure should not exhibit crystal splitting because of its high symmetry. However, an anisotropy can be induced in zincblende QDs by any deviation from a perfectly spherical form. Here, deformations on the order of a few percent could cause an observable splitting of the band edge state. Since most published studies so far either focussed on wurtzite QDs – or did not mention the crystal structure at all – this is a very interesting aspect for the understanding of the electronic states in colloidal QDs.

In this chapter, we will analyze series of both wurtzite and zincblende CdSe QDs with varying diameters by PLE (for the experimental setup, see section 6.2), in order to investigate and compare the size dependent electronic fine structure near the band edge for both crystal structures. These series consist of 9 samples each, varying in diameter between 3.0 nm and 6.3 nm for the zincblende structure, and between 3.4 nm and 5.4 nm for wurtzite. A broad diameter range is thus covered for both crystal structures. For all QD samples, the mean diameter distribution within one sample is about $\pm 5\%$. The observed transitions will be compared with calculations of the electronic fine structure, taking into account the electron-hole exchange interaction, the influence of the different lattice types and possible shape anisotropy of the QDs. In order to observe which influence a CdS shell has on the electronic fine structure, an analysis of both zincblende and wurtzite series of core-shell QDs with different shell thicknesses will be given.

11.1 CdSe QDs in PLE measurements

In this section, PLE spectra of colloidal CdSe QDs (setup see Sec. 6.2) will be presented, followed by a discussion of the observed features. Furthermore it will be demonstrated how the measured PLE and FLN can be used to extract transitions for a broad diameter range of wurtzite and zincblende QDs.

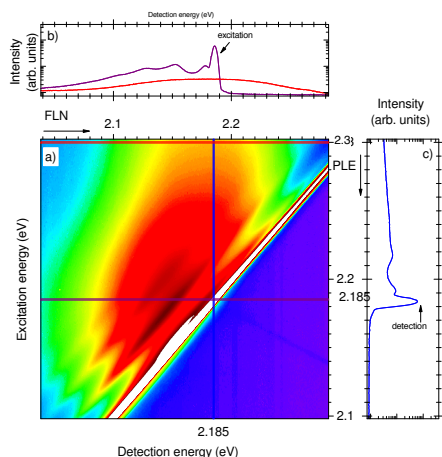


Figure 34: PLE measurement of 3.6 nm zincblende CdSe QDs at 5K. a) Contour plot of PL intensities (logarithmic scale) for varied excitation energies. b) Profile for a fixed excitation energy, non-resonant PL (red line, 2.300 eV). In resonance (violet line, 2.185 eV) this profile is called FLN (fluorescence line narrowing) due to the strongly enhanced signal of the resonant states. c) Excitation profile for a fixed detection energy, here 2.185 eV.

Figure 34 shows a PLE contour plot of zincblende CdSe QDs with an average diameter of 3.6 nm. The color reflects the intensity for each energy, going from low intensity (violet) to high intensity (red). Evaluating a profile through the color plot in the x-direction yields a regular PL spectrum, as shown in Fig. 34 b). Along the y-axis, on the other hand, this results in an intensity profile for a fixed detection energy under varying excitation (Fig. 34c)). If the excitation energy becomes resonant with a distinct state, the PL process becomes very efficient, thus the intensity increases. Looking at the different PL profiles in more detail (Fig. 35), very different spectra can be observed *in* and *off* resonance. When excited off resonance (red), the QD ensemble emits a Gaussian-shaped signal, which is broadened due to the diameter distribution within the sample. This changes dramatically when the the sample is excited in resonance, see profile shown in violet (Fig. 35). As there is resonance only with a certain sub-sample of QDs, the line width is strongly reduced; hence this is commonly called fluorescence line narrowing (FLN). This effect is especially noticeable at energies which are smaller than the mean emission energy of the sample, as this limits the number of excited QDs.

The FLN profile evidently reveals a more complex structure than the off-resonant PL spectrum, including a zero phonon line and subsequent phonon replica. The phonon energy is in agreement with the phonon energy we observed in Raman experiments. The zero-phonon line corresponds to the

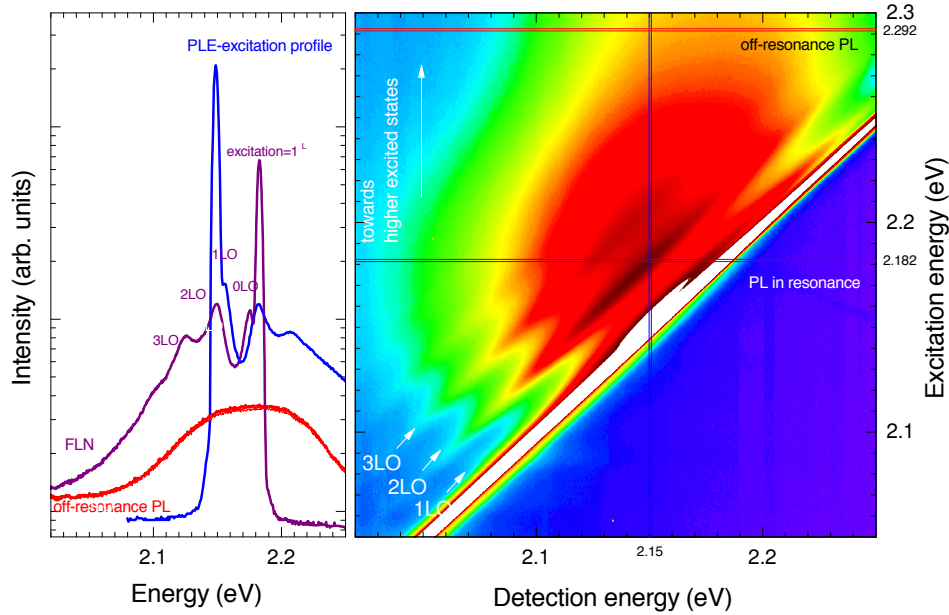


Figure 35: PLE contour plot of ≈ 3.6 nm sized zincblende CdSe QDs. Line profiles at 2.182 eV (FLN, violet) and “classical”, off-resonant PL 2.292 eV (red) are given on the left. Text labels indicate the positions of the zero-phonon line and the phonon replica. Additionally, the PLE profile detected at the position of the 1LO in the resonant FLN profile is displayed (blue).

dark state. Additionally, the excitation profile along the y-axis is given in Fig. 35 (blue), which includes several resonant states when going towards higher energies. For a better overview, the position of each state is given in dependence of excitation energy (FLN profiles) and the 1^L energy (PLE profiles) in Fig 36. While this scatter plot combines all 9 QD samples of the zincblende series, the shown states still line up and evidently give a clear energy dependence, albeit within a small statistical spread. This indicates that we can retract information on QDs of different sizes more or less continuously simply by tuning the excitation energy, and it highlights that in resonant excitation, the FLN spectrum is dominated by a small sub-ensemble of QDs. Energies below zero correspond to states identified from the FLN spectra (i.e. along the x-axis in Fig. 35). Here we find the zero-phonon line, which marks the position of the “dark” state ± 2 . Furthermore, the first, second, and third phonon replica of this state can be seen. Depending on the QD diameter, the phonon replica shift more or less parallel to the “dark” state. Even though there is a small diameter dependence of the Raman shift (Sec. 8.2), a shift is not visible in these measurements, as it is far below the resolution of the measurement.

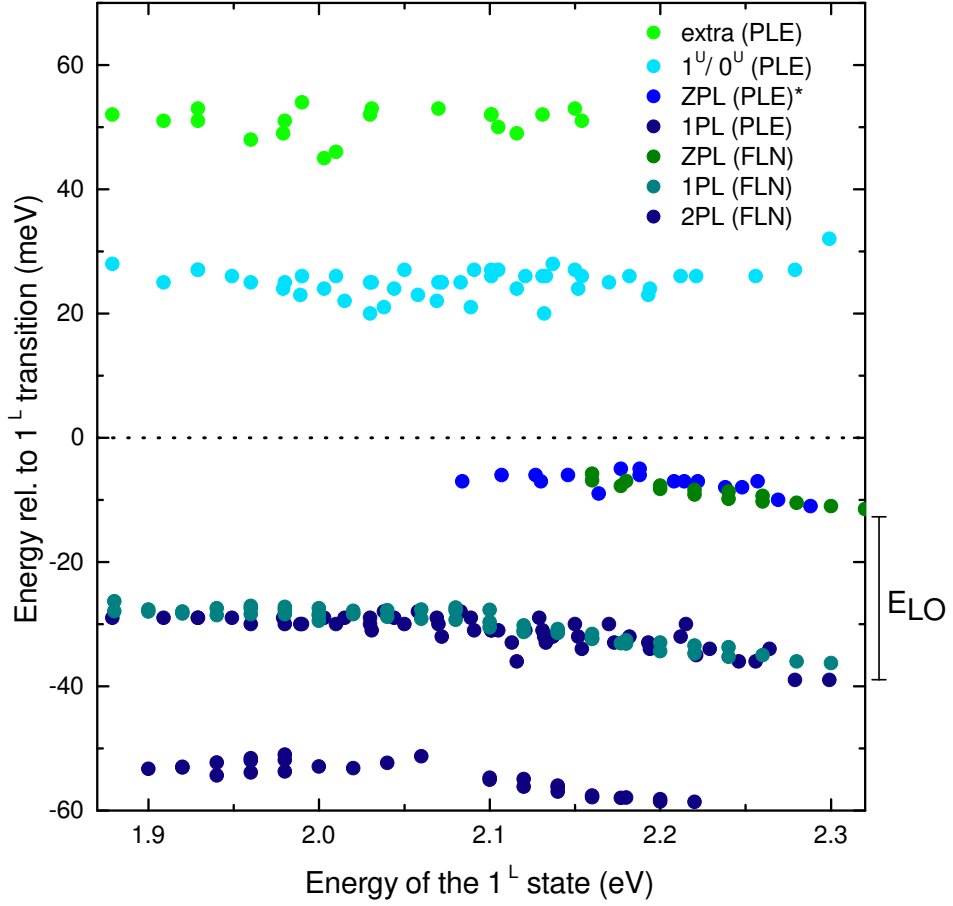


Figure 36: Overview of all near band edge states observed by taking profiles in PLE and FLN for the whole zincblende diameter series. The states are displayed relative to the 1^U state, i.e. the bright state, which is observed as the main transition in off-resonant measurements. Energies above zero are observed in PLE, those below in FLN profiles. Two band edge states with energies above the 1^L state emerge, one of which can be attributed to the mixture of 1^U and 0^U states, analogous to Norris and Efros. Below the 1^L state, a zero-phonon line (ZPL) and the subsequent first and second phonon replica (1PL/2PL) are observed. The displayed values for the ZPL are collected from FLN profiles (ZPL(FLN)) and from PLE profiles (ZPL(PLE))* . The ZPL(PLE)* values shown are calculated from the observed location of the feature above the detection energy in the PLE profile, identifying this feature to a ZPL belonging to the known excitation energy(both values are known quantities). In this way, the ZPL observed in PLE is displayed analogue to the ZPL observed in FLN. The ZPL corresponds to the “dark” state, the ± 2 state, that is evidently optically active for these structures. The 1PL observed in PLE profiles matches with the 1PL observed in FLN. Combining the observed states of all samples leads to continuously energy dependent states, without any steps; hence extrapolations between the discrete, average diameters of the series are evidently allowed.[83, 128]

Towards positive relative energies, we find two higher states with weak diameter dependence, of which the lower energetic one was attributed by Norris and Efros to be a combination of 1^U and 0^U . As the 1^U and 0^U states are energetically very close, they overlap and are often indistinguishable in measurements. Note that they did, however, observe separated features for larger QDs, above 6.2 nm in diameter. Since our wurtzite QD series ends at a diameter of 5.4 nm, we can unfortunately not verify this separation of states. From consultations with our cooperations partners – who synthesized the samples – it has become clear, however, that the size distribution becomes quite broad at larger diameters, and the QD are prone to show ripening effects, which can lead to non-spherical QDs. In the wurtzite crystal structure, QDs tend to form elongated (prolate) forms in case of ripening. For spherical zincblende QDs, this deformation is usually not observed by TEM, which means that only oblate deformation is possible. A oblate deformation would not be difficult to observe by TEM due to the orientation of the QDs, the images being predominantly perpendicular to the deformation. This would subsequently lead to a diverging anisotropy within the series, hence make a complementary description very difficult.

To compare the different crystal structures with each other, one can either compare the different transitions in dependence of the 1^L energy, or in dependence of the corresponding QD diameter. For the latter, a relation between the emission energy and the QD diameter at the temperature of the measurement needs to be found. Such a conversion is presented in the following section 11.2, and applied thereafter. The successful conversion of emission energies into QD diameters entails the additional benefit of the possibility of simulating the electronic fine structure, which was kindly performed by Anna Rodina and Alexandr Golovatenko, and will be presented in Sec. 11.4 of this work.

For the accuracy of these calculation, we must first ensure that the measurement itself does not influence the energy of the observed states. As shown by Biadala et al.[135] – together with Rodina – the high power excitation (e.g. by laser irradiation) leads to increased magnetic polaron effects, which would need to be accounted for in the calculations. In contrast to an energetic splitting which is based on fine structure only, these polaron effects should be strongly dependent on the temperature. Consequently, we show the temperature dependence of the observed states in Sec. 11.3, and reveal that no temperature dependent shifting of the states can be observed in our experimental conditions.

11.2 Determination of the energy to size conversion at low temperatures

In order to compare the band edge states of the wurtzite QD series with those from the zincblende series, it is necessary to compare the band edge

states in dependence of the QD size. Here, a relation is required to translate the transmission energies at the temperature of the measurements (5K) into corresponding QD sizes. Since the mean diameters of our samples are known either from TEM measurements or – *via* subsequent consultation of known size relations – from room temperature absorption measurements, we merely need to connect these with our measured lowest energetic transitions for each sample at 5 K.

Fig. 37 shows the mean diameter dependence of the lowest energetic transition for off-resonance excitations in wurtzite and zinblende QDs. Both zinblende and wurtzite QDs exhibit lower transition energies for larger QD diameters, which originates from the lower quantum confinement present in larger QDs. For similar sizes, the wurtzite QDs show higher lowest transition energies than the zinblende QDs. This originates from the internal fields in the crystal structure, which further separate the electron and the hole states.

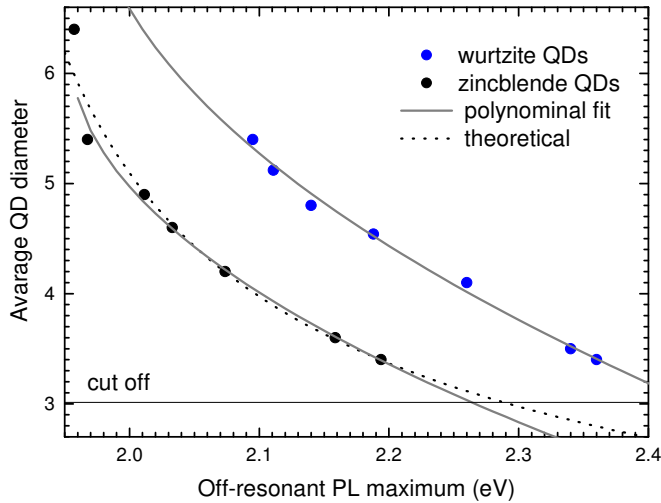


Figure 37: Average QD diameter as a function of the main optical transition in off-resonant PL, as determined from our PLE measurements. The fits required for a successful energy-diameter-conversion are displayed and discussed in the text.

In the strong confinement regime, the transition energy dependence on the QD size can in principle be described with a classic:

$$E_g = E_{g,bulk} + E_{conf} = E_{g,bulk} + \frac{2\hbar^2\chi_{nl}^2}{m_e^*D^2} + \frac{2\hbar^2\chi_{nl}^2}{m_h^*D^2} \quad (22)$$

with D as the effective diameter, $m_{e/h}^*$ the effective mass of hole/electron, χ_{nl} the roots of the Bessel function solving the corresponding Schrödinger equation. (After [136])

For simple cases, it should hence be possible to describe the diameter dependence of the lowest energetic transition with a quadratic function $E = E_0 + \frac{A}{D^2}$. Here the fit parameter c ($c > 0$) represents the influence of confinement on the structure and E_0 is the base energy. Even though this

works for the zincblende QDs, as shown in Fig. 37, this equation does not describe wurtzite QDs well. This might originate in their more complex crystal structure, which has a lower symmetry and also includes internal pyro- and piezo-electric fields, which influence in electronic and hole states. This is often compensated with the the introduction of an additional $-B/D$ term, to account for the coulomb attraction (B positive, $B \ll A$). This term has successfully been used, for instance, by Moreels et al. for rock-salt PbSe[137]. It does, however, not improve our fit sufficiently. For very small QDs, an additional influence of the fine structure splitting might be observable, which could be described with an additional $-C/D^3$ term. For the present wurtzite CdSe QDs at low temperature, however, the inclusion of all these extra terms yields unphysical values, and hence should neither be used for physical interpretations nor the size conversion.

To have a consistent procedure, we therefore use polynominal fits (also used by Moreels et al.[137], for instance) to describe the relation between energy and QD diameter for both crystal structures. These polynominal fits, shown in Fig. 37, only deviate marginally from the measured data points and hence represent the data well. Note that for the zincblende QDs, the polynominal fit and the fit based on confinement energy show only very small deviation. For the intended conversion of the measured transition energies of sub-ensembles to their respective mean QD diameters, it is necessary to reverse the function. To avoid an extrapolation too far beyond the present size data, we use 3 nm as a cut-off for the diameter conversion (see Fig. 37), since the deviation between the theoretical fit and the polynominal fit is small above this point. This will be applied to our experimental findings and results will be discussed in section 11.4.

11.3 Temperature dependence of the near band-edge states

A high excitation energy can lead to a polaron formation at low temperature for CdSe QDs, which induces an increased Stokes shift to the “dark” exciton.[135] Since this effect is strongly temperature dependent and breaks down easily, the temperature dependence of the observed states is investigated in this section.

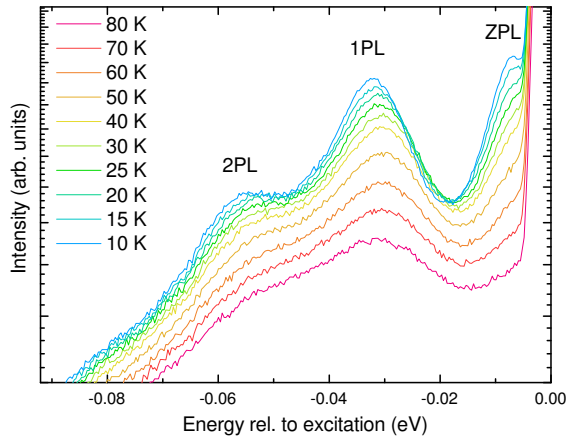


Figure 38: Temperature dependence (between 5 K and 80 K) of FLN spectra for ≈ 3.6 nm sized zincblende QDs at a fixed excitation energy (off resonant PL maximum at 5K).

Figure 38 shows FLN spectra of ≈ 3.6 nm zincblende QDs in the range between 5 K and 80 K for a fixed excitation energy. It becomes clear that the zero-phonon line can not be observed anymore at temperatures above 60 K. Unfortunately, the exact location is difficult to identify from direct observation, yet also can't be easily calculated from the first phonon replica (1PL) position, since the phonon frequency is also temperature dependent (Sec. 9). The intensity of all features reduces for increasing temperature, while the one of the features of the polaron is, that it increases the relative ZPL intensity with T. The fact that the ground state also shifts over temperature is however not taken into account in this picture, which could mean that a sub-ensemble of QDs is actually analyzed at higher temperatures is a different sub-ensemble, due the temperature induced shift of electronic transitions.

To overcome the influence of different sub-ensembles on the temperature dependence, we analyzed the observable states in Fig. 39 for a number of samples (4) at the "elevated" temperature of 60 K, the highest temperature where the ZPL is still observed. These energy dependent states can now be directly compared with the states observed in measurements at 5 K.

Comparing the points for 5 K and 60 K in Fig. 39, we find no dependence on temperature for the zero-phonon line, as well as for the state above the bright state. The phonon replica, however, show a small shift toward lower energies, which is in good agreement with previous observations by Raman spectroscopy (see Sec. 9).

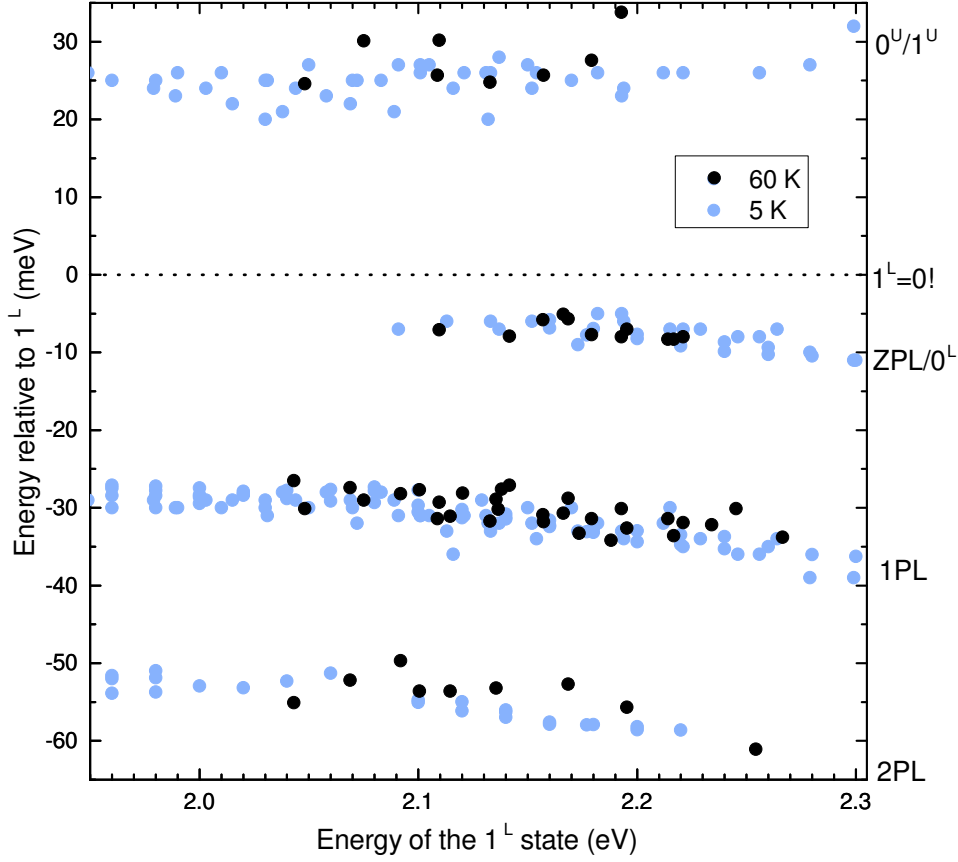


Figure 39: Comparison of states of 3 exemplary zincblende QD samples (3.6 nm, 4.0 nm and 4.2 nm) for 5K (blue) and 60K (black): apart from a smaller phonon energy at higher temperatures (agreement with Sec. 9) no shifts visible. The higher lying states are not observed anymore at 60 K and are hence not shown.

This temperature independence of the dark state energetic position indicates that we don't observe effects caused by the formation of a polaron, but rather a purely exchange interaction based splitting of the band edge state. This is possibly due to the low excitation intensity employed in this experiment, where we use a lamp instead of a laser for excitation. Additionally the excitation and detection is distributed over an area of about 1 cm^2 , which further reduces the power density.

In summary, polaron effects can be neglected when describing the states observed in this work.

11.4 Fine structure dependence on QD size, emission energy and crystal phases

After having found a suitable function to convert emission energies to the corresponding QD diameters in Sec. 11.2 for the two different crystal structures, it is now possible to compare the fine structure of the diameter series. Figure 40 shows the near band edge states – which were extracted from the PLE measurements of the wurtzite diameter series – as a function of the 1^L state and of the calculated QD diameter. As mentioned in the previous chapter, the conversion is reasonable down to a diameter of 3 nm, which causes a small reduction of usable data points in this region. The fact that the energetic splitting between the 1^L state and the ± 2 state increases for higher excitation energies automatically results in an increase of splitting for decreasing QD diameter.

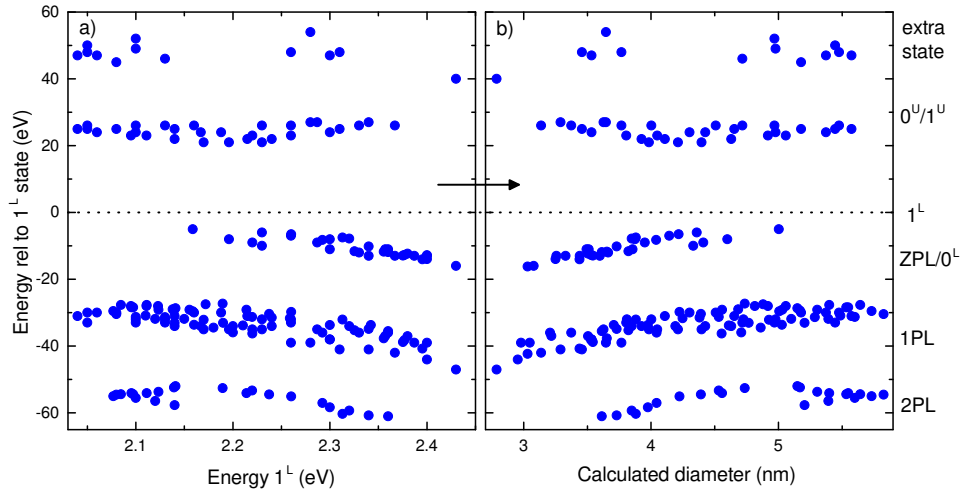


Figure 40: Transitions extracted from the PLE measurements for the wurtzite CdSe QD diameter series a) as a function of the 1^L energy and b) as a function of the calculated QD diameter (conversion see Sec. 11.2). Energies are shown relative to the 1^L energy, the transitions are labeled on the right side.

An overview of the different observed states for the wurtzite and zincblende phase is given in Fig. 41 as a function of the 1^L state and the calculated QD diameter. In the energy dependence as well as the diameter dependence, most prominently the separation between the 1^L state and the ± 2 state (bright and dark state) is higher for the wurtzite QDs and increases for higher energies (smaller diameters). However this different behavior of the crystal structures is strongly increased, looking at the diameter dependence, highlighting the differing electronic properties of the zincblende and

the wurtzite structure. This splitting between “bright” and “dark” state is accentuated by the equally distanced phonon replica to the dark state, showing the same offset between the structures. However, it becomes clear, that the conversion to QD diameter changes the outward appearance of the figure and must be carefully considered. Additionally, wurtzite QDs show more scattering in the observed transitions in PLE than the zincblende QDs, indicating less homogeneous samples.

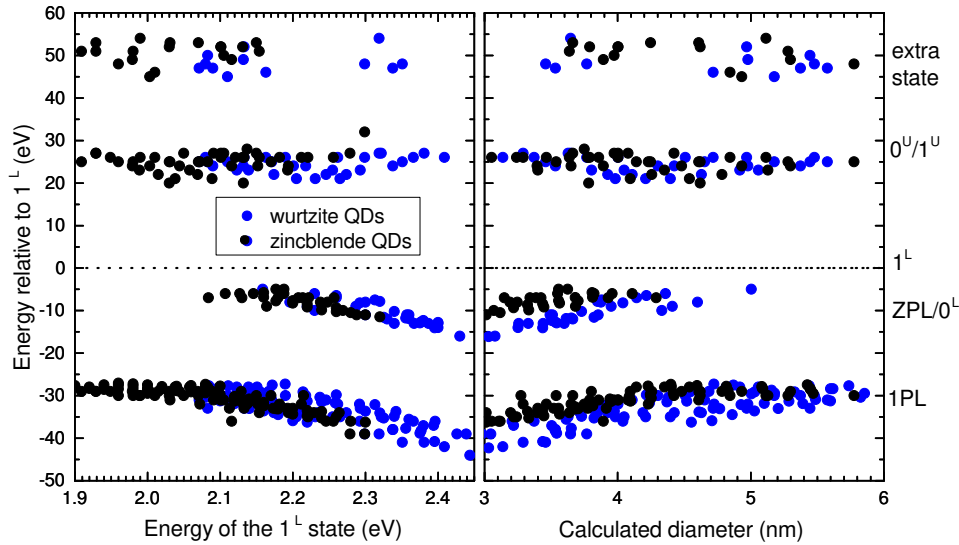


Figure 41: Transitions extracted from the measured PLE contours for the wurtzite and zincblende CdSe QD diameter series in comparison a) in dependence of the ± 2 energy and b) in dependence of the calculated QD diameter (conversion see Sec. 11.2). Energies are shown relative to the 1^L energy, the transitions are labeled on the right side.

Based on these findings, it is our goal to find a coherent description for the observed states for both structures. Therefore, fine structure calculations were performed in the group of Anna Rodina. To achieve a description of the states in zincblende QDs, a possible deformation of the QD has to be taken into account. For perfectly spherical QDs, there should be no dark state observable; a small distortion in QD form, however, already leads to a splitting between bright and dark state.[138]

Figure 42 shows the results of this calculation for wurtzite QDs, including only a purely spherical form. The best fit to our data is achieved using an exchange strength constant $\epsilon_{exch} = 500$ meV (for nomenclature, see [83]), which corresponds to a singlet-triplet splitting equivalent for a bulk semiconductor to $\hbar\omega_{ST} = 0.2$ meV. Norris and Efros found a good fit for $\hbar\omega_{ST} = 0.13$ meV and $\epsilon_{exch} = 320$ meV [128, 139], which is lower than the parameter deter-

mined from our data and equals the previously determined singlet-triplet splitting in bulk CdSe. But also higher values for the exchange parameter have been determined, up to 500 to 1000 meV for 1-2 nm sized CdSe QDs[140]. This shows that the parameters observed here are well within the range of previous findings. Additionally these parameters might even be influenced by sample specific properties like crystal quality, growth conditions or sample preparation. Furthermore, the calculation only focusses on short-range exchange interaction, the addition of long-range interaction to the calculation, as done by Goupalov and Ivchenko[141] could improve the model.

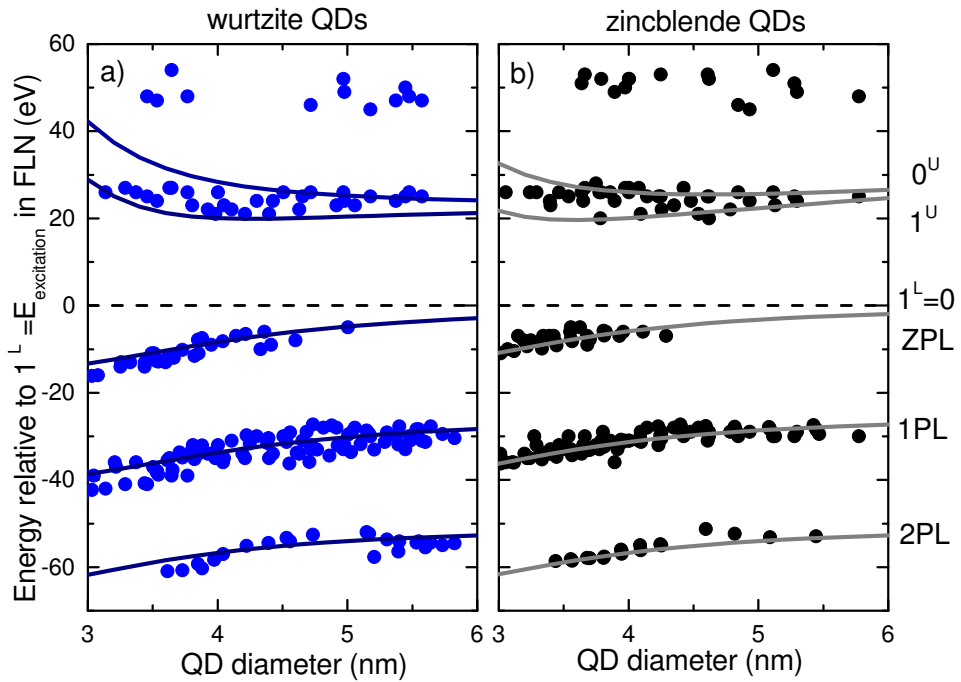


Figure 42: Observed transitions of wurtzite (a) and zincblende (b) CdSe QDs, shown as a function of the calculated QD diameter. Also shown are calculated transitions (lines), using the following parameters: a) $\hbar\omega_{ST} = 0.2$ meV, $\epsilon_{exch} = 500$ meV for wurtzite and b) $\hbar\omega_{ST,zb} = 0.13$ meV, $\epsilon_{exch} = 160$ meV for zincblende. For the latter, the fit can only be realized by introducing a variation to the deformation of the QD shape. This ranges from 10% oblate to 50%, the variation is displayed in Fig. 43.

The resulting fit identifies the state right above the bright state as a combination of the close-lying states 1^U and 0^U . Note that the energetically highest stat is not included in the fine structure, and must originate elsewhere.

For the zincblende QDs, this calculation is more complicated due to the

necessary variation of form deformation, which leads to more adjustment possibilities. On one hand, we can expect only moderately deformed QDs, else one would clearly see the deformation in TEM measurements. This can reasonably assumed to be less than 15-20% deviation of QD height compared to the QD width (see inset of Fig. 43). On the other hand, any deviation from the perfect sphere must be great enough to facilitate a bright-dark splitting of up to 12 meV, which is in the same order of magnitude as that of wurtzite QDs. Furthermore, in order to reach a description comparable to that of the wurtzite QDs, the 1^U and 0^U state should be located close to the lower energetic upper state. But as it turns out, this fit can only be realized for the zincblende QDs by considering a varying anisotropy between 10% for small QDs, to up to 50% for large QDs, going from slightly oblate to *very* oblate. The shape variation is shown in Fig. 43, and the fit resulting from the variation is displayed in Fig.42.

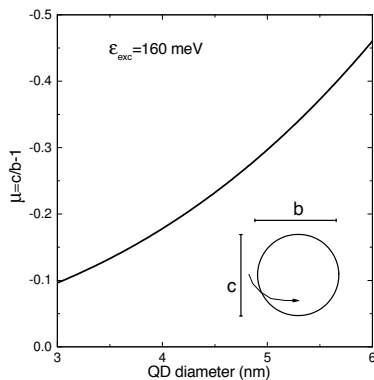


Figure 43: Deviation from the ideal spherical form of the QD, which is used to calculate near band-edge states as shown in Fig. 42 in dependence of the QD diameter. The deformation $\mu = c/b - 1$ is given as a function of the diameter, where c is defined as the height and b as the width of an ellipsoidal QD (see inset sketch, arrow indicating rotational symmetry).

Such a high shape deviation from that of a sphere should be readily visible in TEM measurement and was not observed for the samples. This shows, that different possible origins of the observed higher states must be explored.

Consequently, we must revisit the possible processes which can result in the intensities observed in the FLN and PLE profiles given in Fig. 44. Since most visible features are already identified as phonon replica of what was previously attributed as the “dark” state, assigning the other processes is more or less straight forward for the FLN profile. This “dark” state shows a strong coupling to the phononic system, as can be seen in the presence of up to three phonon replica. In the PLE profile (vertical profile in Fig. 44), there can thus be different explanations for the areas of higher intensity in the PLE contour. On one hand, a possible resonance to a higher energetic state of the electronic structure (for the lower one: fine structure) might cause increased intensities; on the other hand, this could also be a result from phonon replica of resonantly excited smaller QDs (i.e. larger

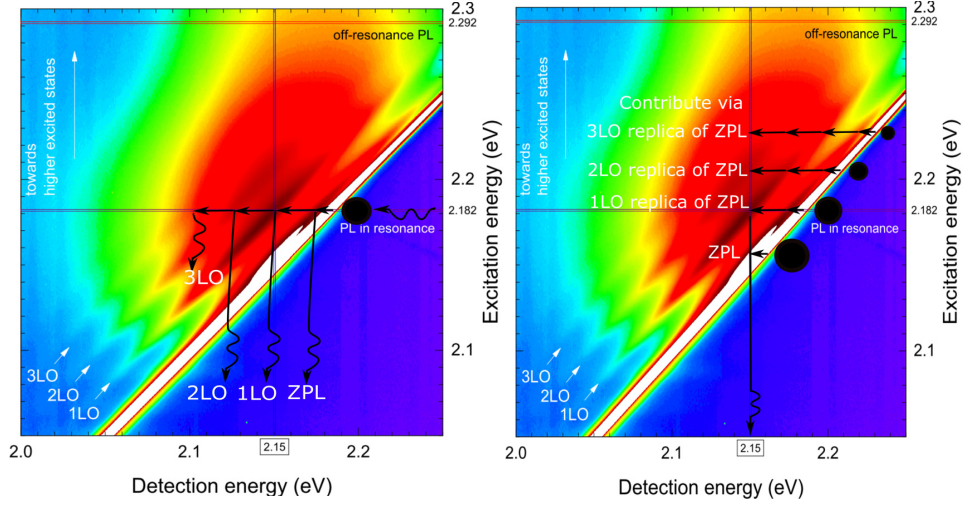


Figure 44: Possible processes that can lead to the observed lines of higher intensity in the PLE contour plot. Left: a photon with discrete energy excites a state and relaxes to the ZPL, the observed emission along the FLN profile stems from ZPL and phonon replica. Right: PLE profile for fixed detection energy. Areas of high intensity can originate from the phonon replica of excited QDs which have a smaller size/higher ground state energy, as indicated by filled black circles.

band gap), as shown in Fig. 44. Such phonon replica would result in 2-3 equally separated features in the PLE profile, depending on how many phonon replica are visible in the FLN profiles.

Figure 45 shows where these phonon replica would appear in the PLE state diagram (see Fig. 44). While this model predominately addresses features appearing in PLE profiles (i.e. those with energies above the bright state 1^L), the fine structure must still be calculated for a full description of observed states, as it causes the bright-dark exciton splitting that was observed in FLN profiles. The calculated states in Fig. 45 are determined with the same parameters as previously used for wurtzite QDs. For zincblende QDs, this allows us to assume a more realistic deformation of 10% in oblate direction, and still find a suitable fit to the data. Figure 45 shows the best fit for the zincblende QDs, which uses an exchange strength of $\epsilon_{exch}^c = 160$ meV (corresponding to bulk singlet-triplet splitting equivalent of $\hbar\omega_{ST,zb} = 0.13$ meV). It can be assumed that the exchange constant is the same for zincblende and wurtzite structure, the exchange strength constants need to be scaled according to the volumes of the unit cells of the structures, $\epsilon_{exch}^c = \epsilon^w(v_w/v_c)$, with v_w/v_c as the volume of the unit cells. This, combined with the two-fold larger unit cell volume of the zincblende crystal structure, should lead to twice smaller exchange constants for zincblende structures. Here, the ex-

change strength of the zincblende QDs is smaller than half the exchange strength of the wurtzite QDs, which could hint toward a different exchange constant for the two crystal structures.

Evidently, features emerging from phonon replica of excited QDs with a higher ground state energy within the ensemble appear at energies that coincide with the two observed higher states for the zincblende QD. For the wurtzite QDs, the energetically lower feature lies at the same energy as the 1^U and 0^U states, thus it is impossible to differentiate between those two possible explanations. Remarkably, the previously unexplained feature at higher energies can now be successfully attributed to the second phonon replica of QDs excited with higher energetic ground state.

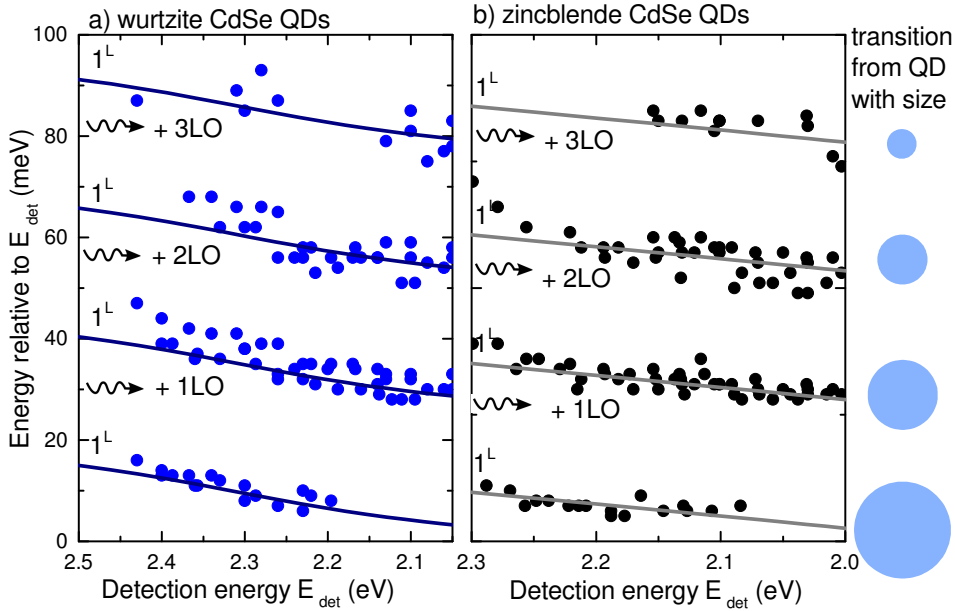


Figure 45: Transitions observed in PLE profiles as a function of the detection energy, for the complete wurtzite a) and zincblende b) series. The phonon replica of the 1^L state from *smaller* QDs coincide with the observed features in PLE.

This model can explain both observed PLE states for wurtzite and zincblende QDs, and predict the size dependence using realistic parameters for simulation. It, however, raises the question why the rest of the fine structure is not visible. This can only originate from a very efficient and very fast relaxation into the lower energetic states. Indeed, browsing the literature, we consistently find intra-band relaxation rates in the nano second range observed by time resolved PL (TRPL)[142–144]. Those relaxation rates have been shown to strongly depend on the surface ligand, of which

TOPO and TOP, the ones present in this work, lead to the fastest relaxation time of about 6 ps.[144] Others found a femto- to picosecond time scale for intraband-relaxation.[142, 143]

The diameter dependent fine structure observed by PLE reveals a generally higher splitting between the transitions for smaller QDs. Differences, however, can be found between wurtzite and zincblende QDs. The separation between the observed states is larger for wurtzite QDs, which makes sense considering the crystal field splitting within this structure. This trend is visible in the diameter dependence, as well as in the dependence on ground state energy; as the relation between energy and size is different for wurtzite and zincblende QDs. The calculation of band edge states for zincblende QDs is possible by taking a deformation in oblate direction into account. The 1^U and 0^U states, however, can only be the origin for the observed PLE transitions if a high, varied deformation is assumed. Hence a different interpretation is presented, which not only coherently explains observed features both in wurtzite and in zincblende QDs, but also an additional feature which is observed for both of them. Especially the latter provides a clear advantage over previous calculations. All features above the 1^L state can be explained by considering LO replica from excitations in smaller QDs within the ensemble. This indicates a very fast relaxation process to the “dark” exciton and emphasizes the importance of phonons and the apparently very efficient coupling to them.

11.5 Excitonic fine structure in CdSe/CdS core-shell QDs

In addition to the diameter dependent analysis of the electronic fine structure of wurtzite and zincblende QDs, we have investigated the influence of the addition of a CdS shell on the bright state - dark state splitting. For this, we analyzed different core-shell QDs with varied CdS shell thickness. The two shell thickness series were both based on a core with a diameter of ≈ 3.4 nm, one wurtzite and one zincblende. Note that the same cores were ones used in Sec. 9 and 8.2. Here, only those with comparable and thin shell thicknesses were investigated in PLE, because of their clearly visible CdSe phonon replica. Figure 46 shows the FLN profiles for each sample series, resonantly excited in the respective bright state. Note that this state depends on the shell thickness, see Sec. 8.1. To compare the relative locations of the ZPL and phonon replica, the data is displayed relative to their excitation energies. The most prominent difference between the spectra is that the whole phonon structure is much better separated in the zincblende series, where the separate CdSe and CdS LO replica are clearly visible. While the CdS phonon should be primarily confined to the shell and the exciton is mainly located in the core, this clearly demonstrates that the exciton couples with both core and shell phonons. Here, it is possible that the exciton mainly couples to CdS phonon modes localized to the interface between

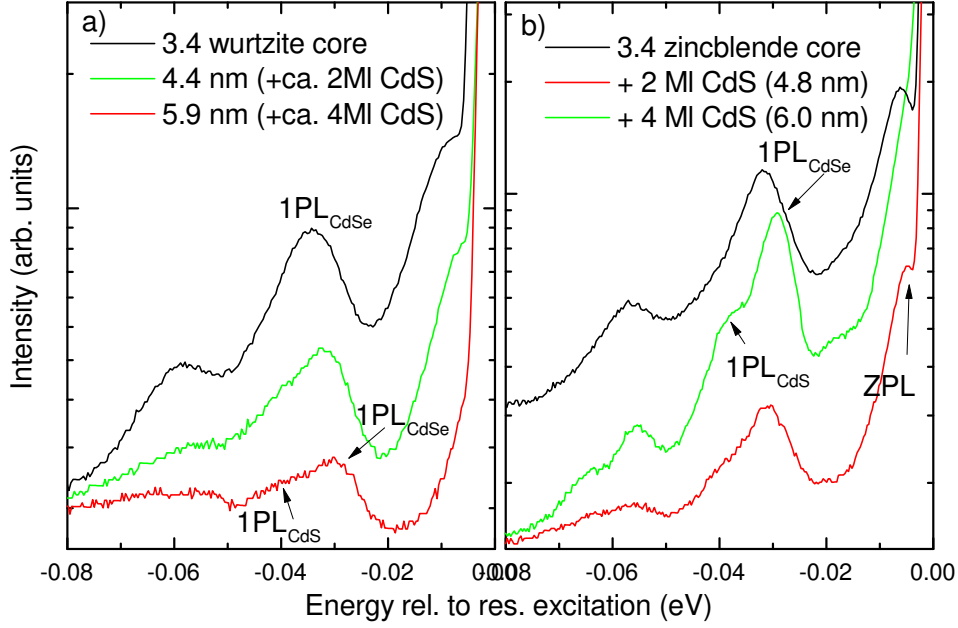


Figure 46: Resonant PL spectra (5K) of a) wurtzite and b) zincblende CdSe/CdS core-shell series, displayed relative to the excitation energy to compare relative locations of the ZPL and its phonon replica. Phonon replica are visible from the CdSe LO phonon and the CdS phonon for the QDs with shell. The zero phonon line lies several meV below the excitation, which highlights the splitting between bright (1^L) and dark state (± 2).

CdSe core and CdS shell; this could induce lower frequencies than expected from Raman measurements, since the lattice constant in the interface region transitions between CdSe-like and CdS-like.

Only for small CdS coverages, the direct observation of the zero-phonon line is possible, especially for the wurtzite QDs. The Raman frequencies are, however, known for all samples from previous Raman experiments (see table 2) and are used to determine the location of the dark state despite the lack of direct observation. The subsequently uncovered relations between the states are shown in Fig. 47. In order to uncover the average fine structure for each ensemble, each QD is analyzed for excitations in the off-resonant PL maximum. For both crystal structures, the dark state shifts closer towards the bright state for increasing shell thickness. On one hand, this could be an effect of the effectively increased QD diameter; on the other hand, it could be an effect of the interaction between core and shell, such as changed atomic bonds at the QD surface or strain induced by the shell.

In case the recombination of the dark exciton functions via dangling bond spins [133], the recombination should become less and less likely, the further the surface dangling bonds are moved away from the QD core. For the

present samples, the ZPL is not visible anymore for the 4ML shell thickness. Here, it is however not possible to determine whether this is due to a dampened recombination, or whether the ZPL is shifted too close to the excitation to be observed with the given resolution.

structure (wz/zb)	core diameter (nm)	shell thickness (nm)	ω_{LO} CdSe (cm^{-1})	ω_{LO} CdS (cm^{-1})
wz	3.4	-	202.9	-
wz	3.4	0.3	204.3	285.7
wz	3.4	1.3	208.2	295.4
zb	3.4	-	203.7	-
zb	3.4	0.7	207.6	289.0
zb	3.4	1.3	209.2	300.0

Table 2: Phonon frequencies of the CdSe and CdS LO mode, as determined by Raman spectroscopy at a temperature of 7K for all QDs studied in Fig. 46 and Fig. 47, given to compare the phonon replica shifting with respect to the strain in the QD’s core and shell. All Raman frequencies $\pm 0.5 \text{ cm}^{-1}$ (see also Sec. 8.2)

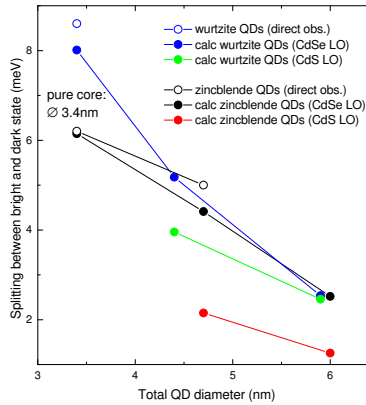


Figure 47: Splitting between bright (1^L) and dark state (± 2) (meV), as a function of total QD diameter. The latter is calculated from the 1PL line observed in resonant FLN via the phonon frequencies determined by Raman spectroscopy (Table 2). In tendency, the two states shift closer together upon shell addition, indicating a strong influence of the shell on the electronic states of the QD.

Not only the CdSe phonon couples to the “dark” exciton, the CdS phonon shows an energetic offset compared to the “bright” state of the CdSe core too. This energetic splitting however, is lower for the CdS than for the CdSe phonon replica. For the wurtzite QDs, the energy is the same as for the CdSe phonon; for the zincblende QDs, however, the phonon seems to couple to a state with lower energetic distance to the bright state. On one hand, this could indicate strong differences in the electronic properties in core-shell structures. On the other hand, for the recombination *via* the dark exciton, an interaction between the hole and the phonon is needed. The hole of the exciton is located in the CdSe core, hence the phonon must be as close as possible to the core to be able to interact. Those phonons,

right at the interface between the CdSe core and CdS shell, should exhibit a higher strain compared with the rest of the shell. This would lead to a strain induced shift in frequency (lower frequency), rendering phonons observed in PLE inequivalent to those measured by Raman spectroscopy (see Sec. 8.2, 8).

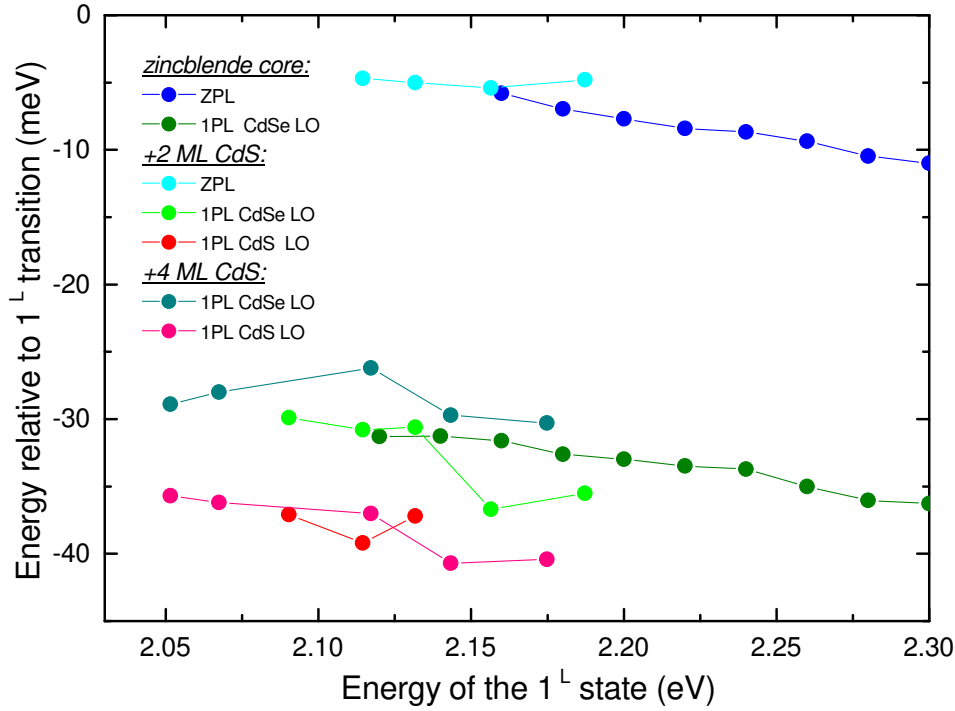


Figure 48: Excitation energy dependent ZPL and 1PL (CdSe, CdS) transitions, as evaluated for the three samples of the zincblende core-shell series shown in Fig. 46b), given here relative to the excitation energy. While each sample shows continuous shifts for the observed transitions, the shifts are, however, not continuous over the whole series.

For a better comparison of the states between bare core and core-shell QDs in Fig. 46, the energy dependence of the ZPL and its phonon replica is analyzed, just as for the diameter series in the previous section (11.4). This energy dependence is shown in Fig. 47 for the zincblende series, as those QDs exhibit an overall better separable phonon replica signal, possibly due to the smaller halfwidth which was also observed in Raman spectra. Compared to the uncovered QD, the ZPL of the core-shell QD with the lowest shell thickness is less dependent on the excitation energy, while also having an overall smaller separation from the bright state, as already observed above. This completely different trend in energy dependence emphasizes that the CdS shell must not only decrease the confinement of the QD (Sec. 8), but also completely changes the QD. As discussed in Sec. 8.2,

the CdS shell causes compressive strain in the CdSe core, which can cause a different anisotropy or deformation of the initial QD. This strain effects on the phonon energy alone, however, can't explain the observed trends, as the phonon energy of the CdSe and CdS LO both increase with increasing shell thickness. The 1PL of the thickest shell is actually even closer to the bright state than that of the bare core, which is in stark contrast with the observed trend in phonon energy. This indicates further mechanisms at play and highlights that this would be an excellent subject for further investigations.

12 Effect of a silica shell on the encapsulated QD

In this chapter, the effect of a silica shell addition on a CdSe/CdS Qd will be discussed. These shells are employed to make the QDs water-soluble and enable applications like the use as biological markers by creating a more or less inert and biocompatible shell that protects both, the biological cell from the potentially poisonous QD as well as the QD from a reactive environment. The chapter will begin picking up from the more motivational section 7.3 (and 4.1) where the application possibilities are described, and start off with a discussion of the state of the art and previous studies. This will be followed by our findings before and after silica coverage and the combined approach of in situ Raman and TEM measurements. The findings reveal an interface formation during the nucleation of silica on the QD surface, which will be discussed in detail in section 12.6, and demonstrate they can be used as visualization of the dynamics of this process.

Finally, we present the additional observation (section 12.8 and 12.7), that the Raman intensity can be used to follow the transition of the QD from one environment to the other during the encapsulation synthesis due to the changes in dielectric constant of the environment. This enables for the first time, to observe the transition of the QD into a water micelle within the reverse micelle growth of the silica encapsulation.

12.1 Previous studies by TEM, PL and absorption

A good overview over various synthesis routes for the silica encapsulation of various particles including metal particles, magnetic particles and inorganic semiconductor particles and synthesis of larger meta structures combining silica with particles is presented by Guerrero Martinez et al..[23] They claim that a precise control over the synthesis and especially the thickness of the isolating shell is the key to ensure a good response of the particles of an external stimulation by incoming light or applied magnetic fields and underline that once this has been optimized the payoff will be considerable due to the high functionality for electronic and bio-sensing applications. Hence a better knowledge of the properties of the hybrid particles and the synthesis in which they are formed is mandatory.

Many groups have demonstrated well working syntheses, that produce evenly sized silica shells around single QDs, and leave the QD intact. [70–76] Acebron[76] et al., Gerion et al [72] and Aubert et al.[70], like other authors, demonstrate that for successful syntheses of silica encapsulation of CdSe/CdS QDs, the quantum yield can be preserved or in some cases even improved. Additionally, the QDs show a very high and stable QY under UV illumination over weeks or even month, rendering them a magnificent probe for long term cell observation. However they, like other groups[73, 74], find

a small redshift (of the order of magnitude of 10 nm) of the PL signal after encapsulation which has yet to be explained.

The effect of a silica shell on a colloidal QD is previously predominantly an-

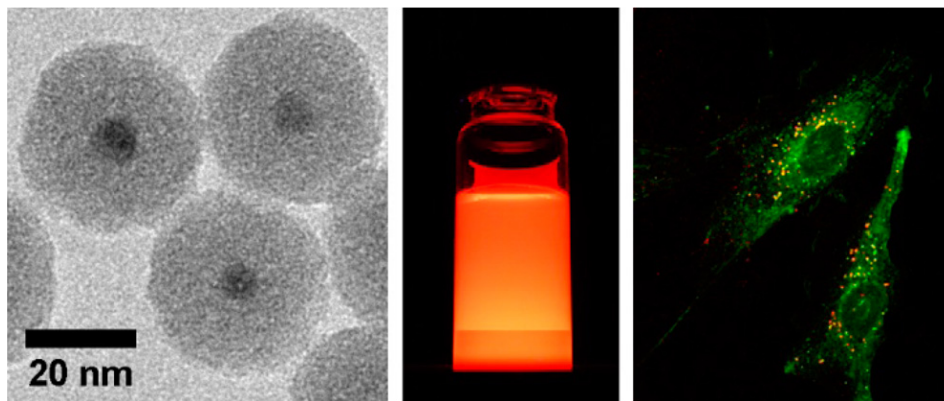


Figure 49: left to right: TEM of silica coated QDs, luminescence of a bottle of QDs under UV irradiation, and application: cells marked with differently colored silica covered QDs under UV lighting, taken from [70] The QDs shown are produced by our cooperation partners and are comparable to those used for this work.

alyzed by TEM, absorption and PL. However TEM only yields information on shell thickness, homogeneity of coverage, possible agglomerations (number of enclosed QDs), and an overall impression on the presence on generally intact QDs. Whereas smaller, more intricate changes in the structure of the QD, e.g. a change in bond length or a rearrangement on the surface, or even the formation of an interface are very hard (and time consuming) to determine by TEM. Even in high resolution TEM those small changes of the surface at the atomic length scale are hard to resolve, rendering the observation of a rearrangement nearly impossible.

In contrast to this, in PL and absorption measurements, effects of changes on the electronic structure of the QD can be observed. It is generally used assuming that when the PL or absorption of a sample goes down, the synthesis of the silica shell has destroyed the samples and hence was not successful. Those methods, especially PL, mostly address the properties of the optically active transitions with a high occupation probability (apart from experiments with very high excitation densities). In the case of the CdSe/CdS core-shell QDs, the charge carriers have a high overlap of their respective wavefunctions in the CdSe core, so PL experiments result in information on the core. Thus they only peripherally provide information on the effect of silica capping, because the core does not have a direct interface with the silica (outer) shell and hence should show only a weak dependence on the interaction of the silica. A possible interface between

silica and QD would form at of the outermost part of the QD, between the CdS shell and silica shell. On the one hand, this presents an advantage for the QY of the QD, as the core is protected from influences on the surface of the QD. On the other hand, this complicates the analysis of the influence of the silica shell, which potentially, with higher knowledge on the interaction, could even improve the QD's properties.

In contrast to this, in absorption the absorption levels of both CdSe core and the CdS shell should be visible. However the problem is the overlapping of the CdS shell absorption lines with higher energetic broad features of the CdSe cores in same the energetic region. This causes the CdS shell related absorption lines to mostly vanish within the absorption band of close lying levels of the CdSe core and makes the assignment and interpretation extremely complex and thus rarely done.

In conclusion, both methods are mainly used to monitor changes in the main optical transition, the lowest energy level on the CdSe core and are used to confirm the QD is still intact, through demonstrating it has a comparative quantum yield and emission wavelength after the silica encapsulation compared to before. Since the QDs in the analyzed samples always have a size distribution, the emission signal is broadened accordingly, and hence smaller changes induced by the silica capping might not be visible anyway.

As a further method of investigation, ^1H NMR spectroscopy, has been applied by Acebron et al [76]. they follow which chemical species interact with the organic ligands that cover the QD initially and find that under the conditions applied the ligands stay linked to the QDs even after the encapsulation. Therewith they demonstrate that the silica forms on top of a ligand shell that remains on the QD. However this method cannot provide direct microstructural information on the QD's surface. Additionally, the ligands used in the experiment are strongly bound to the surface (see Sec. 12.2), which means the experiment can lead to different results when different conditions are used.

At the same time, the synthesis of the silica shell in the reverse micelle solution is often regarded as a black box. Samples are analyzed before and after the encapsulation, but the process in between is mostly guess-work between those two points, which makes it an interesting subject for in situ analysis for a more detailed investigation. not only indication, but real evidence of the changes the undergo.

As Raman spectroscopy provides structural details that can potentially unveil the interaction between the QD and the changing surrounding. It has been shown to reveal details on the interface in core-shell QDs [43] as well as possible influences of the surface on the QD[91, 95, 124, 145] (see also Section 8.2). However, it has rarely been applied to the silica encapsulation before, only Ethiraj et al.[146] used Raman spectroscopy to prove that the QDs remain intact after silica encapsulation. Additionally, they compare their silica encapsulated QDs with pure silica samples and find similar fea-

tures in the spectra. However the silica features consist of broad features in the low frequency region ($250\text{-}500\text{ cm}^{-1}$) and more discrete signals at higher energies (around 1500 cm^{-1}), which probably originate from molecule vibrations while the broad low energy feature should stem from collective vibrations of the amorphous structure of the silica. However, the Raman spectra are mainly used to evidence the presents of both structures and are not analyzed in much detail.

This leaves room for a more detailed Raman spectroscopy-based study of silica-QD compound particles. Here, due to the long duration of the synthesis, and the sharp and intense Raman signal of the CdSe/CdS QDs, even the in situ observation of the synthesis is possible. Which should provide valuable information on the process of the silica formation on the QD.

12.2 Synthesis of silica particles and the synthesis reaction mechanism in the reverse micelle microemulsion

The use of silica for the encapsulation of QDs for biological or medical applications provides many advantages, as it is a comparatively well known biocompatible material. One very important aspect is that it provides the water solubility to the QD, which is the basis for any biological application. The synthesis of nano sized spherical silica structures is usually performed in a water-in-oil solution. Using a silica precursor, often TEOS, the synthesis takes place under the addition of ammonia and a surfactant. Together with the surfactant, the water forms micelles in the oily solution. Those micelles are used as nano-reactors for silica, as well as for a wide variety of other nanoparticles. With the addition of ammonia the synthesis is started, as it enables the TEOS molecules (or other alkoxy silane precursor) to be hydrolyzed and available for reaction. Such an amorphous silica structure can form from within the water micelles from condensation of the hydrolyzed silica precursor (classical sol-gel reaction).[75, 147] However the actual mechanism for the silica encapsulation of the hydrophobic nanocrystals in the microemulsion is not completely understood. It is however often assumed, that the previously hydrophobic nanocrystals, initially in the oily phase, can migrate into the water micelles, enabled by an exchange of the organic ligands for hydrolyzed silica monomers and/or surfactant molecules. [73, 74] This process is schematically depicted in Fig. 50.

Osseo-Asara and Arrigada[148] find that the evolution of average size of a silica particle formed in a microemulsion can be described by first order kinetics with a growth rate k . This rate k can, under the assumption that the change in concentration of silica precursor is directly gives with the amount of newly formed silica, be described as $k = d[\text{TEOS}]/dt = d[\text{SiO}_2]/dt$.

Using TEOS as a precursor, the silica builds spherical particles, which means that when analyzing the particle size, it can be assumed that the TEOS is converted to a spherical volume. The speed of TEOS conversion is deter-

mined by the relation water to surfactant, which Osseo-Asara and Arrigada[148] studied in detail and find that a higher surfactant concentration enables faster growth. Within the first 30 hours of the experiment the size distribution is represented well by the description based on the amount of hydrolyzed TEOS, but afterwards another growth mechanism might be at work. For instance after a certain point, the statistics of a silica particle even getting in contact TEOS molecule must play a role. However, for a benign synthesis the evolution of average spherical particle size $\langle d \rangle$ over time t thus can be described with the function $\langle d \rangle = (1 - e^{-kt})^{1/3} \cdot d_{final}$, where k is the TEOS hydrolyzation rate and d_{final} is the diameter of the particle at the end of the described growth step (not the converged diameter when the growth has saturated naturally). This just reflects the fact that for the growth of a 3 dimensional structure, the TEOS converted to silica needs a fill a volume and hence the TEOS consumption for the growth goes by the power of 3 of the particle radius.

Looking at the synthesis in a more general way, it becomes clear the solu-

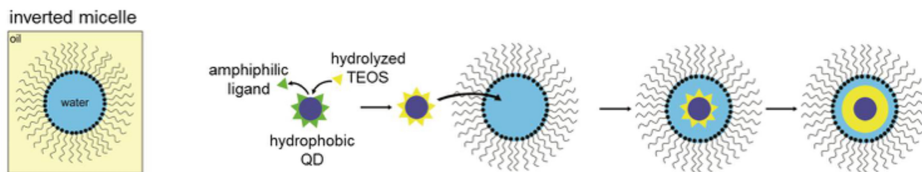


Figure 50: left to right: Model of the so-called “inverted micelle”: A micelle of hydrophilic liquid in hydrophobic liquid (water in oil, instead of the usual oil in water), kept stable by a shell of ligands. Schematic of the growth mechanism of a silica (hydrophilic) shell around colloidal hydrophobic QDs: The synthesis starts with a QD covered in amphiphilic ligands. Once the silica precursor molecules, the TEOS, hydrolyzes and silica can be formed. This can be either directly on the surface of the QD, thereby removing the ligands or on top of the ligand shell (not shown). The silica forms a hydrophilic shell around the QD, that favors solution in water. Hence QD transfers to water micelles, which provided in the synthesis solution, where the silica shell proceeds to grow until all hydrolyzed TEOS is used up. image taken from Tangi Aubert, private communication.

bility plays an important role as the CdS/CdS QDs that are to be capped are hydrophobic, while the silica that will encapsulate them in the end is hydrophilic. Hence during the synthesis the solubility changes and the QD must travel from one solvent to another. Consequently the synthesis must take place in a microemulsion, containing both water (or a different hydrophilic solvent for the silica) and a hydrophobic solvent like toluene or cyclohexane (for the QD covered with amphiphilic ligands; often TOPO, TOP or oleic acids). The emulsion is kept stable by a nonionic surfactant, in our

case Brij, a polyalkylene glycol ether, that is widely commercially available. This microemulsion is schematically shown in Fig.50, where a water micelle is shown in cyclohexane solution surrounded by surfactant molecules. During the course of the synthesis, the QD which were previously surrounded by it's ligands and diluted in cyclohexane, will be covered by the first of silica have to travel into the water micelle because of solubility.

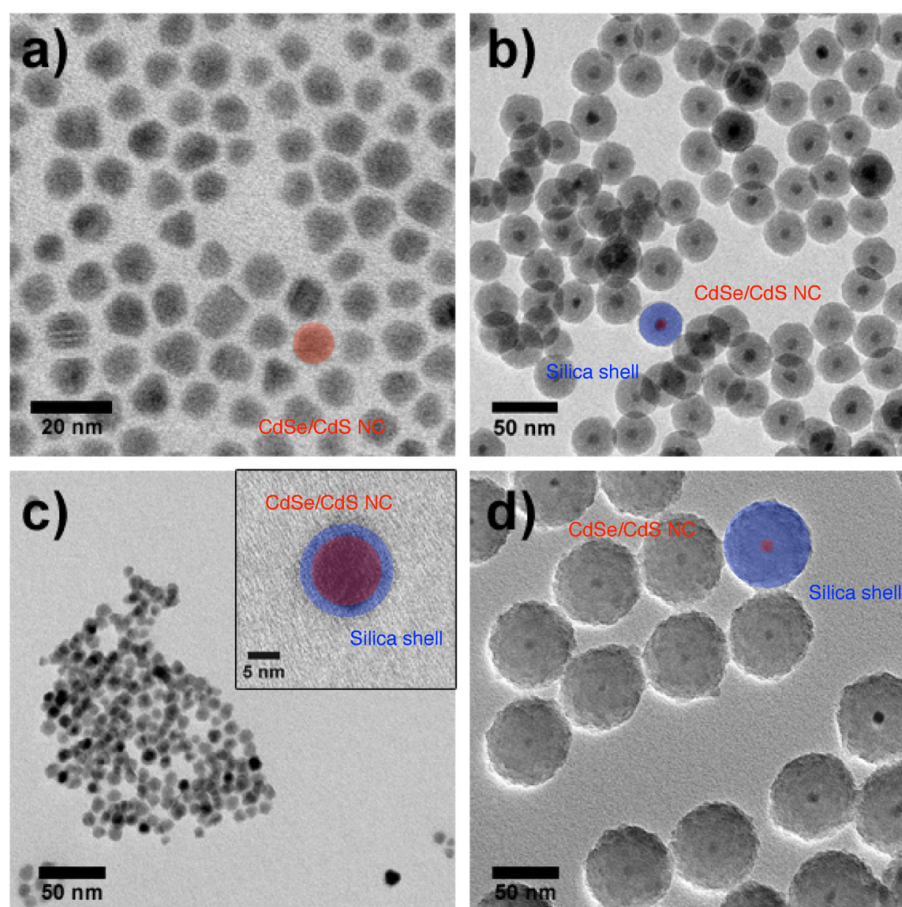


Figure 51: TEM measurements of CdSe/CdS QDs before (a) and after silica encapsulation (b-c), with increasing silica shell thickness c-b-d. For better visibility, the QD is highlighted in red, the silica shell in blue. Figure after Aubert et al.[70]

The exact mechanism of silica incorporation is debated in the literature currently. One possibility is that the ligands on the Qd surface are replaced by hydrolyzed TEOs molecules which allows the QD to travel into the water micelle (Fig.50).[73, 74] Others believe that the ligands on the QD are exchanged by surfactant molecules to enable the travel into the micelle before

the hydrolyzed TEOS attaches to the surface and the growth of the shell starts.[73] Darbandi et al. base this assumption on TEM measurements, where no surfactant filled gap found between silica and QD. Koole et al conclude the direct interaction of silica and the QD surface from time-resolved PL measurements following the different stages of the synthesis. This is opposed by thiol bound ligands, have been shown to remain on the QD surface after silica encapsulation, as reported by Acebron et al.[76] (bases on NMR measurements). Those ligands however have been shown to be more tightly bound to the QD surface than oleic acid for instance, which have demonstrated to be easily removable from the surface by Hassinen et al.[149]. For further information on the surface chemistry of the QDs used in this work, see Sec. 7 and Drjivers et al. [78].

Since the bond between QD surface and attached ligand can be this diverse, it is out of outmost importance to analyze the surface chemistry and the different outcomes of the silica encapsulation synthesis in more detail. This can result in several different mechanisms of coverage and surface functionalization, the understanding of which could be a key to improving the quality of the final capped QD. Eventually varying the QD's ligands, microemulsion surfactant or pH conditions, would certainly be of interest for the design of an optimized synthesis towards the production of materials with greater optical properties.

Until now, very few of these theories have been supported by actual measurements to determine the exact surface reaction on the QD surface. Hence the question is left open if the silica shell is formed directly on the QD surface, or on top of or incorporating the ligand shell around the QD. Between those cases, the intensity of interaction between the two materials would surely be very different and should influence the properties of the QD inside. Consequently, we analyze the silica encapsulation of CdSe/CdS QDs in order to find evidence regarding the nature of interaction between silica and QD in the following Section.

12.3 The *in situ* Raman setup and synthesis of silica shell on CdSe/CdS QDs

In order to realize *in situ* Raman measurements during a silica encapsulation reaction, the reaction is performed in a cuvette placed in the macro setup (shown in Sec. 6.1). The cuvette must be stirred continuously during the whole process by a magnetic stirrer to ensure a constant temperature in the whole vessel due to possible laser induced heating. The cuvette used (Torlabs) has a volume of 2.5 mL, to facilitate sufficient mixing and optimal for transmission of light in the visible range.

Since the reaction takes place in the course of two to three days, the system needs to be stable and CCD cooling needs to be ensured. The stability of

the solution is temperature sensitive and best kept constant at 20°C, as at temperatures above 32°C the microemulsion separates irreversibly. This is caused by the temperature instability of Brij. We found that some stirrers develop heat after operating for a few hours, so as a result the cuvette is positioned above the stirrer separated with ca. 2 cm styrofoam and is cooled with cooling fan additionally. To keep laser induced heating low, the laser power was kept below 10mW. Intensity fluctuations due to small changes in laser power can be corrected by normalizing to the solvent intensity. For the encapsulation, wurtzite CdSe/CdS QDs are synthesized with the *flash* procedure as published by Cirillo et al. [69] (Sec. 7.2.1). These QDs have been shown to retain good luminescent properties and high stability after encapsulation by Aubert et al. [70] (see also Sec. 7.3 and Sec. 12) We employ a reaction based on this synthesis, only the solvent is substituted with cyclohexane for a better separation of the Raman signal of solvent and QDs.

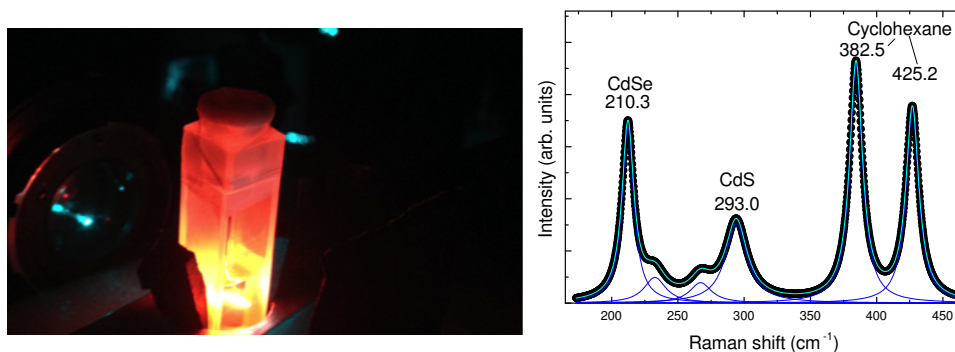


Figure 52: Left: photo of a QD solution post silica encapsulation within the Raman setup, illuminated with the Raman laser. Right: Raman spectrum of CdSe/CdS QDs in cyclohexane solution with the phonon modes of CdSe and CdS clearly visible, as well as two modes originating from the solvent that remain stationary over the whole synthesis.

First the prepared QDs, which are in solution with cyclohexane, are mixed with an additional 1ml of cyclohexane with 0.32 ml Brij (Polyethylene glycol hexadecyl ether) and stirred for at least 5 minutes. Then, 50 μ L water and 5 μ L ammonia (NH_4OH) are added and after 1 hour of stirring, the solution is ready for silica precursor injection to start the synthesis. This step is crucial to ensure the formation of a microemulsion needed for the reaction, as an isotropic growth of silica shells, which each enclose one QD only, is not possible otherwise. We vary the TEOS amount to compare different reaction speeds and final silica shell thicknesses during and after the experiment. The TEOS amounts used in the three separate synthesis are listed in Tab.3 and are given in the TEOS to QDs molar ratio in the

following to give a more universal value that is independent of the QD concentration in the initial mixture. The QD concentration of the QD solution is determined based on their absorbance in toluene under the use of intrinsic absorption coefficients, calculated with Maxwell-Garnett effective medium theory in dependence of the CdSe/CdS volume ratio.

For the *in situ* measurement, the TEOS injection marks the beginning of

Sample	TEOS-volume (μL)	TEOS/QD molar ratio	final silica thickness (after 72h) (nm)
QD A-1	13	$2.86 \cdot 10^5$	26.7 ± 1.5
QD A-2	25	$5.51 \cdot 10^5$	33.4 ± 1.7
QD A-3	50	$7.71 \cdot 10^5$	35.8 ± 1.5

Table 3: Varied TEOS amounts used in the *in situ* Raman observation for three different synthesis' presented in Sec. 12

the reaction and thus has to be conducted with the cuvette in place inside the Raman setup. Measurements need to be started simultaneously and be repeated in defined intervals of time (with Labspec), and resulting in the time axis for the *in situ* observations. We used an integration time of 180s and repeated the measurements every 10 minutes for the duration of the whole synthesis of up to tree day. Since changes in the Raman spectra have saturated well before 24 h, in some cases the observation was stopped after 48 h. The resulting Raman spectra are subsequently analyzed and the different phonon modes are fitted with Lorentzian functions, as shown in Fig.52, to extract precise positions and integrated intensities of each mode. To correlate the findings from Raman spectroscopy with a silica shell thickness, in separate syntheses the thickness is analyzed by TEM after defined intervals of time. This is done by taking aliquots from the reacting solution and subsequently stopping the shell growth by removing the remaining TEOS molecules by centrifugation.

Name	CdSe core (nm)	total (nm)	CdS shell thickness (nm)	surface area / volume of CdS shell(1/nm)
QD A	4	7.4	1.7	2.8
QD B	3.6	9.1	2.8	0.8

Table 4: Different QD geometries, that where observed during silica encapsulation with *in situ* Raman with diverging results presented in Sec. 12.8

Additionally to the silica encapsulation synthesis with varied silica precursor amount on the same QD, we have conducted a similar encapsulation on a QD with a different geometry (see Tab. 4) to be able to analyze how

the effect in the Raman spectrum is influenced by the surface to volume ratio of the QD. At the same time this QD B has a less strained CdS shell, and hence the initial phonon frequency of the QDs diverge.

These experiments are shown and discussed in Sec. 12, giving an interesting insight into the silica encapsulation reaction and the interaction with the enclosed QD.

12.4 Raman analysis of the silica encapsulation of CdSe/CdS QDs

In the previous Sections we established that there is an interest to find out about the nature and strength of interaction between the QD and the silica shell in such a silica encapsulated compound and described the experimental setup and synthesis condition to be used in the *in situ* Raman analysis of the encapsulation process.

The Raman spectra of pure and silica encapsulated CdSe/CdS QDs are shown in Fig. 53 left. The fact that the Raman signal of the QD is still present after the shell addition, demonstrates that the crystal remains intact after the reaction. The frequency of the CdS phonon mode of the shell, however, appears shifted compared to the uncovered QD. The FWHM of this mode is slightly reduced. Generally, in such a CdSe/CdS core-shell QD, the frequency of the phonon modes is mainly influenced by the strain caused by the lattice mismatch between core and shell. Within the QD, the CdSe core and CdS shell are under compressive and tensile strain, respectively. This results in shifted Raman frequencies compared to the undisturbed bulk phonon mode towards blue for compressive strain, and red for tensile strain. As a first investigation of the influence of the silica shell thickness, the re-

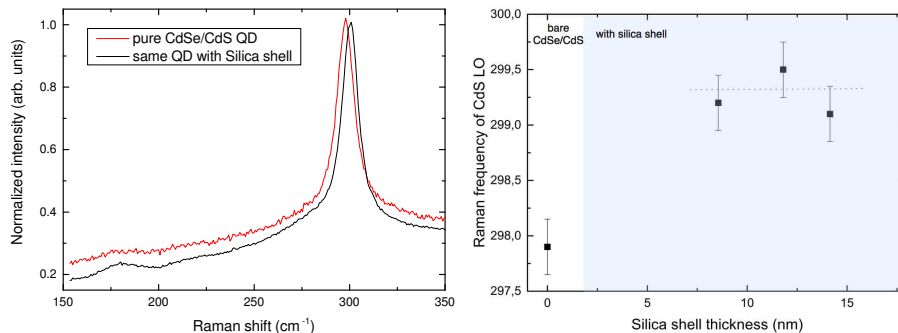


Figure 53: Left: First silica experiment: Raman spectra of one QD, pure and with a thick silica shell. The CdSe core is barely visible, but the CdS shell shows a shift towards higher frequencies and a decreased halfwidth. Right: Raman frequencies of the CdS shell of a pure QD and after coverage with a differently thick silica shell. Within scattering, the frequencies after capping are independent of the shell thickness.

sulting shell phonon mode is displayed in Fig. 53 right for one exemplary QD, pure and covered with different silica shell thicknesses. For this QD, the CdSe core Raman frequency doesn't change upon silica shell addition. For all silica shell thicknesses shown, the shift in Raman frequency compared to the uncovered QD is the same, which evidences that the shift is independent of shell thickness above 8 nm. Hence, to find the dependence of the shift from the silica shell, the investigation needs to start at far lower thicknesses, as the shift has saturated already above 8 nm thickness.

Nevertheless, the direction of the shift is the same direction for all examined samples. The CdS shell phonon mode always shifts towards the bulk frequency, starting an initial red shifted CdS shell phonon frequency due to tensile strain in the QD. This direction in combination with the small decrease in halfwidth of the phonon mode, indicates a reduction of strain combined (shift) with an improvement of the long range order of the crystal (low halfwidth of Raman mode). Thus a reduction of strain due to defect induced relaxation is unlikely. However the origin of the shift in Raman frequency will be discussed in more detail in Sec.12.6, after the analysis of the dynamics in Sec.12.5.

The total difference between initial and final frequency depends on the geometry of the initial QD. A QD with a thin CdS shell is under heavy tensile strain and thus starts at with lower initial phonon frequency and in tendency shows a higher change when a silica shell is added. Additionally it will become clearer in the following chapter that a dependence of surface area compared volume of the shell is also likely to have an impact, as we demonstrate that, under our experimental conditions, the shift is caused by interaction with the surface(see Sec.12.6).

In order to find out at which state of the synthesis the shift occurs, we monitor the formation of the silica shell in situ during the synthesis with Raman spectra every 10 minutes with an accumulation time 180 s. A typical spectrum of the QD microemulsion, that is used for the synthesis, is shown in Fig. 54a. The peaks of main interest, the CdSe core and the CdS shell phonon, are visible at 210 cm^{-1} and 293 cm^{-1} for this QD (QD A). Additionally, the solvent Cyclohexane has two peaks at 383 cm^{-1} and 425 cm^{-1} , which can be used for reference as the solvent is unaffected by the reaction, hence the position and intensity remain constant and are used for normalization. All spectra are analyzed and fitted with Loretzian functions, as shown in Fig.54a with peak-o-mat and in the following, the LO-peak positions, FWHM and intensities (peak areas) are collected from the fits are used for analysis in the following.

In Fig.54 a and b, the evolution of Raman frequencies of the CdSe core and CdS shell (of QD A) is displayed during the synthesis of a silica shell over synthesis time. The time 0 corresponds to the injection of silica precursor, the start of the synthesis. While the CdSe signal of the core only shifts towards a higher frequency by approximately 0.5 cm^{-1} , the CdS shell fre-

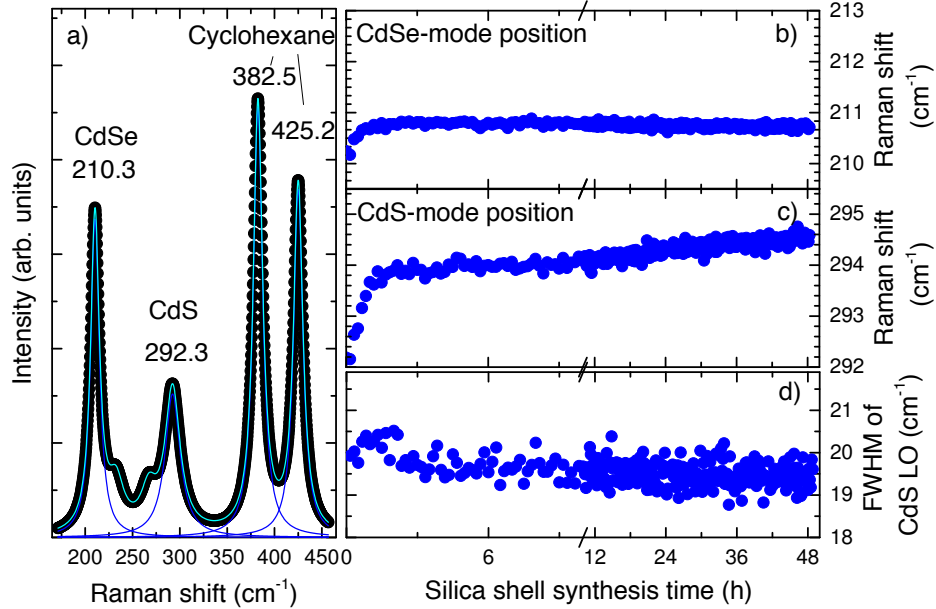


Figure 54: a) Raman spectra of CdSe/CdS QDs in cyclohexane solution. Peaks from the CdSe core and the CdS shell can be seen at 210 cm^{-1} and 292 cm^{-1} , respectively. The solvent cyclohexane has peaks at 382 and 425 cm^{-1} . Position of the CdSe b) and CdS c) LO-like modes depending on time passed during silica synthesis. Time =0 corresponds to time of TEOS precursor injection. Break in time axis to highlight “early” hours of the experiment, d) FWHM of the CdS shell LO fit during the course of synthesis. [150]

quency increases by as much as 2.2 cm^{-1} . Additionally, the FWHM of the CdS shell Raman mode reduces from 20.5 cm^{-1} to 19.5 cm^{-1} , about 1 cm^{-1} in total, which has already been observed in the ex situ measurement. Hence the in situ measurement reproduces results from the comparison between pure and final silica covered QD, but also reveals that this shift only takes place in a very early stage of the synthesis. While the final silica thickness is reached after several days, the Raman frequency shift saturates already after 2 hours in this synthesis. This indicates that the shift is not primarily a function of the silica shell thickness, but of the formation of the very first silica layers. Considering that silica is an amorphous material, the prospect that it doesn't cause an epitaxial strain on the QD makes sense, since it would increase for increasing thicknesses far beyond a few nm. In the following, we examine the dynamics of the synthesis in more detail. For this experiment, we vary the concentration of the silica precursor in order to vary the speed of the silica formation. This should lead to direct

information on the dynamics of the evolution of the Raman signal and the synthesis. Additionally we compare the effects of the silica shell on two QDs with different geometries to see if this influence the extend of influence of the silica on the QD.

12.5 Dynamics of the silica encapsulation reaction analyzed by *in situ* Raman and TEM

Since in Sec. 12.4 it was established that the shift in CdS phonon mode upon silica capping develops at low silica shell thicknesses and saturates fast. These finding shall now be connected with the silica shell thickness' function of time during the synthesis. The growth speed is varied to find the relation between the shift in Raman frequency and the speed of the silica growth.

Thus to further investigate the dynamics of the shift, we have designed the following experiment: the same QD (QD A) is encapsulated in three separate synthesis under the same conditions, same water, Ammonia and surfactant concentration, apart from silica precursor concentration. For a detailed list of used amount of each chemical see Section 12.3. Three different TEOS concentrations, $2.86 \cdot 10^5$, $5.51 \cdot 10^5$ and $7.71 \cdot 10^5$ TEOS to QD molar ratio, are employed. These three reactions are monitored by *in situ* Raman and in a separate experiment under the same conditions, the evolution of average particle size is analyzed by TEM. The TEM analysis is realized by taking aliquots from the reacting solution after defined periods of synthesis time. Those aliquots are subsequently cleaned from TEOS by centrifugation to stop the reaction and then analyzed by TEM. A small selection of theses TEM measurements is shown Fig. 55. The QDs in their developing silica shell for all three syntheses are displayed for two different synthesis times; after 2 hours of synthesis and after 72 hours, when the experiment was stopped. With increasing TEOS amount in the synthesis, both the final silica thickness as well as the growth speed increases.

The the development of the average particle size over time gained from these measurements is shown in Fig.56 for the three syntheses. The employed TEOS concentrations of $1.73 \cdot 10^3 \text{ nm}^{-2}$, $3.33 \cdot 10^3 \text{ nm}^{-2}$ and $4.66 \cdot 10^3 \text{ nm}^{-2}$ result in different final silica shell thickness after 72 hours, as well as diverging speed of shell growth. In general, the higher the TEOS concentration, the faster the speed of silica growth and the higher the final shell thickness. As mentioned in Section 12.2 the growth of pure silica particles in water-in-oil microemulsion can be well describe by a simple function. It should be noted that the shell thickness after 72 hours of growth still hasn't saturated and would proceed if the reaction isn't stopped by washing the particles and thus we can assume, the growth does not go beyond the TEOS hydrolyzation rate limited regime as described in Section 12.2. However, for the description of the silica encapsulation, the non-zero initial silica particle size has to

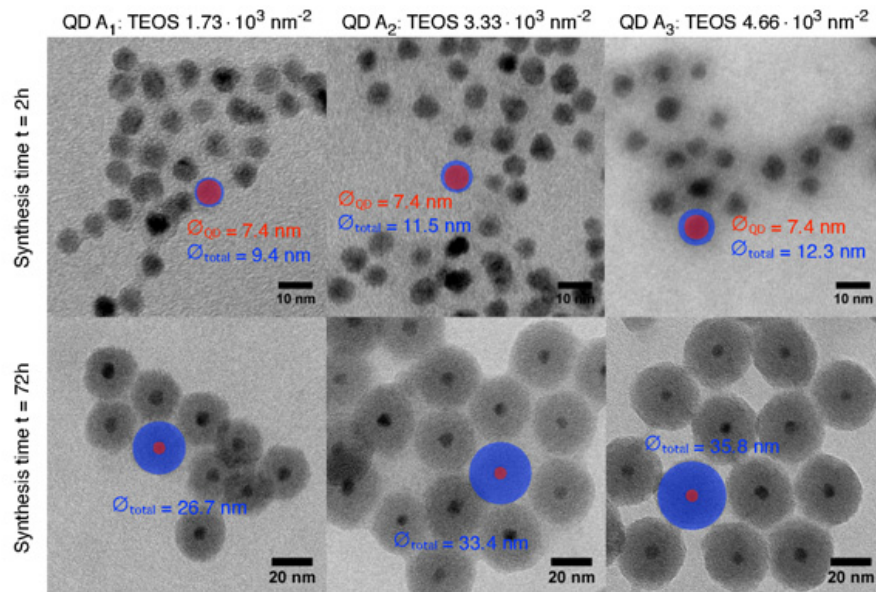


Figure 55: TEM-analysis as a function of the synthesis time for different TEOS amounts in TEOS molecules per QD surface area (QD A₁ $1.73 \cdot 10^3 \text{ nm}^{-2}$, QD A₂ $3.33 \cdot 10^3 \text{ nm}^{-2}$ and QD A₃ $4.66 \cdot 10^3 \text{ nm}^{-2}$), in TEOS to QD molar ratio QD A₁ $2.86 \cdot 10^5$, QD A₂ $5.51 \cdot 10^5$ and QD A₃ $7.71 \cdot 10^5$

be taken into account, since the minimal particle size here is the QD size. To account for the presence of initial CdSe/CdS seeds, which will influence the initial growth rate, introduced a time offset to their equation. Looking at the data, we find that the formula gives a good fit when approximately the first 5 hours of experiment are excluded. This means that within those first 5 hours the growth mode differs from that of pure silica particles. After the synthesis of more than 2 nm of silica, it becomes the same as for pure silica particles.

During those first few hours of the experiment, the first layers of silica form on the surface of the QD. This heterogeneous nucleation is slower than the growth later on, as can be seen in Fig.56a. Because this coincides with the time frame of the change in Raman frequency, it is necessary to investigate this region in as much detail as possible. To quantize the nucleation speed, we fit the average silica shell thickness approximating with a linear fit. It may be noted that for the lowest TEOS concentration, we find no trace of the silica in TEM after 1 hours, so for this synthesis the point 0,0 is removed from this fit. This could be an effect of low accuracy in the determination of silica thickness by TEM, which is especially high for low thicknesses (resolution, contrast), or a very slow start of nucleation due to the low concentration of TEOS. The linear fit of the average silica shell

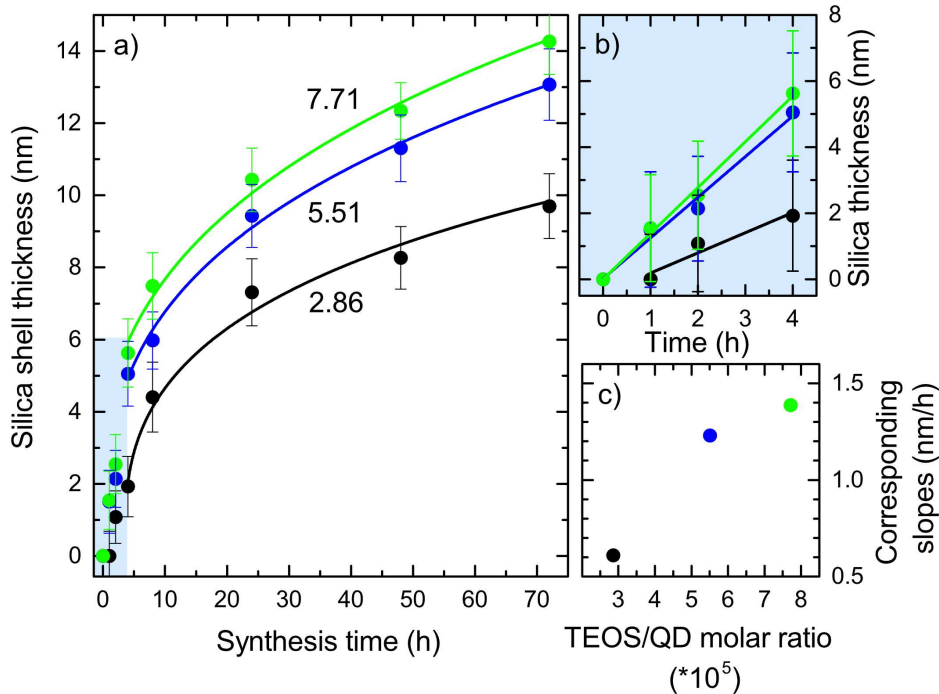


Figure 56: a) silica shell thickness as determined by TEM-analysis as a function of the synthesis time for different TEOS amounts ($2.86 \cdot 10^5$, $5.51 \cdot 10^5$ and $7.71 \cdot 10^5$ TEOS to QD molar ratio in black, blue and green respectively) The final size, as well as the speed of the reaction increases with higher TEOS concentration, Inset in a): TEM of final silica shelled QD, b) linear fit of 0-5 hours (formation of the first silica on the QD) of data in a), c) slopes resulting in b) over TEOS concentration. part of this work and from [150]

thickness within the first 5 hours is shown in Fig. 56b). To connect this dependence with the synthesis condition, the slopes resulting from the fits are shown in 56c) in dependence of the corresponding TEOS concentration in the synthesis. This clearly shows a linear correlation between the speed of silica growth in this starting phase and the TEOS concentration in the reaction. Fig. 57 shows the CdS Raman frequencies during the course of the three syntheses. For all syntheses, the change in phonon frequency saturates below the duration of 5 hours. 90% of the final shift has been reached after 4.4 hours, 3 hours, and 1.8 hours in order of decreasing TEOS concentration. Already this indicates a correlation similar to the linear dependence of the nucleation speed on the TEOS concentration. The final Raman frequency is the same for all syntheses, independent of final silica shell thickness or

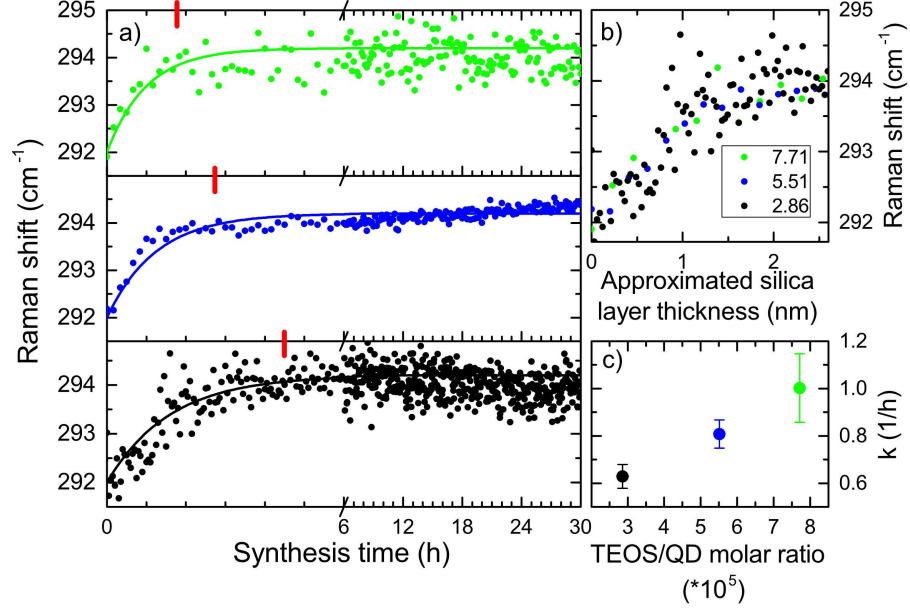


Figure 57: Raman shift of the CdS mode as a function of the synthesis time for different TEOS amounts per QD surface ($2.86 \cdot 10^5$, $5.51 \cdot 10^5$ and $7.71 \cdot 10^5$ TEOS to QD molar ratio in black, blue and green respectively). The final shift remains the same between the different conditions, while the speed of the shift increases with higher TEOS concentration. The red ticks mark the time where 90% of the final shift is reached. part of this work and from [150]

the speed of heterogeneous nucleation. This essentially reflects our findings from ex situ measurements as mentioned in Section 12.2.

To analyze dynamics of the shift, we find that the Raman shift can be well described using $A_f - \Delta A e^{-kt}$, where A_f is the final Raman frequency reached during synthesis, ΔA is the total change in Raman signal over t (time) with the exponential parameter k that represents the rate of saturation. The shift of the Raman frequencies together with the fits are shown in Fig. 57a. The growth rates k resulting from this fits, are displayed in Fig. 57c in dependence of the TEOS concentration in the synthesis. Again, we find an approximately linear dependency on the TEOS concentration. This is also supported by Fig. 57b, which shows the Raman shift in dependence of the approximated silica shell thickness, which was calculated with the linear fits to the TEM determined sizes. It demonstrates, that the shift in phonon frequency is actually the same for all synthesis, when the shift is analyzed in dependence of the shell thickness instead of synthesis time and shows this shift is fundamental.

Additionally since the speed of silica nucleation on the QD surface is linearly

dependent on the silica precursor concentration, as discussed above, this is a new method to monitor the nucleation right during the synthesis, without the necessity of stopping the reaction or taking aliquots. Thus monitoring the Raman signal enables the silica shell growth process to be studied in more detail and optimized more rapidly than conventional spectroscopic techniques or TEM allow. This method provides a new approach to analyze the reaction mechanism of the nucleation of silica on the QD surface and how it is influenced by the water-to-surfactant ratio, TEOS/QD surface relation, temperature or Ammonia concentration. As before mentioned the influence of differently strong bound ligands on the surface of the initial QD should have a strong influence on the synthesis.

12.6 Origin of the change in Raman frequency during silica synthesis

In the previous Sections, the change in Raman frequency of the CdS LO phonon mode during the encapsulation of a CdSe/CdS QD with silica has been discussed, establishing that the shift is independent of the shell thickness when the coverage exceeds 2 nm and correlating the dynamics of the shift in Raman frequency with the nucleation of silica on the surface. If the silica would be interacting with remaining organic ligands only, it would not affect the structure of the QD and thus could not explain the observed changes in the Raman spectrum. Thus, the extent of the effect of the silica on the Raman signal of the CdS shell implies a close interaction between the two materials. The reduction in halfwidth of the phonon line excludes massive structural defects caused by the reaction. This leaves the question open, what the origin this shift actually is. In general, shifts in Raman frequency mean that the vibrational properties of the material have changed. This can happen due to a change in bond length, bond strength and/or geometry, for instance. All of those change the conditions for a lattice vibration and thus the phonon energy.

Scenarios with a complete exchange of bond partners in the whole sample are unlikely in many experiments, hence shifts or deviations from reference samples in Raman frequency are often discussed in the context of strain. This can, for example, be epitaxial strain, that occurs when two materials with different crystal lattices are grown on top of each other. In order to form a bond, the unit cells at the interface need to deform to make a fit. For the material with the smaller lattice constant this means it must stretch, while the larger lattice constant is compressed. This puts the two materials under tensile and compressive strain, respectively. Thinking of the lattice vibration, this can be compared to a stressed system of springs (elastic constant model). Compressive stress changes the eigenfrequency of the spring towards higher energy, tensile stress leads to lower eigenfrequencies. The

same is valid for the phonon energies measured in Raman spectroscopy. To make claims about strain however it is necessary to have a strain-free reference system, for colloidal QD in most cases a bulk reference at a defined temperature would be used. In this context it is also important to think about different temperature expansion coefficients of different materials, as this influences the interplay strongly, depending on the temperature the materials were brought in contact (grown) and the temperature at which the measurement is performed. This temperature dependence is addressed in more detail in Section 9.

Considering the CdSe/CdS QD in silica shell, we are presented with materials that possess very different long-range order. Two materials in the compound form a periodic crystal lattice CdSe and CdS, while silica is an amorphous material, which has a short-range but no long-range order. The atomic structure of silica is shown in Fig. 58. So before the addition of the silica, the QD is strained depending on the correlation between CdSe core and CdS shell, this leads to Raman frequencies that are smaller than for bulk material for the CdS shell, and ones that are larger than in bulk material for the CdSe core. The addition of the amorphous silica shell results in a shift to higher frequencies for both signals at different extents. For the CdSe core, the shift is either very small or for not detectable (depending on the exact geometry of the QD), this would mean a small increase in compressive strain. This is opposed by the shift to higher frequencies for the CdS shell, which shifts the shell closer to CdS bulk configuration. At the same time, the halfwidth of the CdS LO phonon mode decreases and thus indicates an improved ordering in the shell and an improved, overall more bulk-like condition. Since silica is an amorphous material, this shift cannot be because by a lattice mismatch inducing strain. As this silica is formed, it is energetically unfavorable to grow in a way that it applies additional (compressive) strain to the QD and because it is not constrained to crystallize in an ordered lattice, it will arrange in the position with the lowest potential energy. Furthermore since the temperature of the synthesis is the same as for the measurement, thermal expansion can be excluded as a cause of further strain. Additionally to the position of the phonon mode, strain influences the halfwidth of the mode because the distribution of bond length increases when stress is applied. The fact that the halfwidth of the CdS LO phonon mode has a tendency to decrease, suggests that additional epitaxial strain applied to the QD is not the explanation for the shift in phonon frequency, as it would increase the distribution width of bond lengths.

At the same time, atomistic *ab initio* calculations done by Han et al. [124, 125] find that the whole CdSe/CdS QD structure, should be under compressive strain. For the phonon frequencies for both, CdSe core and CdS shell, this would lead to a blue shift compared to the bulk phonon frequency. However, according to their calculation the shell still has a redshifted phonon frequency. The reason for this redshifted signal of the shell is the surface. At

the surface. the symmetry of the crystal is broken; the atoms lack bonding partners. This *surface under-coordination*, according to Han et al., overcompensates the effect of the compressive strain on the phonon frequency and results in a signal that is red shifted compared to the bulk phonon frequency. So the final outcome of phonon energies is coherent with that predicted by the epitaxial strain model. Since this shift of the CdS shell is a pure surface effect, it strongly depends on the ratio between surface area and volume of the shell material. When the surface area is small in comparison to the volume, the influence on the resulting signal becomes negligible. This indicates that at very small surface-to-volume ratios, the phonon frequency should become higher for the CdS shell than for bulk material. This is where the calculation differs from results of our measurements. Even for shells as thick as 15 nm, the phonon frequency doesn't become higher than the bulk frequency. The same is evidenced by other groups based on measurements of dot-in-dot or dot-in-rod structures. This shows that the overall compressive strain in the QD that they predict can't be found in experiments. Even though this points out boundaries that the calculation faces, the findings still point out the high relevance of surface symmetry breaking in a QD and the great effect the surface has on the phonon frequency.

In our experiment, the initially red shifted CdS shell shifts towards bulk frequency during the nucleation of silica on the surface of the QD, as shown in section 12.4 and 12.5. In the comparison between two different QDs, QD A and QD B, we will find an indication that the total shift during the synthesis is in fact surface related, as it depends on the surface area compared to volume of the CdS shell (Section 12.8). All this is evidence that during the synthesis, the surface of the QD is modified by the formation of an interface with the silica. This interface would reduce the surface under-coordination by providing bonding partners to the CdS shell with bond lengths similar to those present in CdS bulk material. This at the same time explains the blue shift of the CdS LO phonon towards the bulk frequency, and elucidates the reduction of the CdS LO phonon's halfwidth. As opposed to additional strain, the reduction in under coordination should decrease the distribution of bond length in the structure and hence reduce the halfwidth in Raman signal.

Although there is no direct evidence on the nature of the bond, that is formed at the interface of the QD and silica, the direction of the shift in Raman frequency points towards a bond similar to those present in bulk material. Generally, QDs are known to have dangling bonds on their surface[151], thus for the formation of covalent bonds with the silica monomers during coverage is possible. Since the reactive species formed during the hydrolysis of TEOS are silanol groups, we assume that a Cd-O-Si bridge is more likely to form with a dangling bond on Cd rather than a Cd-S-Si bond. This would mean that an O binds to a Cd dangling bond, at a site where in bulk there would be a S atom, as shown in Fig.58. Since O and S

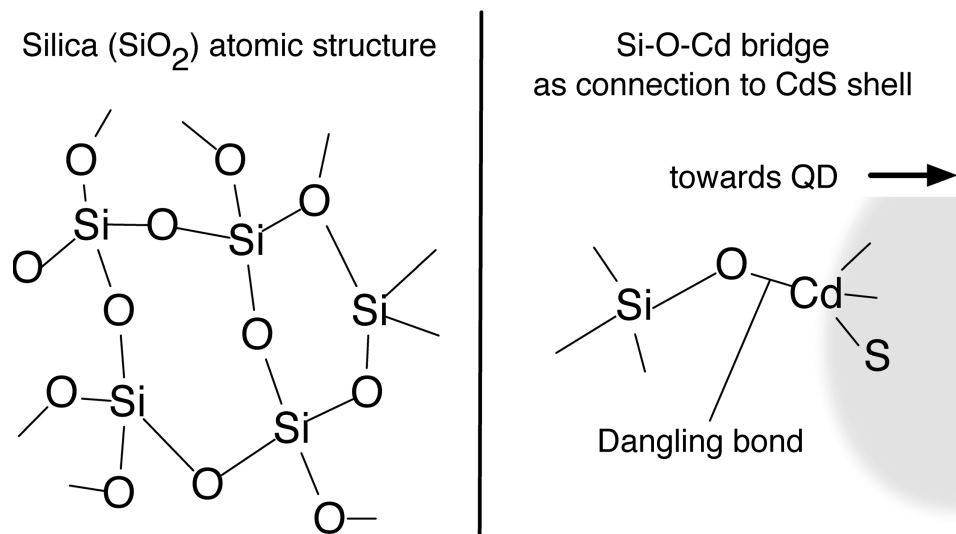


Figure 58: Left: Schematic display of the atomic structure of amorphous silica, Right: Si-O-Cd bridge as possible bound of silica to the QD CdS surface. A Cd dangling bond at the surface is bound to a O atom, which has Si as second bonding partner and forms a connection to the silica.

are in the same chemical group, they have a similar electronegativity and so should form similar bonds. Hence this Cd-O-Si bridge would fulfill required condition to be similar to the bond present in the bulk material.

Although such a reaction step has been proposed as part of the encapsulation process before,[73, 74] the *in situ* Raman investigations thus provide a direct observation of this tight interaction for the first time.

In conclusion, the shift of the CdS Raman mode is most likely not caused by external strain induced by the silica shell. Instead, considering the model proposed by Han *et al.*[124, 125], the blue shift can be attributed to a reduction of the surface under-coordination. This is caused by the formation of an interface based on strong, direct interactions between silica and the QD (Cd-O-Si bridge for instance) and is supported by the shift occurring at a very “early” stage of the synthesis. Thus, the strong influence of the silica on the CdS shell demonstrates the close interaction between the two materials, confirming the removal of the ligands during the microemulsion process for the synthesis condition in the work.

Although this step of the encapsulation process was already predicted by other authors [73, 74], the in-situ Raman investigations provide here the first direct observation of this strong interaction and insight in the microstructure of this interface.

12.7 The evolution of the Raman intensity observed during silica encapsulation

An additional aspect to the change in Raman frequency during the silica encapsulation reaction (Section 12.4) is provided by monitoring the Raman intensity of the signal during the synthesis. Fig. 59 displays the Raman intensity (integrated intensity) gained from the Lorentzian fits to the corresponding peaks. The peak areas are normalized to the solvent peaks in order to account for any changes in laser power during the synthesis, which is monitored over the duration of two days. It is important to note that the changes in intensity are due to an increase in amplitude, not halfwidth. This is shown in Fig. 54, where the halfwidth decreases over synthesis time.

In Fig. 59 a) and b) the evolution of the intensity of CdSe and CdS LO

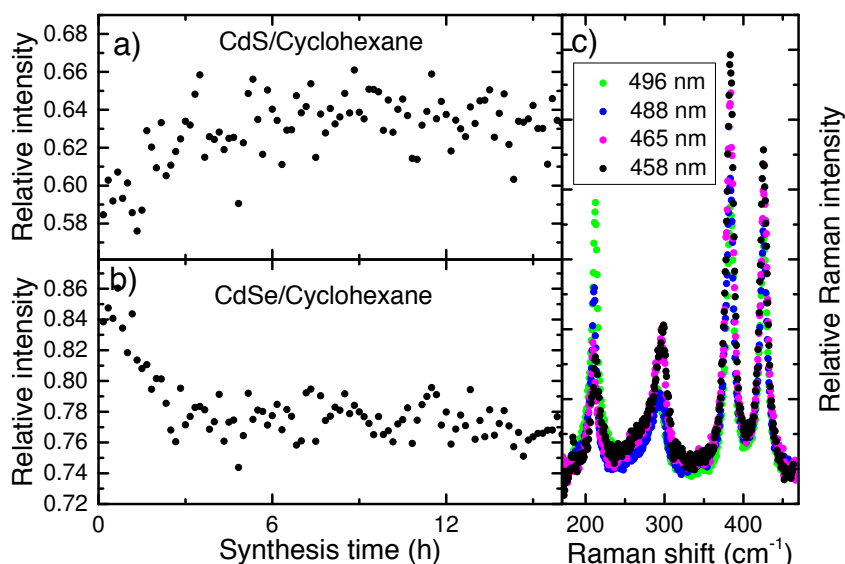


Figure 59: Relative Raman intensities for the CdS (a) and CdSe (b) modes compared to the cyclohexane peak (383 cm^{-1}) depending on synthesis time. The intensity equals the area under the Lorentzian fits of the peaks. (c) Raman spectra of the same QD measured with different laser wavelength, normalized to the intensity of the Cyclohexane peaks according to Trulson *et al.*[152]. For higher excitation energies the intensity of the CdS mode increases, while the CdSe mode decreases. [150]

mode (QD A) during the synthesis with medium TEOS concentration are shown. This is the same synthesis, as in Fig.57 and 56 displayed in blue. Despite the different magnitudes of change in Raman frequency between

CdSe and CdS, the change in intensity is an comparable range. While the intensity of the CdS LO decreases, the intensity of the CdSe LO increases over the course of 6 hours. This change is not at the same time scale as the frequency shift of the signal, indicating a different origin.

Generally, the intensity of a signal in Raman spectroscopy is determined by several factors; apart for experimental influences like laser power or the setup efficiency, the intensity is determined by the strength of electron-phonon coupling, resonance conditions with electronic transitions, and by the strength of the local electric field. Amongst others, these quantities depend on the dielectrical environment. Since in our case we can exclude experimental origin, because we are analyzing the signal change in relation to the stable solvent signal in one continuous experiment, the change in intensity must originate either from a change in resonance condition by a shift of the optical transition energy or a change in electron-phonon coupling. Thinking of the mechanism of the synthesis (Section 12.2), we are faced by a not insignificant change in environment. Before the start of the synthesis, the QDs are in a solution of Cyclohexane with a dielectric constant of $\epsilon \approx 2.0$ [153] and ligands. After the synthesis, the QD is surrounded by silica, which has a higher constant of about $\epsilon \approx 2.4$ [154]. This can have different effects; The screening of the optical field depends, for example, on the local dielectric environment and so do the transition energies between valence- and conduction-band states. Both properties influence the interaction between the QDs and the laser light and thus the intensity of the Raman signals. Unfortunately, the precise effect of dielectric confinement on the optical band gap of QDs is difficult to predict, especially in the case of complex heterostructures.[155–157] To explain the experimental findings, the effect must be such that the states of the CdS shell are shifted closer to resonance with the laser wavelength of 488 nm, while the states of the CdSe core should be shifted further away from resonance.

This can be analyzed by finding in which energetic direction in relation to the laser wavelength the density of states of core and shell increases. Therefore the laser wavelength was varied. The intensities of the Raman modes are normalized to the solvent intensity at the corresponding wavelength after Trulson[152] for comparability. This results in a small resonance profile, as shown in Fig. 59c. With increasing excitation energy the intensity of the CdS LO increases, and the CdSe LO intensity decreases. Hence a shifting of transition energies, induced by a changing dielectric environment, is supported by our experimental observations. The fact that the CdSe mode on the other hand displays the opposite behavior both in resonance Raman measurements (Fig.59c), as well as during synthesis (Fig. 59b), further supports our hypothesis of states shifting towards lower energies. It does however not exclude influences of the local field factor modification by silica encapsulation.

The dielectric confinement has been addressed by many different groups,

especially in theory, because calculated electronic states often differed from experimental values. One reason is the assumption vacuum as a surrounding medium. For instance Franceschetti *et al.*[155] present a very simple model, taking polarization properties into account. This model should help us reveal the tendencies for shifts of electronic transitions for changes in dielectric environment. The smaller the surrounding dielectric constant, the higher the influence of polarization energy and self energy of hole and electron on the QD's electronic energies, effectively increasing the energy gap. In our experiment, the dielectric constant is increased, reducing the energy gap effectively through reducing influence of surface polarization. This should lower the energy of higher excited states near our laser wavelength. Comparing this finding with the intensities in Fig. 59c), where higher intensities for the CdS Raman mode can be found for higher excitation energies, it seems reasonable to explain the increase during the synthesis with a energetic lowering of the transition energies, moving a higher density of states to the Raman laser energy. The same explanation fits for the CdSe signal; The CdSe Raman intensity decreases for higher excitation energy, hence when the energy is lowered the intensity is reduced.

This not only explains the changes in Raman intensity of the materials, but also shines a light on the shift of emission wavelength, which has been found by several groups, but could not be explained until now. Additionally it means, that the intensity can in principle be used to measure the silica thickness. However, in contrast to the shift in Raman frequency, the interpretation requires a precise knowledge on the transition energies of each QD near the excitation wavelength. It could then be used to reveal the exact distance in which the dielectric interaction takes place, which would be interesting. Here, the intensity of the CdS saturates after about 10 hours, which corresponds to a silica shell thickness of ≈ 12 nm. The CdSe intensity appears to saturate already after about 6 hours, ≈ 10 nm silica thickness. Since the CdSe core is separated from the silica by a CdS shell of about 1.6 nm, the total distance is comparable.

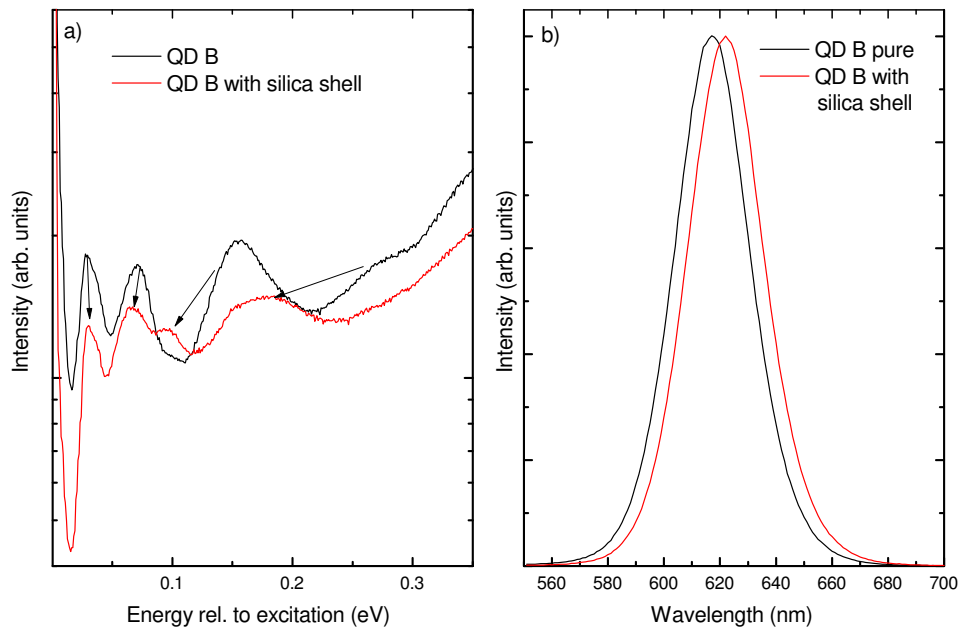


Figure 60: a) PLE measurements of the electronic transition of QD B (pure in black, silica covered in red) at 5K with detection energy in resonance with the main transition, shown relative to the lowest energy transition. Arrows indicated the possible reorganization of higher states due to the silica shell. b) PL spectra of QD B at room temperature before and after silica encapsulation at 365 nm excitation wavelength. The emission of QD B shows a small shift of about 5 nm towards higher wavelength, from 617 nm to 622 nm, after silica encapsulation, which indicates a change in the electronic states of the QD

This shows that the changes of transition energies are certainly out of interest and relevant for the analysis of Raman intensities during the synthesis. Therefore PLE measurements of a pure and a silica covered QD (QD B) are shown in Fig. 60a), relative to the lowest transition energy (which is at a higher energy for the pure QD) and shows that the higher electronic transitions are closer after the QD was covered by the silica shell. The lowest energetic transition is shifted towards red. This is confirmed in room temperature PL measurements, where the lowest transition energy is shifted from 617 nm for the pure QD to 622 nm at room temperature for the silica covered QD, Fig. 60b). Hence the encapsulation has led to an effective reduction of lowest energy transition, which as mentioned above has been observed by many groups. Looking at Fig. 60a), it becomes visible that the distance between the higher energetic transitions is reduced by the addition of the silica shell, which is in agreement with a reduction in confinement as discussed above.

12.8 QD A and QD B's diverging evolution of the Raman spectrum during silica encapsulation

As a result of Section 12.4 and 12.5, we found that the shift in Raman frequency during the silica encapsulation reaction occurs during the nucleation of silica on the Qd's surface until the silica layer has reached a thickness 3 nm. Thereafter the Raman frequency becomes independent of the shell thickness. This was attributed to the formation of an interface between the QD's surface and the silica capping (Section 12.6). What hasn't been addressed yet, is how the amount of shift is changed and what happens if the synthesis is performed on a different QD. For this investigation, two QD with different geometries, QD A and QD B, will be compared. Different aspects of these comparative measurements are shown in Fig. 61.

QD A has a CdSe core with a diameter of 4 nm and a relatively thin CdS shell of 1.6 nm (total diameter 7.2 nm), whereas QD B's core is 3.6 nm in diameter and the CdS shell with 2.8 nm (total diameter 9.1 nm) is much thicker. This, because of strain, causes the Raman modes of the two QDs to have very different initial phonon frequencies. While QD A has Raman frequencies of 210 cm^{-1} and 292 cm^{-1} for core and shell respectively, QD B has frequencies of 212 cm^{-1} and 298 cm^{-1} . So on the one hand, QD A has a shell that has a higher surface area (2.8) compared to volume than QD B(0.8). On the other hand the CdS shell of QD A is under more intense tensile strain than the shell of QD B. The CdSe cores of the QD in contrast are compressively strained, while the strain inside the core is higher for QD B.

Fig.61 shows two different silica synthesis' under different conditions, one for QD A and QD B. The final silica thickness is 13.1 nm for QD A and 8.6 nm for QD B. The change in Raman frequency with 2.2 cm^{-1} is higher für QD A than for QD B, which only shifts by 1 cm^{-1} . The CdSe core of QD B remains unchanged(not shown), QD A's core shifts by a small amount towards higher frequencies as discussed in Sec. 8, Fig. 54, so the focus is on the shift caused in the CdS shell. How much the addition of the silica influences the Raman signal of core and shell, seems to directly depend on the QD's geometry.

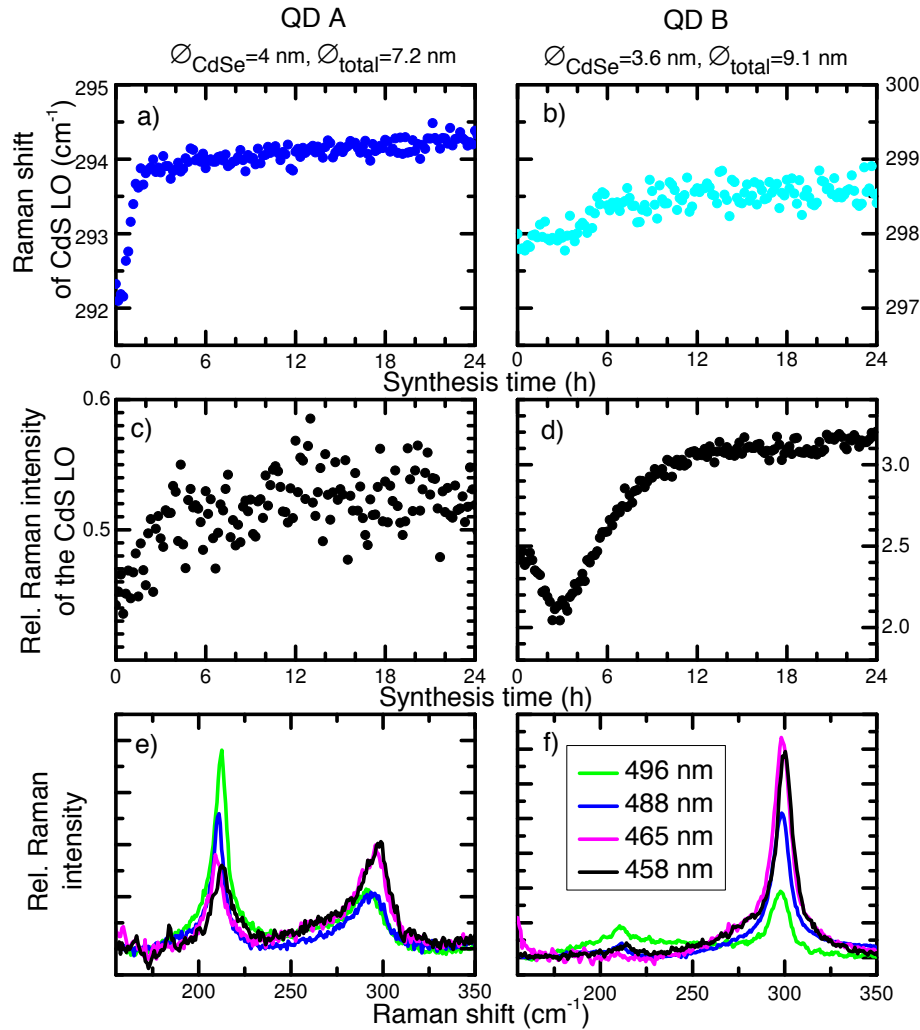


Figure 61: (a)/(b) Raman frequencies of the CdS mode in the course of the silica synthesis for QD A/ QD B; (c)/(d) Raman intensity ratios (peak area) for the CdS mode in the course of the silica synthesis for QD A/ QD B, normalized to solvent intensities to exclude influences of the laser power; (e)/(f) Raman spectra of QD A/QD B for different laser energies, intensity normalized to solvent as indicated above. [150]

However, this is not the only difference between the two samples. The evolution of intensity during the synthesis, displayed in Fig. 61, diverges greatly between the two QDs. While the intensity of the CdS Raman mode increases for QD A, QD B shows a distinct dip in intensity after two hours of synthesis, accompanied by a faster and stronger change in Raman intensity than for QD A (compare Fig. 61c and d). The step rise in intensity

indicates a higher sensitivity to the dielectric environment for QD B, which is also supported by the stronger change in intensity upon excitation with higher energies (see Fig. 61f and for comparison with QD A 61e). The higher dependence of the Raman intensity on excitation energy makes sense, since the shell of QD B is thick and thus should have electronic properties similar to bulk CdS which has an absorption edge at around 500 nm[158] close to the excitation wavelength (of 488 nm). As right at the absorption edge, the density of electronic states dramatically changes in dependence of energy, a strong dependence of Raman intensity on energy logically follows. The shell of QD A, with a thickness of 1.6 nm only, is very much in the confinement regime and hence the electronic states should be shifted towards higher energies and therewith further away from the excitation laser used in this experiment.

The dip in intensity that occurs during silica encapsulation of QD B (at a silica thickness of 2.5 nm after 3h of reaction), cannot be explained by the increase of surrounding dielectric constant as above. To further understand this dip in intensity, we have to remind ourselves of the mechanism of the synthesis, as discussed in Section 12.2. The dielectric environment of the QD changes over the whole synthesis from a mixture of ligands and cyclohexane to silica, but as a transitional stage the QD has to travel into a micelle of water. Water however has a lower dielectric constant $\epsilon \approx 1.8$ [159] than both, Cyclohexane and silica. Hence, when in close proximity to the QD, it should have the opposite effect on the electronic transitions of the QD than the silica. So, as long as the silica shell is thin or only partially covers the QD, the effective dielectric constant of the environment is lowered by the introduction of water in the environment. This temporarily leads to a shift of the electronic transitions of the QD (shell) towards higher energies. This environment is then successively moved further and further away from the QD as the silica shell grows until the QD is surrounded by silica only and the electronic transitions shift to their final position at lower energies. Thus for the thicker shelled QD B, it is possible to observe the transition of the QD from the solution of Cyclohexane into the water micelle and therewith delivers an observation, that can't be made by any other method.

This once more underlines the complexity of interpretation of the trend in Raman intensity and the necessity of a very precise knowledge on the resonance conditions and electronic transitions of the sample, as QD A and QD B yield very different observations. However, these observations are strongly energy-dependent, hence an in situ measurement with different excitation energies must give different results, and every different QD dependent on their electronic transitions will have a distinct resonance condition. Nevertheless the observations made by monitoring the Raman intensity during the encapsulation are unique and can potentially offer intricate details on the synthesis mechanism. Additionally, the influence of the use of differ-

ently bound ligands on the surface of the QD should reflect in the dip in intensity as they should influence the introduction of water in the proximity of the QD. The transition of the QD into the water micelle should also be influence by the type of and concentration surfactant, which should be observable monitoring the Raman intensity.

13 Conclusions

In this work, the vibronic and electronic properties of spherical, colloidal CdSe QDs were studied, as well as CdSe/CdS core-shell QDs. The dependence on crystal symmetry was evaluated using experimental methods like Raman spectroscopy, TEM and PLE.

The Raman-based strain analysis of spherical core-shell QDs agrees well with previous publications[43, 160]: compressive strain is found in the CdSe core while tensile strain is exerted on the CdS shell. It was demonstrated that the strain depends on the geometry of the QD, and that an increasing shell thickness on a constantly sized core results in an increasing strain within the CdSe core, while it reduces strain in the CdS shell. Additionally, the shell addition leads to a shift in emission frequency towards red, as observed in absorption and PL measurements, partially relieving the confinement of the charge carriers.

Two different methods of shell synthesis, SILAR and FLASH, were compared; where the former is the well-established method, the latter allows a much faster synthesis using a higher temperature. An analysis of the interface mode – which resides in the sideband of the CdSe LO mode – revealed no significant reductions in intensity and shape of the mode between both synthesis methods. This shows that the faster reaction method (FLASH) can also provide a graded interface, which is highly favorable as it improves the radiative recombination efficiency.

The lattice parameters, therefore also the strain values that were published so far are found to differ strongly from each other, as they are highly dependent on the precise ambient temperature during measurement. These presumably temperature dependent differences indicate diverging temperature coefficients for the two materials. The analysis of temperature dependent Raman measurements and subsequent separation of strain effects allows access to temperature coefficients for the two materials. Careful examination thus reveals different thermal expansion coefficients for CdSe and CdS, which are independent of the CdS shell thickness, and thus evidence a correct separation of effects. The thermal expansion coefficient of the CdS shell is independent of the crystal structure and shows only a small, slow increase with temperature. The CdSe core's temperature dependence however shows a steep increase at low temperatures, hinting at a size dependence, which should be checked in further studies. For zincblende QDs it is shown that smaller dots exhibit a stronger temperature dependence.

CdSe cores that have a wurtzite structure expand fast and at lower temperature than zincblende structures with equivalent diameter; they however show an overall smaller temperature dependence. This is shown to originate from the distinct crystal structure.

The exciton-phonon coupling within the QD is studied with Raman spectroscopy, revealing a size dependent minimum in coupling strength for QD

with a zincblende structure at a diameter of about 4.7 nm, for wurtzite QDs between 3.8 and 4.4 nm, which indicates a lower band offset to the environment for wurtzite QDs. The coupling strength of 0.1-0.2 for zincblende QDs is in line with previous findings. However wurtzite QDs exhibit, outside of the minimum exhibit a larger coupling strength by factors 2-4, diameter dependently. This shows again the different properties for the two crystal structures. The coupling strength is found to decrease upon addition of a CdS shell, both in Raman and resonance PL.

Further differences between the two crystal structures are revealed in the diameter dependent band edge fine structure, which is examined with excitation spectroscopy. It is shown that the obtained PL signal is strongly dependent on resonances, which are unique for each QD diameter. Dedicated analysis on samples with a broad range of diameters shows that while the inherent diameter distributions results in overlapping signals, the overall dependence on the excitation energy can still be extracted nicely. This demonstrates that ensemble measurements can well be used to extract the continuous band edge fine structure over a broad range of diameters.

For both crystal structures, well separated bright and dark states are observed, the latter having a slightly lower energy. For instance for a QD with 3 nm in diameter, the wurtzite structure has an energetic separation between dark and bright state of 16 meV, zincblende only 10 meV. As shown, the splitting between the bright-dark splitting decreases with an increasing QD diameter. This splitting of band-edge states was already observed for wurtzite QDs, and explained with the inherent crystal fields in the QDs. For the zincblende structure, however, this splitting is shown here for the first time for such a broad diameter range, and is additionally completed with an analysis of the band edge states above the bright state, which are only revealed by excitation spectroscopy. A shape anisotropy is considered as potential reason for the induced splitting, analyzed with a model already used by Efros [83] for the description of the band edge states of wurtzite CdSe QDs, based on the A-B exciton splitting in the bulk semiconductor. The splitting between the bright and the dark state can be well described with this model, considering a deformation of 10% in oblate direction. Such deformation, however, can't explain the high energetic separation of the next higher band edge states compared to the bright state, if keeping in line with the original assignment. The large separation of states can only be achieved, assuming a broad deformation gradient of 10% to 50% over the diameter range, which seems unrealistic.

An alternative explanation is given here, where the higher lying band edge states are phonon replica of those excited QDs, that have a higher ground state energy. This theory completely changes the view on the interpretation of measurements that has been used for 20 years. It also highlights how important the coupling between excitons and the phononic system is, especially in these kind of nano-structures, and should be carefully considered

in the analysis of future experiments.

After analyzing the basic physical properties of QDs, this thesis turns its focus to the more complex structure of colloidal silica encapsulated QDs. These hybrid systems are currently highly investigated for their potential use as biological cell-labels, due to their potentially high, long-term quantum yield and biocompatibility. Additionally, they exhibit a high stability in aqueous solution, which has been successfully demonstrated for certain synthesis conditions [70, 74, 76, 147], depending on the QD surface chemistry. However much investigated, no direct evidence has been found regarding whether the silica interacts directly with the QD surface, or if the ligand shell remains on the QD surface and the silica is formed on the outside.

Using Raman spectroscopy during the encapsulation reaction in combination with TEM analysis for determination of the silica shell thickness, it is revealed that using loosely bound ligands, an interface between silica and QD is formed during the first hours of synthesis (1-4h of 48h of synthesis in total). In fact, the *in situ* analysis of the changing Raman spectra indicates that the interface reduces the surface undercoordination, and that the overall crystal quality is surprisingly even increased. Out of the many possible bonds that could constitute this interface, Cd-O-Si bonds are closest in length and electronegativity to the optimal Cd-S bond; this would then explain the shift in Raman frequency toward the relaxed bulk value. Through observation of the intensities of the individual Raman modes, changes in the dielectric environment can be directly monitored, which can potentially be used to derive silica shell thicknesses directly during of the synthesis.

In summary, Raman spectroscopy is a useful tool for the analysis of the silica encapsulation reaction, and can be used in investigations of varying QD ligands, microemulsion surfactant, or pH condition. This thesis then provides a highly interesting tool to design an optimized synthesis route towards the production of materials with ideal optical properties.

This work highlights the versatility of Raman spectroscopy in the analysis of colloidal QDs, and emphasizes that it should be used in addition to the conventionally used TEM, absorption and PL measurements. It shines light on information that would be complicated to assess otherwise, e.g. the strain, temperature dependent lattice expansion, and even information on interfaces within the QD and the respective surface chemistry. Complementary PLE measurements offer an in-depth view on the electronic states, the band edge fine structure and demonstrate that those observations are also governed by phonon assisted recombination and an overall strong coupling to the lattice phonons.

14 Bibliography

- [1] D. V. Talapin, J.-S. Lee, M. V. Kovalenko, and E. V. Shevchenko, “Prospects of Colloidal Nanocrystals for Electronic and Optoelectronic Applications”, *Chem. Rev.* **110**, 389–458 (2010) (cit. on pp. 2, 4).
- [2] L. Jing, S. V. Kershaw, Y. Li, X. Huang, Y. Li, A. L. Rogach, and M. Gao, “Aqueous Based Semiconductor Nanocrystals”, *Chem. Rev.* **116**, 10623–10730 (2016) (cit. on pp. 2, 5).
- [3] J. M. Pietryga, Y.-S. Park, J. Lim, A. F. Fidler, W. K. Bae, S. Brovelli, and V. I. Klimov, “Spectroscopic and Device Aspects of Nanocrystal Quantum Dots”, *Chem. Rev.* **116**, 10513–10622 (2016) (cit. on pp. 2, 5).
- [4] D. V. Talapin and E. V. Shevchenko, “Introduction: Nanoparticle Chemistry”, *Chem. Rev.* **116**, 10343–10345 (2016) (cit. on p. 2).
- [5] V. L. Colvin, M. C. Schlamp, and A. P. Alivisatos, “Light-emitting diodes made from cadmium selenide nanocrystals and a semiconducting polymer”, *Nature* **370**, 354–357 (1994) (cit. on p. 4).
- [6] H. Mattoussi, L. H. Radzilowski, B. O. Dabbousi, E. L. Thomas, M. G. Bawendi, and M. F. Rubner, “Electroluminescence from heterostructures of poly(phenylene vinylene) and inorganic CdSe nanocrystals”, *J. Appl. Phys.* **83**, 7965–11 (1998) (cit. on p. 4).
- [7] N. C. Greenham, X. Peng, and A. P. Alivisatos, “Charge separation and transport in conjugated-polymer/semiconductor-nanocrystal composites studied by photoluminescence quenching and photoconductivity”, *Phys. Rev., B Condens. Matter* **54**, 17628–17637 (1996) (cit. on p. 4).
- [8] S. S. Coe, W.-K. W. Woo, M. M. Bawendi, and V. V. Bulović, “Electroluminescence from single monolayers of nanocrystals in molecular organic devices.”, *Nature* **420**, 800–803 (2001) (cit. on p. 4).
- [9] J. Zhao, J. Zhang, C. Jiang, J. Bohnenberger, T. Basché, and A. Mews, “Electroluminescence from isolated CdSe/ZnS quantum dots in multilayered light-emitting diodes”, *J. Appl. Phys.* **96**, 3206–6 (2004) (cit. on p. 4).
- [10] A. Mews and J. Zhao, “Light-emitting diodes: A bright outlook for quantum dots”, *Nature Photon* **1**, 683–684 (2007) (cit. on p. 4).
- [11] E. Jang, S. Jun, H. Jang, J. Lim, B. Kim, and Y. Kim, “White-Light-Emitting Diodes with Quantum Dot Color Converters for Display Backlights”, *Adv. Mater* **22**, 3076–3080 (2010) (cit. on p. 4).

- [12] C. Dang, J. Lee, C. Breen, J. S. Steckel, S. Coe-Sullivan, and A. Nurmikko, “Red, green and blue lasing enabled by single-exciton gain in colloidal quantum dot films”, *Nature Nanotech* **7**, 335–339 (2012) (cit. on p. 4).
- [13] R. R. Lunt, T. P. Osedach, P. R. Brown, J. A. Rowehl, and V. Bulović, “Practical roadmap and limits to nanostructured photovoltaics.”, *Adv. Mater. Weinheim* **23**, 5712–5727 (2011) (cit. on p. 4).
- [14] X. Lan, O. Voznyy, F. P. García de Arquer, M. Liu, J. Xu, A. H. Proppe, G. Walters, F. Fan, H. Tan, M. Liu, Z. Yang, S. Hoogland, and E. H. Sargent, “10.6Solvent-Polarity-Engineered Halide Passivation”, *Nano Lett.* **16**, 4630–4634 (2016) (cit. on p. 5).
- [15] G. I. Koleilat, L. Levina, H. Shukla, S. H. Myrskog, S. Hinds, A. G. Pattantyus-Abraham, and E. H. Sargent, “Efficient, Stable Infrared Photovoltaics Based on Solution-Cast Colloidal Quantum Dots”, *ACS Nano* **2**, 833–840 (2008) (cit. on p. 5).
- [16] A. Hagfeldt and M. Grätzel, “Molecular Photovoltaics”, *Acc. Chem. Res.* **33**, 269–277 (2000) (cit. on p. 5).
- [17] M. J. Bruchez, M. Moronne, P. Gin, S. Weiss, and A Paul Alivisatos, “Semiconductor Nanocrystals as Fluorescent Biological Labels”, *Science* **281**, 2013– (1998) (cit. on p. 5).
- [18] W. C. W. Chan and S. Nie, “Quantum Dot Bioconjugates for Ultra-sensitive Nonisotopic Detection”, *Science* **281**, 2016– (1998) (cit. on p. 5).
- [19] J. Gao and B. Xu, “Applications of nanomaterials inside cells”, *Nano Today* **4**, 37–51 (2009) (cit. on p. 6).
- [20] I. L. Medintz, H. T. Uyeda, E. R. Goldman, and H. Mattoussi, “Quantum dot bioconjugates for imaging, labelling and sensing”, *Nature Materials* **4**, 435–446 (2005) (cit. on p. 5).
- [21] X. Wu, H. Liu, J. Liu, K. N. Haley, J. A. Treadway, J. P. Larson, N. Ge, F. Peale, and M. P. Bruchez, “Immunofluorescent labeling of cancer marker Her2 and other cellular targets with semiconductor quantum dots”, *Nat Biotech* **21**, 41–46 (2002) (cit. on p. 5).
- [22] W. C. W. Chan, D. J. Maxwell, X. Gao, R. E. Bailey, M. Han, and S. Nie, “Luminescent quantum dots for multiplexed biological detection and imaging”, *Current Opinion in Biotechnology* **13**, 40–46 (2002) (cit. on p. 5).
- [23] A. Guerrero Martínez, J. Pérez Juste, and L. M. Liz-Marzán, “Recent Progress on Silica Coating of Nanoparticles and Related Nanomaterials”, *Adv. Mater. Weinheim* **22**, 1182–1195 (2010) (cit. on pp. 6, 85).

- [24] V. W. Manner, A. Y. Kopolov, P. Szymanski, and V. I. Klimov, “Role of solvent–oxygen ion pairs in photooxidation of cdse nanocrystal quantum dots”, *ACS Nano* **6**, 2371–2377 (2012) (cit. on p. 6).
- [25] Y Wang, Z Tang, and M. A. Correa-Duarte, “Mechanism of strong luminescence photoactivation of citrate-stabilized water-soluble nanoparticles with CdSe cores”, *J. Phys. Chem. B* **108**, 15461–15469 (2004) (cit. on p. 6).
- [26] Y Zhang, J He, P. N. Wang, J. Y. Chen, and Z. J. Lu, “Time-dependent photoluminescence blue shift of the quantum dots in living cells: effect of oxidation by singlet oxygen”, *J. AM. CHEM. SOC.* **128**, 13396–13401 (2006) (cit. on p. 6).
- [27] M. A. Hines and P. Guyot-Sionnest, “Synthesis and Characterization of Strongly Luminescing ZnS-Capped CdSe Nanocrystals”, *J Phys Chem* **100**, 468–471 (1996) (cit. on pp. 7, 8).
- [28] L. Qu and X. Peng, “Control of Photoluminescence Properties of CdSe Nanocrystals in Growth”, *J. Am. Chem. Soc.* **124**, 2049–2055 (2002) (cit. on pp. 7, 8).
- [29] L. Carbone, C. Nobile, M. De Giorgi, F. D. Sala, G. Morello, P. Pompa, M. Hytch, E. Snoeck, A. Fiore, I. R. Franchini, M. Nadasan, A. F. Silvestre, L. Chiodo, S. Kudera, R. Cingolani, R. Krahne, and L. Manna, “Synthesis and Micrometer-Scale Assembly of Colloidal CdSe/CdS Nanorods Prepared by a Seeded Growth Approach”, *Nano Lett.* **7**, 2942–2950 (2007) (cit. on pp. 7, 8).
- [30] M. L. Cohen and J. R. Chelikowsky, *ELECTRONIC STRUCTURE AND OPTICAL PROPERTIES OF SEMICONDUCTORS* (Springer-Verlag, Berlin, 1988) (cit. on pp. 8, 32).
- [31] R. W. G. Wyckoff, *CRYSTAL STRUCTURES* (Wiley, New York, 1963) (cit. on pp. 8, 32).
- [32] K. H. Hellwege and O. M. Landolt-Bornstein, *PHYSICS OF GROUP IV ELEMENTS AND III-V COMPOUNDS*, Vol. 22 (Springer, Berlin, 1982) (cit. on pp. 8, 32).
- [33] K. H. Hellwege and O. M. Landolt-Bornstein, *PHYSICS OF GROUP IV ELEMENTS AND III-V COMPOUNDS*, Vol. 17 (Springer, Berlin, 1982) (cit. on pp. 8, 32).
- [34] Y. Chen, J. Vela, H. Htoon, J. L. Casson, D. J. Werder, D. A. Busian, V. I. Klimov, and J. A. Hollingsworth, ““Giant” Multishell CdSe Nanocrystal Quantum Dots with Suppressed Blinking”, *J. Am. Chem. Soc.* **130**, 5026–5027 (2008) (cit. on p. 9).
- [35] B. Mahler, P. Spinicelli, S. Buil, X. Quelin, J.-P. Hermier, and B. Dubertret, “Towards non-blinking colloidal quantum dots”, *Nature Materials* **7**, 659–664 (2008) (cit. on p. 9).

- [36] Y. Ghosh, B. D. Mangum, J. L. Casson, D. J. Williams, H. Htoon, and J. A. Hollingsworth, “New Insights into the Complexities of Shell Growth and the Strong Influence of Particle Volume in Nonblinking “Giant” Core/Shell Nanocrystal Quantum Dots”, *J. Am. Chem. Soc.* **134**, 9634–9643 (2012) (cit. on pp. 9, 26).
- [37] J. Vela, H. Htoon, Y. Chen, Y.-S. Park, Y. Ghosh, P. M. Goodwin, J. H. Werner, N. P. Wells, J. L. Casson, and J. A. Hollingsworth, “Effect of shell thickness and composition on blinking suppression and the blinking mechanism in ‘giant’ CdSe/CdS nanocrystal quantum dots”, *J. Biophotonics* **3**, 706–717 (2010) (cit. on p. 9).
- [38] C. D. Heyes, A. Y. Kobitski, V. V. Breus, and G. U. Nienhaus, “Effect of the shell on the blinking statistics of core-shell quantum dots: A single-particle fluorescence study”, *PRB* **75**, 125431–8 (2007) (cit. on p. 9).
- [39] P. Frantsuzov, M. Kuno, B. Janko, and R. A. Marcus, “Universal emission intermittency in quantum dots, nanorods, and nanowires”, *Nat. Phys.* **4**, 519–522 (2008) (cit. on p. 9).
- [40] G. E. Cragg and A. L. Efros, “Suppression of Auger Processes in Confined Structures”, *Nano Lett.* **10**, 313–317 (2010) (cit. on p. 9).
- [41] F. García-Santamaría, S. Brovelli, R. Viswanatha, J. A. Hollingsworth, H. Htoon, S. A. Crooker, and V. I. Klimov, “Breakdown of Volume Scaling in Auger Recombination in CdSe/CdS Heteronanocrystals: The Role of the Core-Shell Interface”, *Nano Lett.* **11**, 687–693 (2011) (cit. on p. 9).
- [42] X. Wang, X. Ren, K. Kahen, M. A. Hahn, M. Rajeswaran, S. Maccagnano-Zacher, J. Silcox, G. E. Cragg, A. L. Efros, and T. D. Krauss, “Non-blinking semiconductor nanocrystals”, *Nature* **459**, 686–689 (2009) (cit. on p. 10).
- [43] N. Tschirner, H. Lange, A. Schliwa, A. Biermann, C. Thomsen, K. Lambert, R. Gomes, and Z. Hens, “Interfacial Alloying in CdSe/CdS Heteronanocrystals: A Raman Spectroscopy Analysis”, *Chem. Mater.* **24**, 311–318 (2012) (cit. on pp. 10, 27, 28, 47, 61, 87, 113).
- [44] D. Mourad, A. Guille, T. Aubert, E. Brainis, and Z. Hens, “Random-Alloying Induced Signatures in the Absorption Spectra of Colloidal Quantum Dots”, *Chem. Mater.* **26**, 6852–6862 (2014) (cit. on p. 10).
- [45] R. Vaxenburg, A. Rodina, E. Lifshitz, and A. L. Efros, “Biexciton Auger Recombination in CdSe/CdS Core/Shell Semiconductor Nanocrystals”, *Nano Lett.*, [acs.nanolett.6b00066–9](https://doi.org/10.1021/acs.nanolett.6b00066) (2016) (cit. on p. 10).

- [46] B Khodadoost, S. A. Lee, J. B. Page, and R. C. Hanson, “Resonance Raman scattering and optical absorption studies of MnO_4^- in KClO_4 at high pressure”, *Phys. Rev. B* **38**, 5288–5295 (1988) (cit. on pp. 13, 47).
- [47] J. H. Wasilik, “Attenuation of c propagating acoustic waves in CdS: Grüneisen parameter calculations”, *Appl. Phys. Lett.* **24**, 153–3 (1974) (cit. on pp. 13, 47).
- [48] G Scamarcio, M Lugara, and D Manno, “Size-dependent lattice contraction in $\text{CdS}_{1-x}\text{Se}_x$ nanocrystals embedded in glass observed by Raman scattering”, *Phys. Rev. B* (1992) (cit. on p. 13).
- [49] V. M. Dzhagan, M Ya Valakh, A. E. Raevskaya, A. L. Stroyuk, S. Y. Kuchmiy, and D. R. T. Zahn, “Size effects on Raman spectra of small CdSe nanoparticles in polymer films”, *NANOTECHNOLOGY* **19**, 305707 (2008) (cit. on pp. 13, 35).
- [50] H Fröhlich, “Electrons in lattice fields”, *Advances in Physics* **3**, 325–361 (1954) (cit. on p. 14).
- [51] K. Huang and A. Rhys, “Theory of Light Absorption and Non-Radiative Transitions in F-Centres”, in *Proceedings of the royal society of london. series a* (Dec. 1950), pp. 406–423 (cit. on p. 14).
- [52] T. H. Keil, “Shapes of Impurity Absorption Bands in Solids”, *Physical Review* **140**, 601–617 (1965) (cit. on pp. 14, 15).
- [53] T. P. Martin and S Onari, “Multiple-order Raman scattering in MnO_4^{2-} -doped CsI”, *Phys. Rev. B* **15**, 1093 (1977) (cit. on p. 15).
- [54] I. S. Gradshteyu and I. M. Ryzhik, *Table of Integrals Series and Products* (AP, Apr. 1965) (cit. on p. 15).
- [55] M. C. Klein, F Hache, D Ricard, and C Flytzanis, “Size dependence of electron-phonon coupling in semiconductor nanospheres: The case of CdSe”, *Phys. Rev., B Condens. Matter* **42**, 11123–11132 (1990) (cit. on pp. 15, 55).
- [56] A. C. Albrecht, “On the Theory of Raman Intensities”, *J. Chem. Phys.* **34**, 1476–1484 (1961) (cit. on p. 15).
- [57] R Merlin, G Güntherodt, R Humphreys, M Cardona, R Suryanarayanan, and F Holtzberg, “Multiphonon processes in YbS”, *Phys. Rev. B* **17**, 4951–4958 (1978) (cit. on p. 15).
- [58] A. P. Alivisatos, T. D. Harris, P. J. Carroll, M. L. Steigerwald, and L. E. Brus, “Electron-vibration coupling in semiconductor clusters studied by resonance Raman spectroscopy”, *J. Chem. Phys.* **90**, 3463–3468 (1989) (cit. on p. 15).

- [59] A. M. Kelley, “Resonance Raman Overtone Intensities and Electron-Phonon Coupling Strengths in Semiconductor Nanocrystals”, *The Journal of Physical Chemistry A* **117**, 6143–6149 (2013) (cit. on pp. 15, 56).
- [60] H Telg, “Raman studies on individual nanotubes and nanotube ensembles-vibrational properties and scattering efficiencies”, PhD thesis (Berlin, 2009) (cit. on p. 17).
- [61] J. Park, J. Joo, S. G. Kwon, Y. Jang, and T. Hyeon, “Synthesis of Monodisperse Spherical Nanocrystals”, *Angew. Chem. Int. Ed.* **46**, 4630–4660 (2007) (cit. on pp. 21, 22).
- [62] S. Abe, R. K. Čapek, B. De Geyter, and Z. Hens, “Tuning the Post-focused Size of Colloidal Nanocrystals by the Reaction Rate: From Theory to Application”, *ACS Nano* **6**, 42–53 (2012) (cit. on pp. 21–23).
- [63] S. Abe, R. K. Čapek, B. De Geyter, and Z. Hens, “Reaction Chemistry/Nanocrystal Property Relations in the Hot Injection Synthesis, the Role of the Solute Solubility”, *ACS Nano* **7**, 943–949 (2013) (cit. on pp. 21–23).
- [64] D. V. Talapin, A. L. Rogach, M. Haase, and H. Weller, “Evolution of an Ensemble of Nanoparticles in a Colloidal Solution: Theoretical Study”, *J. Phys. Chem. B* **105**, 12278–12285 (2001) (cit. on pp. 21, 22).
- [65] C. B. Murray, D. B. Norris, and M. G. Bawendi, *Synthesis and characterization of nearly monodisperse CdE (E= S, Se, Te) semiconductor nanocrystallite* (*J. Am. Chem. Soc.*, 1993) (cit. on p. 22).
- [66] C. B. Murray and C. R. Kagan, “Synthesis and characterization of monodisperse nanocrystals and close-packed nanocrystal assemblies”, *Annual Review of Materials Science* **30**, 545–610 (2000) (cit. on p. 22).
- [67] A. P. Alivisatos, “Semiconductor Clusters, Nanocrystals, and Quantum Dots”, *Science* **271**, 933–937 (1996) (cit. on p. 22).
- [68] X Peng, M. C. Schlamp, and A. V. Kadavanich, “Epitaxial growth of highly luminescent CdSe/CdS core/shell nanocrystals with photostability and electronic accessibility”, *J. AM. CHEM. SOC.* **119**, 7019–7029 (1997) (cit. on p. 22).
- [69] M. Cirillo, T. Aubert, R. Gomes, R. Van Deun, P. Emplit, A. Biermann, H. Lange, C. Thomsen, E. Brainis, and Z. Hens, “Flash Synthesis of CdSe/CdS Core–Shell Quantum Dots”, *Chem. Mater.* **26**, 1154–1160 (2014) (cit. on pp. 24, 26–28, 92).

- [70] T. Aubert, S. J. Soenen, D. Wassmuth, M. Cirillo, R. Van Deun, K. Braeckmans, and Z. Hens, “Bright and Stable CdSe/CdS@SiO₂ Nanoparticles Suitable for Long-Term Cell Labeling”, *ACS Appl. Mater. Interfaces* **6**, 11714–11723 (2014) (cit. on pp. 24, 26, 29, 85, 86, 90, 92, 115).
- [71] P Mulvaney, L. M. Liz-Marzán, M Giersig, and T Ung, “Silica encapsulation of quantum dots and metal clusters”, *J. Mater. Chem.* **10**, 1259–1270 (2000) (cit. on pp. 28, 85).
- [72] D. Gerion, F. Pinaud, S. C. Williams, W. J. Parak, D. Zanchet, S. Weiss, and A. P. Alivisatos, “Synthesis and Properties of Biocompatible Water-Soluble Silica-Coated CdSe/ZnS Semiconductor Quantum Dots †”, *J. Phys. Chem. B* **105**, 8861–8871 (2001) (cit. on pp. 28, 85).
- [73] M Darbandi, R Thomann, and T Nann, “Single quantum dots in silica spheres by microemulsion synthesis”, *Chem. Mater.* **17**, 5720–5725 (2005) (cit. on pp. 28, 85, 88, 90, 91, 104).
- [74] R. Koole, M. M. van Schooneveld, J. Hilhorst, C. De Mello Donegá, D. C. t. Hart, A. van Blaaderen, D. Vanmaekelbergh, and A. Meijerink, “On the Incorporation Mechanism of Hydrophobic Quantum Dots in Silica Spheres by a Reverse Microemulsion Method”, *Chem. Mater.* **20**, 2503–2512 (2008) (cit. on pp. 28, 85, 88, 90, 104, 115).
- [75] S. T. Selvan, T. T. Tan, and J. Y. Ying, “Robust, Non-Cytotoxic, Silica-Coated CdSe Quantum Dots with Efficient Photoluminescence”, *Adv. Mater* **17**, 1620–1625 (2005) (cit. on pp. 28, 85, 88).
- [76] M. Acebrón, J. F. Galisteo-López, D. Granados, J. López-Ogalla, J. M. Gallego, R. Otero, C. López, and B. H. Juárez, “Protective Ligand Shells for Luminescent SiO₂-Coated Alloyed Semiconductor Nanocrystals”, *ACS Appl. Mater. Interfaces* **7**, 6935–6945 (2015) (cit. on pp. 28, 85, 87, 91, 115).
- [77] J. J. Li, Y. A. Wang, W. Guo, J. C. Keay, T. D. Mishima, M. B. Johnson, and X. Peng, “Large-Scale Synthesis of Nearly Monodisperse CdSe/CdS Core/Shell Nanocrystals Using Air-Stable Reagents via Successive Ion Layer Adsorption and Reaction”, *J. Am. Chem. Soc.* **125**, 12567–12575 (2003) (cit. on p. 29).
- [78] E. Drijvers, J. De Roo, P. Geiregat, K. Fehér, Z. Hens, and T. Aubert, “Revisited Wurtzite CdSe Synthesis: A Gateway for the Versatile Flash Synthesis of Multishell Quantum Dots and Rods”, *Chem. Mater.* **28**, 7311–7323 (2016) (cit. on pp. 29, 91).
- [79] M. Grünwald, A. Zayak, J. B. Neaton, P. L. Geissler, and E. Rabani, “Transferable pair potentials for CdS and ZnS crystals”, *J. Chem. Phys.* **136**, 234111–234117 (2012) (cit. on pp. 32, 53).

- [80] C Trallero-Giner, A Debernardi, M Cardona, E Menéndez-Proupín, and A. I. Ekimov, “Optical vibrons in CdSe dots and dispersion relation of the bulk material”, *Phys. Rev. B (Condensed Matter and Materials Physics)* **57**, 4664–4669 (1998) (cit. on pp. 35, 36, 53).
- [81] L. Börnstein, *Group III Condensed Matter, Semiconductors, II – VI and I – VII Compounds; Semimagnetic Compounds*, Vol. 41, Group III Condensed Matter (Springer, Berlin, 1999) (cit. on p. 35).
- [82] A. G. del Águila, E. Groeneveld, J. C. Maan, C. De Mello Donegá, and P. C. M. Christianen, “Effect of Electron–Hole Overlap and Exchange Interaction on Exciton Radiative Lifetimes of CdTe/CdSe Heteronanocrystals”, *Appl. Phys. Lett.* **81**, 2076 (2016) (cit. on p. 35).
- [83] A. L. Efros, M Rosen, M Kuno, M Nirmal, D. J. Norris, and M Bawendi, “Band-edge exciton in quantum dots of semiconductors with a degenerate valence band: Dark and bright exciton states”, *Phys. Rev., B Condens. Matter* **54**, 4843–4856 (1996) (cit. on pp. 35, 55, 64, 68, 75, 114).
- [84] H Richter, Z. P. Wang, and L Ley, “The one phonon Raman spectrum in microcrystalline silicon”, *Solid State Communications* **39**, 625–629 (1981) (cit. on p. 35).
- [85] L Saviot, “Size dependence of acoustic and optical vibrational modes of CdSe nanocrystals in glasses”, *Journal of Non-Crystalline Solids* **197**, 238–246 (1996) (cit. on p. 35).
- [86] R. W. Meulenbergh, T. Jennings, and G. F. Strouse, “Compressive and tensile stress in colloidal CdSe semiconductor quantum dots”, *Phys. Rev. B* **70**, 235311 (2004) (cit. on p. 35).
- [87] W. S. O. Rodden, C. M. Sotomayor Torres, and C. N. Ironside, “Three-dimensional phonon confinement in CdSe microcrystallites in glass”, *Semicond. Sci. Technol.* **10**, 807–812 (1995) (cit. on pp. 35, 40).
- [88] A. Tanaka, S. Onari, and T. Arai, “Raman scattering from CdSe microcrystals embedded in a germanate glass matrix”, *Phys. Rev., B Condens. Matter* **45**, 6587–6592 (1992) (cit. on p. 35).
- [89] A. G. Rolo and M. I. Vasilevskiy, “Raman spectroscopy of optical phonons confined in semiconductor quantum dots and nanocrystals”, *J. Raman Spectrosc.* **38**, 618–633 (2007) (cit. on p. 35).
- [90] R Beserman, “ZONE EDGE PHONONS IN CdS_{1-x}Se_x”, *Solid State Communications* **23**, 323–327 (1977) (cit. on p. 38).
- [91] J. F. Scott and T. C. Damen, “Raman scattering from surface modes of small CdS crystallites”, *Optics Communications* (1972) (cit. on pp. 40, 87).

- [92] F Comas and C Trallero-Giner, “Surface optical phonons in spherically capped quantum-dot/quantum-well heterostructures”, *J. Appl. Phys.* **94**, 6023 (2003) (cit. on p. 40).
- [93] Y.-N. Hwang, S.-H. Park, and D. Kim, “Size-dependent surface phonon mode of CdSe quantum dots”, *Phys. Rev. B (Condensed Matter and Materials Physics)* **59**, 7285–7288 (1999) (cit. on p. 40).
- [94] R. Gupta, Q Xiong, G. D. Mahan, and P. C. Eklund, “Surface Optical Phonons in Gallium Phosphide Nanowires”, *Nano Lett.* **3**, 1745–1750 (2003) (cit. on p. 40).
- [95] Q. Xiong, J. Wang, O Reese, L. C. Lew Yan Voon, and P. C. Eklund, “Raman Scattering from Surface Phonons in Rectangular Cross-sectional w-ZnS Nanowires”, *Nano Lett.* **4**, 1991–1996 (2004) (cit. on pp. 40, 87).
- [96] H. H. Lange, M. M. Artemyev, U. U. Woggon, and C. C. Thomsen, “Geometry dependence of the phonon modes in CdSe nanorods.”, *NANOTECHNOLOGY* **20**, 045705–045705 (2009) (cit. on p. 40).
- [97] F Comas and C Trallero-Giner, “Interface optical phonons in spherical quantum-dot/quantum-well heterostructures”, *Phys. Rev. B* **67**, 115301 (2003) (cit. on p. 40).
- [98] A Baranov, Y. Rakovich, J Donegan, T Perova, R Moore, D Talapin, A Rogach, Y Masumoto, and I Nabiev, “Raman analysis of CdSe/CdS core-shell quantum dots with different CdS shell thickness”, *Phys. Rev. B* **68**, 165306 (2003) (cit. on p. 40).
- [99] A. Giugni, G. Das, A. Alabastri, R. P. Zaccaria, M. Zanella, I. Franchini, E. Di Fabrizio, and R. Krahne, “Optical phonon modes in ordered core-shell CdSe/CdS nanorod arrays”, *Phys. Rev. B* **85**, 115413 (2012) (cit. on p. 40).
- [100] C. Lin, D. F. Kelley, M. Rico, and A. M. Kelley, “The “Surface Optical” Phonon in CdSe Nanocrystals”, *ACS Nano* **8**, 140326161606009 (2014) (cit. on pp. 40, 58).
- [101] N Tschirner, “Raman spectroscopy of β -carotene and CdSe-based nanocrystals”, PhD thesis (Berlin, 2012) (cit. on p. 41).
- [102] V Dzhagan, A. G. Milekhin, M. Y. Valakh, S Pedetti, M Tessier, B Dubertret, and D. R. T. Zahn, “Morphology-induced phonon spectra of CdSe/CdS nanoplatelets: core/shell vs. core-crown”, *Nanoscale* **8**, 17204–17212 (2016) (cit. on p. 41).
- [103] A. E. Raevskaya, A. L. Stroyuk, S. Y. Kuchmiy, V. M. Dzhagan, D. R. T. Zahn, and S. Schulze, “Annealing-induced structural transformation of gelatin-capped Se nanoparticles”, *Solid State Communications* **145**, 288–292 (2008) (cit. on p. 41).

- [104] E. S. Freitas Neto, N. O. Dantas, S. W. da Silva, P. C. Morais, M. A. Pereira-da Silva, A. J. D. Moreno, V López-Richard, G. E. Marques, and C Trallero-Giner, “Temperature-dependent Raman study of thermal parameters in CdS quantum dots”, *NANOTECHNOLOGY* **23**, 125701 (2012) (cit. on pp. 42, 46, 48).
- [105] K Haruna, H Maeta, K Ohashi, and T Koike, “The thermal expansion coefficient and Gruneisen parameter of InP crystal at low temperatures”, *J. Phys. C: Solid State Phys.* **20**, 5275–5279 (1987) (cit. on p. 44).
- [106] J. D. James, J. A. Spittle, S. G. R. Brown, and R. W. Evans, “REVIEW ARTICLE: A review of measurement techniques for the thermal expansion coefficient of metals and alloys at elevated temperatures”, *Measurement Science and Technology* **12**, R1–R15 (2001) (cit. on pp. 44, 50).
- [107] D. A. Padmavathi, “Potential Energy Curves & Material Properties”, *MSA* **02**, 97–104 (2011) (cit. on pp. 44, 51, 52).
- [108] J. B. Cui, K Amtmann, J Ristein, and L Ley, “Noncontact temperature measurements of diamond by Raman scattering spectroscopy”, *J. Appl. Phys.* **83**, 7929–7933 (1998) (cit. on p. 47).
- [109] V. M. Dzhagan, M. Y. Valakh, A. E. Raevskaya, A. L. Stroyuk, S. Y. Kuchmiy, and D. R. T. Zahn, “Resonant Raman scattering study of CdSe nanocrystals passivated with CdS and ZnS”, *NANOTECHNOLOGY* **18**, 285701 (2007) (cit. on p. 47).
- [110] Y. Okada and Y. Tokumaru, “Precise determination of lattice parameter and thermal expansion coefficient of silicon between 300 and 1500 K”, *J. Appl. Phys.* **56**, 314–318 (1984) (cit. on p. 50).
- [111] L Merten, “Zeitschrift für Naturforschung / A / 15 (1960)”, *Zeitung für Naturforschung* **15a**, 626–633 (1960) (cit. on p. 53).
- [112] A. J. Nozik, “Spectroscopy and hot electron relaxation dynamics in semiconductor quantum wells and quantum dots.”, *Annu. Rev. Phys. Chem.* **52**, 193–231 (2001) (cit. on p. 55).
- [113] K. Gong, D. F. Kelley, and A. M. Kelley, “Resonance Raman Spectroscopy and Electron–Phonon Coupling in Zinc Selenide Quantum Dots”, *J. Phys. Chem. C* **120**, 29533–29539 (2016) (cit. on p. 55).
- [114] A. V. Fedorov, A. V. Baranov, and K Inoue, “Exciton-phonon coupling in semiconductor quantum dots: Resonant Raman scattering”, *Phys. Rev., B Condens. Matter* **56**, 7491–7502 (1997) (cit. on p. 55).
- [115] J. J. Shiang, S. H. Risbud, and A. P. Alivisatos, “Resonance Raman studies of the ground and lowest electronic excited state in CdS nanocrystals”, *J. Chem. Phys.* **98**, 8432–8442 (1993) (cit. on p. 55).

- [116] S Schmitt-Rink, D. A. B. Miller, and D. S. Chemla, “Theory of the linear and nonlinear optical properties of semiconductor microcrystallites”, *Phys. Rev., B Condens. Matter* **35**, 8113–8125 (1987) (cit. on p. 55).
- [117] G Scamarcio, V Spagnolo, G Ventruti, M Lugara, and G. C. Righini, “Size dependence of electron-LO-phonon coupling in semiconductor nanocrystals”, *Phys. Rev., B Condens. Matter* **53**, R10489–R10492 (1996) (cit. on p. 55).
- [118] S. Nomura and T. Kobayashi, “Exciton-LO-phonon couplings in spherical semiconductor microcrystallites”, *Phys. Rev. B* **45**, 1–12 (1992) (cit. on pp. 55, 60, 61).
- [119] M. R. Salvador, M. W. Graham, and G. D. Scholes, “Exciton-phonon coupling and disorder in the excited states of CdSe colloidal quantum dots”, *J. Chem. Phys.* **125**, 184709 (2006) (cit. on p. 55).
- [120] K. Oshiro, K. Akai, and M. Matsuura, “Exciton–optical phonon interaction in a spherical quantum dot embedded in nonpolar matrix”, *Phys. Rev. B* **66**, 153308 (2002) (cit. on pp. 55, 61).
- [121] R. Zheng, M. Matsuura, and T. Taguchi, “Exciton–LO-phonon interaction in zinc-compound quantum wells”, *Phys. Rev. B* **61**, 9960 (2000) (cit. on p. 55).
- [122] A. M. Kelley, “Electron-Phonon Coupling in CdSe Nanocrystals from an Atomistic Phonon Model”, *ACS Nano* **5**, 5254–5262 (2011) (cit. on pp. 55, 58).
- [123] H. Lange, M. Artemyev, U. Woggon, T. Niermann, and C. Thomsen, “Experimental investigation of exciton-LO-phonon couplings in CdSe/ZnS core/shell nanorods”, *Phys. Rev. B* **77**, 193303 (2008) (cit. on p. 57).
- [124] P. Han and G. Bester, “Insights about the Surface of Colloidal Nanoclusters from Their Vibrational and Thermodynamic Properties”, *J. Phys. Chem. C* **116**, 10790–10795 (2012) (cit. on pp. 58, 87, 102, 104).
- [125] P. Han and G. Bester, “Heavy strain conditions in colloidal core-shell quantum dots and their consequences on the vibrational properties from ab initio calculations”, *Phys. Rev. B* **92**, 125438–125410 (2015) (cit. on pp. 58, 102, 104).
- [126] A. M. Kelley, “Electron-Phonon Coupling in CdSe Nanocrystals”, *J. Phys. Chem. Lett.* **1**, 1296–1300 (2010) (cit. on p. 61).
- [127] M Nirmal, D. J. Norris, M Kuno, M. G. Bawendi, A. L. Efros, and M Rosen, “Observation of the “Dark exciton” in CdSe quantum dots”, *Phys. Rev. Lett.* **75**, 3728–3731 (1995) (cit. on p. 64).

- [128] D. J. Norris, A. L. Efros, M. Rosen, and M. G. Bawendi, “Size dependence of exciton fine structure in CdSe quantum dots”, *Phys. Rev. B* **53**, 90951–16354 (1996) (cit. on pp. 64, 68, 75).
- [129] M. Chamarro, C. Gourdon, P. Lavallard, and A. I. Ekimov, “Enhancement of Exciton Exchange Interaction by Quantum Confinement in CdSe Nanocrystals”, *Japanese Journal of Applied Physics Supplement* **34**, 12– (1995) (cit. on p. 64).
- [130] M. Nirmal, C. B. Murray, and M. G. Bawendi, “Fluorescence-line narrowing in CdSe quantum dots: Surface localization of the photogenerated exciton”, *Phys. Rev. B* **50**, 2293–2300 (1994) (cit. on p. 64).
- [131] A. L. Efros, “Luminescence polarization of CdSe microcrystals”, *Phys. Rev., B Condens. Matter* **46**, 7448–7458 (1992) (cit. on p. 64).
- [132] A. Rodina and A. L. Efros, “Magnetic Properties of Nonmagnetic Nanostructures: Dangling Bond Magnetic Polaron in CdSe Nanocrystals”, *Nano Lett.* **15**, 4214–4222 (2015) (cit. on p. 64).
- [133] A. V. Rodina and A. L. Efros, “Radiative recombination from dark excitons in nanocrystals: Activation mechanisms and polarization properties”, *Phys. Rev. B* **93**, 155427 (2016) (cit. on pp. 64, 81).
- [134] P. C. Sercel, A. Shabaev, and A. L. Efros, “Photoluminescence Enhancement through Symmetry Breaking Induced by Defects in Nanocrystals”, *Nano Lett.* **17**, 4820–4830 (2017) (cit. on p. 64).
- [135] L. Biadala, E. V. Shornikova, A. V. Rodina, D. R. Yakovlev, B. Siebers, T. Aubert, M. Nasilowski, Z. Hens, B. Dubertret, A. L. Efros, and M. Bayer, “Magnetic polaron on dangling-bond spins in CdSe colloidal nanocrystals”, *Nature Nanotech* **47**, 4569 (2017) (cit. on pp. 64, 69, 71).
- [136] C. De Mello Donegá, “The Nanoscience Paradigm: “Size Matters!””, in *Nanoparticles* (Springer Berlin Heidelberg, Berlin, Heidelberg, Oct. 2014), pp. 1–12 (cit. on p. 70).
- [137] I. Moreels, K. Lambert, D. Smeets, D. De Muyenck, T. Nollet, J. C. Martins, F. Vanhaecke, A. Vantomme, C. Delerue, G. Allan, and Z. Hens, “Size-Dependent Optical Properties of Colloidal PbS Quantum Dots”, *ACS Nano* **3**, 3023–3030 (2009) (cit. on p. 71).
- [138] A. L. Efros and A. V. Rodina, “Band-edge absorption and luminescence of nonspherical nanometer-size crystals”, *Phys. Rev., B Condens. Matter* **47**, 10005–10007 (1993) (cit. on p. 75).
- [139] V. A. Kiselev, B. S. Razbirin, and I. N. Uraltsev, “Additional waves and Fabry-Perot interference of photoexcitons (polaritons) in thin II–VI crystals”, *physica status solidi (b)* **72**, 161–172 (1975) (cit. on p. 75).

- [140] J. M. Elward and A. Chakraborty, “Effect of Dot Size on Exciton Binding Energy and Electron–Hole Recombination Probability in CdSe Quantum Dots”, *J. Chem. Theory Comput.* **9**, 4351–4359 (2013) (cit. on p. 76).
- [141] S. V. Goupalov and E. L. Ivchenko, “Electron–hole long-range exchange interaction in semiconductor quantum dots”, *Journal of Crystal Growth* **184-185**, 393–397 (1998) (cit. on p. 76).
- [142] V. M. Huxter, V. Kovalevskij, and G. D. Scholes, “Dynamics within the Exciton Fine Structure of Colloidal CdSe Quantum Dots”, *J. Phys. Chem. B* **109**, 20060–20063 (2005) (cit. on pp. 79, 80).
- [143] V. I. Klimov, A. A. Mikhailovsky, D. W. McBranch, C. A. Leatherdale, and M. G. Bawendi, “Mechanisms for intraband energy relaxation in semiconductor quantum dots: The role of electron-hole interactions”, *Phys. Rev. B* **61**, R13349–R13352 (2000) (cit. on pp. 79, 80).
- [144] P. Guyot-Sionnest, B. Wehrenberg, and D. Yu, “Intraband relaxation in CdSe nanocrystals and the strong influence of the surface ligands”, *J. Chem. Phys.* **123**, 074709–8 (2005) (cit. on pp. 79, 80).
- [145] D. Fan, R. Zhang, Y. Zhu, and H. Peng, “Size dependence of surface optical mode and electron-phonon coupling in ZnO nanocombs”, *Physica B: Physics of Condensed Matter* **407**, 3510–3514 (2012) (cit. on p. 87).
- [146] A. S. Ethiraj, N. Hebalkar, S. K. Kulkarni, R. Pasricha, J Urban, C Dem, M Schmitt, W Kiefer, L Weinhardt, S Joshi, R Fink, C Heske, C Kumpf, and E Umbach, “Enhancement of photoluminescence in manganese-doped ZnS nanoparticles due to a silica shell”, *JOURNAL OF CHEMICAL PHYSICS* **118**, 8945–8953 (2003) (cit. on p. 87).
- [147] J. Wang, Z. H. Shah, S. Zhang, and R. Lu, “Silica-based nanocomposites via reverse microemulsions: classifications, preparations, and applications”, *Nanoscale* **6**, 4418–21 (2014) (cit. on pp. 88, 115).
- [148] K Osseo-Asare and F. J. Arriagada, “Growth Kinetics of Nanosize Silica in a Nonionic Water-in-Oil Microemulsion: A Reverse Micellar Pseudophase Reaction Model”, *J. Colloid Interface Sci* **218**, 68–76 (1999) (cit. on pp. 88, 89).
- [149] A. Hassinen, I. Moreels, K. De Nolf, P. F. Smet, J. C. Martins, and Z. Hens, “Short-Chain Alcohols Strip X-Type Ligands and Quench the Luminescence of PbSe and CdSe Quantum Dots, Acetonitrile Does Not”, *J. Am. Chem. Soc.* **134**, 20705–20712 (2012) (cit. on p. 91).

- [150] A. Biermann, T. Aubert, P. Baumeister, E. Drijvers, Z. Hens, and J. Maultzsch, “Interface formation during silica encapsulation of colloidal CdSe/CdS quantum dots observed by in situ Raman spectroscopy”, *J. Chem. Phys.* **146**, 134708–7 (2017) (cit. on pp. 96, 99, 100, 105, 110).
- [151] M. A. Boles, D. Ling, T. Hyeon, and D. V. Talapin, “The surface science of nanocrystals”, *Nature Materials* **15**, 141–153 (2016) (cit. on p. 103).
- [152] M. O. Trulson and R. A. Mathies, “Raman Cross Section Measurements in the Visible and Ultraviolet Using an Integrating Cavity: Application to Benzene, Cyclohexane, and Cacodylate”, *J. Chem. Phys.* **84**, 2068–2068 (1986) (cit. on pp. 105, 106).
- [153] T. M. Aminabhavi, V. B. Patil, M. I. Aralaguppi, and H. T. S. Phayde, “Density, viscosity, and refractive index of the binary mixtures of cyclohexane with hexane, heptane, octane, nonane, and decane at (298.15, 303.15, and 308.15) K”, *Journal of Chemical & Engineering Data* **41**, 521–525 (1996) (cit. on p. 106).
- [154] S. H. Wemple, “Refractive-Index Behavior of Amorphous Semiconductors and Glasses”, *Phys. Rev. B* **7**, 3767–3777 (1973) (cit. on p. 106).
- [155] A. Franceschetti, A. Williamson, and A. Zunger, “Addition Spectra of Quantum Dots: the Role of Dielectric Mismatch”, *J. Phys. Chem. B* **104**, 3398–3401 (2000) (cit. on pp. 106, 107).
- [156] A. Franceschetti and A. Zunger, “Pseudopotential calculations of electron and hole addition spectra of InAs, InP, and Si quantum dots”, *Phys. Rev. B (Condensed Matter and Materials Physics)* **62**, 2614–2623 (2000) (cit. on p. 106).
- [157] A. V. Rodina and A. L. Efros, “Effect of dielectric confinement on optical properties of colloidal nanostructures”, *Journal of Experimental and Theoretical Physics* **122**, 554–566 (2016) (cit. on p. 106).
- [158] L. E. Brus, “On the development of bulk optical properties in small semiconductor crystallites”, *Journal of Luminescence* **31-32**, 381–384 (1984) (cit. on p. 111).
- [159] G. M. Hale and M. R. Querry, “Optical Constants of Water in the 200-nm to 200- μ m Wavelength Region”, *Appl Opt* **12**, 555–563 (1973) (cit. on p. 111).
- [160] V. M. Dzhagan, M. Y. Valakh, O. E. Raevska, O. L. Stroyuk, S. Y. Kuchmiy, and D. R. T. Zahn, “The influence of shell parameters on phonons in core-shell nanoparticles: a resonant Raman study”, *NANOTECHNOLOGY* **20**, 365704 (2009) (cit. on p. 113).

15 Acknowledgments

Finally, I want to thank all my colleagues from the AG Thomsen, AG Hoffmann and AG Maultzsch for the exceptionally nice working atmosphere and many discussions, which were a good mix of fruitful / about physics and just plain ridiculous. Additionally, there are a few people I want to thank in particular:

- For the QD syntheses, great discussions and help regarding all questions on chemistry: the whole group of Zeger Hens (and Zeger Hens himself, of course), especially Tangi Aubert and Sofie Abé
- For their help and involvement with measurements and great teamwork, my students Narine Ghazarian and Philipp Baumeister
- For introducing me to CdSe QDs and for many discussions on their Raman spectra: Holger Lange, Norman Tschirner, Christian Thomsen and Janina Maultzsch
- For great discussions and for exciton fine structure calculations: Anna Rodina, Alexandr Golovatenko and Alexander (Sasha) Efros
- For an introduction to PLE and help addressing the PLE setup, and for useful discussions of results and analysis of the acquired data: Gordon Callsen, Nadja Jankowski, Steffen Westerkamp, and Stefan Kalinowski
- For chaotic help in chaotic labs: Christian Nenstiel, Thomas Kure, Felix Nippert and Max Bügler
- For working together, trying to teach students at least something about physics and for dealing with the stressful Kirchberg organization: Hans Tornatzky, Dirk Heinrich, and Harald Scheel
- For general organisation and help with the TU bureaucracy: Anja Sandersfeld and Sabine Morgner
- For their high spirits: Sarah Schlichting and Markus Wagner
- For many things listed above and so much else: Asmus Vierck

Now, as this project comes to an end, I would like to thank Anna Rodina and Axel Hoffmann for their kind review of this thesis and Micheal Lehmann for chairing the examination.